UNIVERSITÀ
DEGLI STUDI
FIRENZE

DOTTORATO DI RICERCA IN
SCIENZE CHIMICHE

CICLO XXIX

COORDINATORE Prof. PIERO BAGLIONI

ELEMENTAL MAPS WITH X-RAY FLUORESCENCE

(XRF)

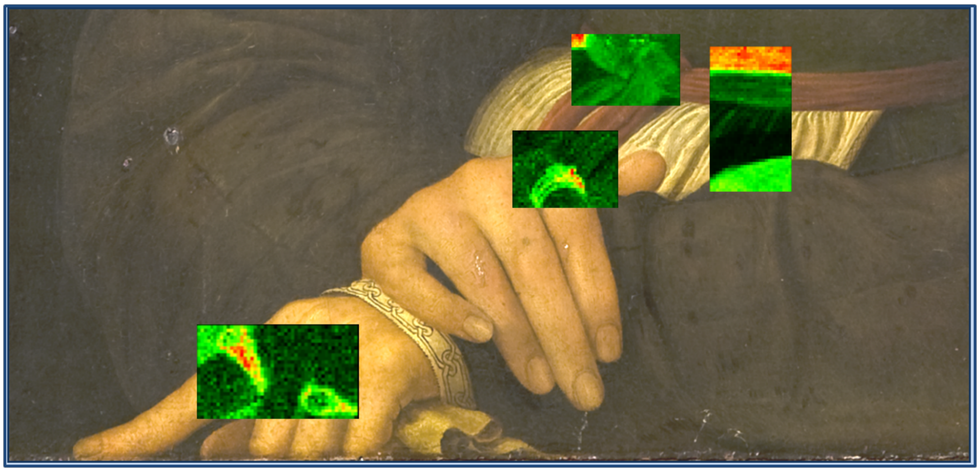

Dottorando
Dott. Chiara Ruberto

Tutore
Prof. Lorenzo Giuntini

Co-tutore
Prof. Pier Andrea Mandò

UNIVERSITÀ
DEGLI STUDI
FIRENZE

DOTTORATO DI RICERCA IN SCIENZE CHIMICHE

CICLO XXIX

COORDINATORE Prof. PIERO BAGLIONI

ELEMENTAL MAPS WITH X-RAY FLUORESCENCE (XRF)

Settore Scientifico Disciplinare CHIM/12

Dottorando
Dott. Chiara Ruberto
Chiara Ruberto

Tutore
Prof. Lorenzo Giuntini

Co-Tutore
Prof. Pier Andrea Mandò

Coordinatore
Prof. Piero Baglioni

Anni 2013/2016

SUMMARY

INTRODUCTION

The Conservation Scientist is a researcher and an expert in the field of diagnostic, conservation and restoration of Cultural Heritage (CH), who has high methodological and operational mastery of all the scientific techniques applicable in this field. Appropriate skills are required to participate in development and design of new techniques and instrumentations, as well as to plan diagnostic interventions with particular attention to the identification of methods, materials, analyses and techniques for the recovery, conservation and restoration of Cultural Heritage, in order to avoid future degradation phenomena.

Diagnostics for Cultural Heritage is a well-established research field, demanding high performance, non-destructive and portable instruments, which accounts for the growing demand for scientific techniques. Among all the techniques for CH diagnostics, X-Ray Fluorescence (XRF) is one of the most used because it allows for multi-elemental, non-invasive and non-destructive analysis (no sampling or sample preparation is required, no damage is induced to the analysed area). Furthermore, the development of portable spectrometers gives the possibility to perform *in situ* analysis. XRF technique provides information useful for the study of manufacturing techniques, dating, provenance, authenticity and conservation state.

For these reasons, since 2008 in Florence, the Labec (Laboratory of nuclear techniques for Cultural Heritage and Environmental Applications) laboratory has turned its attention to the XRF technique, developing an XRF spectrometer for punctual analyses (XRF0) with high sensitivity to low Z elements, successfully used for many applications on works of art.

Traditionally, XRF spectrometers have been used for single point measurements, where a small area, the dimensions of which are those of the X-ray beam spot on sample, is irradiated and the corresponding spectrum is acquired. Therefore, it can be questioned whether the point investigated is significant or not for the chemical compositionof the sample. Indeed, most of the objects of artistic or historical interest have quite inhomogeneous structures, even within apparently uniform areas: ‘‘anomalous’’ details may be present, on a scale of hundred microns or smaller. Such non-homogeneous structures can become a problem for compositional analyses, since these features may be difficult to identify by visual examination. Therefore, traditional “single spot” XRF analysis can result in misleading information about the composition of the material under study.

In order to overcome the outlined risk of misleading or ambiguous information, many efforts have been dedicated by the scientific community to develop XRF imaging techniques, using scanning mode acquisition systems. They allow for acquiring information both on material composition of the sample and on the distribution of the characteristic elements within the scanned area, thus permitting to obtain elemental distribution maps. Reconstructing elemental maps over a whole surface of relatively large area would undoubtedly lead to achieving results by far more significant and reliable than those obtained from multiple single-spot analysis.

The great potential of the XRF imaging, especially in the field of Cultural Heritage, has strongly stimulated the development of the first generation LABEC scanning-mode XRF1 spectrometer, between 2012 and 2013, prior to my PhD training. The XRF1, thanks to a software developed entirely in the laboratory, has allowed for elemental mapping analysis, maintaining the many attractive features of the XRF0.

A preliminary, important step of my PhD thesis was to test the XRF1, in order to gain a deepened knowledge of the XRF1 scanning mode acquisition, pointing out its strengths and weaknesses. This study allowed me to identify the XRF1 limitations, to understand how to overcome them and to plan, design and develop the second generation XRF2 scanner, a more performant instrument, more lightweight, easier to handle and to use than XRF1.

This second generation spectrometer was designed exploiting the experience acquired during my PhD training and considering also the performances of the XRF1, obtained by methodological test on standard laboratory samples and measurements on Cultural Heritage real cases. Several tests and measurements were carried out to verify the effectiveness and reliability of the solutions adopted for the XRF imaging of objects of complex structure. In order to accomplish this task, during the three years of my PhD training, I carried out a wide diagnostic campaign on a total of 30 artworks, among which paintings by the “Old Masters”, such as Simone Martini, Botticelli, Leonardo, Raffaello, Carracci and by modern painters, such as Manet, Previati, Lazzari, Leger, Buffet and Picasso (proposed attribution). In addition, it was also possible to test our spectrometer on a Roman mosaic, a rather unconventional application of the XRF imaging.

All the measurements on these masterworks have been possible thanks to the collaboration with many museums, conservation scientists, privates interested in CH diagnostic and with the *Opificio delle Pietre Dure* (OPD) of Florence, one of the world’s most renowned centres for artistic restoration.

In chapter 1, the physics of the X-rays fluorescence is briefly reviewed. Subsequently, the XRF spectrometry instrumentation is summarised, focusing the attention on the X-rays production, interaction with matter and detection. Then, XRF data analyses are presented, in order to explain the obtained data (spectra, maps) and to show some possible typologies of analyses.

In chapter 2, a detailed description of the first generation XRF1 scanner is reported, focusing the attention on the control/acquisition software, largely exploited also in the XRF2. In addition, some of the results obtained in CH applications, useful to better understand the use of the main functions necessary for the use of the instrument, are reported.

In chapter 3, the development of the secondgeneration XRF2 scanner is widely discussed. In this chapter, I report on the hardware and software upgrades and on the new Graphical Users Interface (GUI), which, differently from XRF1, has proved “on field” to be robust and fail-safe and “user-friendly”. The most important upgrades, concerning both hardware and software, consist in the dynamic positioning system and in the helium-flow control system. The former, maintaining constant the sample-to-scanner distance, allows for the XRF imaging of objects of complex structure, with non-planar surfaces. The latter allows for detecting low atomic number elements down to sodium, thus noticeably extending the range of detectable elements. In the final part of this chapter, other functions which make the XRF2 use easier, both for acquisition and data analyses, are presented.

In chapter 4, in order to highlight the capabilities of the XRF2 scanner, the most significant studies carried out on CH artworks are presented. Exploiting the characterization of the chemical composition, it has been possible to provide the restorers with information about original materials, manufacturing process, conservation state of the artworks and restorations or alterations occurred over the time, thus allowing them to choose the most suitable conservation/restoration treatments.

Concerning material investigations, three case studies are reported, in order to characterise the pigments and their evolution over the time, from Renaissance to the Baroque and “Modern” period.

As regards manufacturing process identification, exploiting the analyses carried out on two gilding decorations of the same historical period (around 1300), it was possible to characterise the metals employed for the gildings and identify the manufacturing processes.

A complete analysis of the conservation state of paintings represents an important guide for its restoration. In this chapter, some measurements carried out on a painting affected by the presence of calcium oxalates as decay products in varnishes, before and during the cleaning treatments, are presented. The results of this study provided restorers with information necessary to choose the correct cleaning procedures.

In the conclusions of the thesis, after some concluding remarks, perspectives for future developments of the XRF scanner at LABEC are shortly presented, for both improving the detection efficiency and the spatial resolution. Concerning the latter, I have started a collaboration with the CNA (Centro Nacional des Acelaradores, Seville, Spain), to gain a good operative knowledge on the use of XRF spectrometers equipped with polycapillary lenses.

During the evolution of my thesis, besides the time dedicated to the implementation of the XRF2 scanner and its applications, I have spent some months on another project, which ended up with the PhD work of a colleague (Catacterización No-desctructiva de Joyas Arqueológicas de Oro mediante Micro Fluorescencia de rayos X, by S. Scrivano). This work was based on the use of a μ-XRF spectrometer in order to identify the soldering technique of Etruscan gold jewels. These results will summarised in a forthcoming paper.

CHAPTER 1

The X Ray Fluorescence (XRF) spectroscopy

Although observed during several experiments, X-rays have been officially discovered by Röntgen in 1895. He produced and detected electromagnetic radiation in a wavelength range now known as X-rays, an achievement that earned him the first Nobel Prize in Physics in 1901. He was the first to systematically study this radiation and named them “X” to highlight their unknown nature. He produced the first “medical” radiographic image of the history, the so-called *Hand mit Ringen*.

This discovery opened new research fields and allowed the development of many analytical techniques based on X-rays, with a big impact on both science and society. At present, X-rays are widely employed in many application fields, from medical diagnostic to industrial quality monitoring. They allow for many non-destructive investigations, both for imaging (radiography and tomography) and compositional analysis (absorption, fluorescence, diffraction, etc.) [1].

X-rays are a part of the electromagnetic spectrum, with wavelengths shorter and energies greater than those associated to visible light photons (i.e. typically wavelengths from ~10 nm to ~ 10 pm and energies from ~100 eV to ~ 100 KeV). X-rays mainly interact with matter by photoabsorption, Compton and Rayleigh scattering and pair production. The relative intensities of these interactions essentially depend on the energy of the primary X-rays and the elemental composition of the target material, since X-ray photon energy is much higher than chemical binding energies, which can be thus neglected.

In the first part of this chapter the physics of X rays emission and interaction with matter are described. Later, the physical processes involved in the various steps of the XRF spectrometry are discussed, focusing the attention on the X-rays production, interaction and detection.

1.1. Physics of X-rays fluorescence

Although a large number of possible interaction mechanisms are known in matter, at the energies of interest for the XRF spectrometry, only three major types play an important role: photoelectric absorption, Compton and Rayleigh scattering[1]. All these processes result in sudden and abrupt changes in the photon history, in that the photon either disappears entirely or is scattered through a significant angle.

The relative importance of the three major types of interaction depends on the energy region of the radiation. For this reason, for the tube-emitted X-rays, that do not exceed 50 – 100 keV in typical XRF application, the predominant interaction are photoelectric absorption and Compton scattering.

1.1.1 Compton scattering

The Compton scattering, also known as incoherent or inelastic scattering, takes place between the incident photon and an electron in the atom of the sample material. In this scattering process, the incoming photon is deflected through an angle θ with respect to its original direction. The photon transfers a portion of its energy to a weakly bound electron (similar to a free-electron), which is then known as a *recoil electron*. Because all angles of scattering are possible, the energy transferred to the electron can vary from zero to a large fraction of incident energy. For small scattering angles, very little energy is transferred. However, a part of the original energy is always retained by the incident photon.

The cross section[2] of Compton scattering (σ_c) per atom of the absorber depends on the number of electrons available as scattering target and therefore increases linearly with Z. σ_c shows an inverse dependence on the energy of the incident photon (E), so its behaviour vs. incoming photon energy (E) and target atomic number (Z) is:

$$\sigma_c \propto \frac{Z}{E_X}$$

1.1.2 Rayleigh scattering

In addition to Compton scattering, another type of scattering can occur if the photons interact coherently with a whole absorber atom. This coherent or elastic scattering (Rayleigh scattering) process neither excites nor ionizes the atom, and the photon retains its original energy after the scattering event. In this process virtually no energy is transferred but the direction of the photon is changed. The probability of coherent scattering is significant only

---

[1] At energies below 1022 keV, no pair production is possible. For XRF spectroscopy, energies of interest are typically well below 100 keV, ranging normally from one to few tens of keV. So pair production will not be taken into account here

[2] The cross section is a measure of the probability of an event

for photon energies typically well below a few hundred keV for common materials, and is most prominent in high-Z samples. The importance of Rayleigh scattering is mainly limited to low photon energies and high Z materials, as the cross section of coherent scattering (σ_R) decreases with the square of energy (E), and increases with the square of the atomic number (Z) of the target material:

$$\sigma_R \propto \frac{Z^2}{E^2}$$

1.1.3 Photoelectric effect

In the photoelectric absorption process, a photon interacts with an atom in which the photon completely disappears. In this inelastic collision, the incident photon energy ($E_p = h\nu$) is transferred to an atomic electron (photoelectron), which is then ejected (Fig. 1.1).

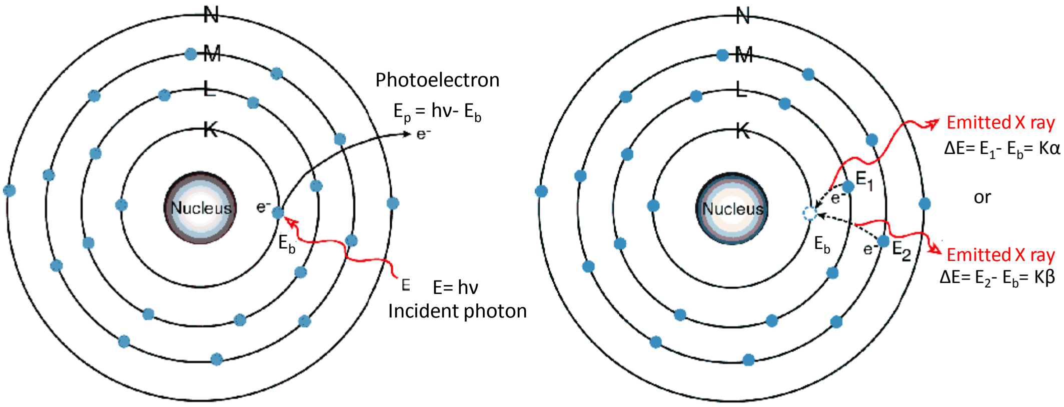

Figure 1.1. Scheme of the photoelectric absorption (left) and emission (right) processes

The photoelectron appears with an energy (E_p) given by:

$$E_p = h\nu - E_b$$

where E_b represents the binding energy of the photoelectron in its original shell.

Then, in a very short time (~10^{-15} s), an electron from an outer atomic shell will occupy the vacancy left by the photoelectron, releasing an X-ray with energy equivalent to the difference between the two electronic levels, as shown in figure 1.1.

This further vacancy will be filled through capture of a free electron from the medium and/or rearrangement of electrons from other outer shells of the atom. Therefore, one or more characteristic X-ray photons may also be generated.

The photoelectric process is the predominant mode of interaction for X-rays of relatively low energy. The process is also enhanced for absorber materials of high atomic number *Z*. No single analytic expression is valid for the cross section of photoelectric absorption (σ_{Ph}) per atom over all ranges of E and Z, but a rough approximation is:

$$\sigma_{Ph} \sim \frac{Z^n}{E^{3.5}}$$

where the exponent n varies between 4 and 5.

A plot of photoelectric absorption energy dependence is shown in figure 1.2, where, in the low-energy region, discontinuities in the curve (*absorption edge)* are clearly visible in correspondence to the photon energies equivalent to the binding energies of electrons in the various shells of the absorber atom. The edge lying highest in energy therefore corresponds to the binding energy of the *K*-shell electron. For photon energies slightly above the edge, the photon energy is just sufficient to undergo a photoelectric interaction, in which a *K*-electron is ejected from the atom. For photon energies slightly below the edge, this process is no longer energetically possible and therefore the interaction probability drops abruptly. Similar absorption edges occur at lower energies for the *L, M*, ... electron shells of the atom.

1.2. X-rays absorption into the matter

The interaction processes remove the photon from the primary beam, either by absorption or by scattering it away from the original direction, as previously discussed. The probability per unit path length (σ_{Tot}) that a photon is removed from the beam is simply the sum of the processes above mentioned and thus we have:

$$\sigma_{Tot} = \sigma_R + \sigma_C + \sigma_{Ph}$$

where σ_{Ph} is the cross section for the photoelectric effect, σ_C for the Compton effect and σ_R for the Rayleigh scattering.

In the interaction with matter, the primary beam intensity (I_0) changes following the *exponential attenuation law*:

$$I = I_0 e^{-(\mu \rho x)}$$

where I *is* the number of transmitted photons through a slab of material of density ρ and thickness x and μ is the mass attenuation coefficient, which is proportional to the total cross section of the process (σ_{Tot}):

$$\mu = k\ (\sigma_R + \sigma_C + \sigma_{Ph})$$

In the case of a heterogeneous medium, such as a compound or a mixture, the mass attenuation coefficient (μ_{Tot}) can be calculated taking into account the contribution of each element in the sample:

$$\mu_{tot} = \sum_i \mu_i \, w_i$$

where the w_i factors represent the weight fraction of element i in the compound or mixture.

As an example, in figure 1.2 the mass attenuation coefficients for a light (C) and a heavy (Pb) element are shown. The plots refer to the photon cross section in interaction with matter, as the coefficient μ is directly influenced by the cross section of each phenomenon.

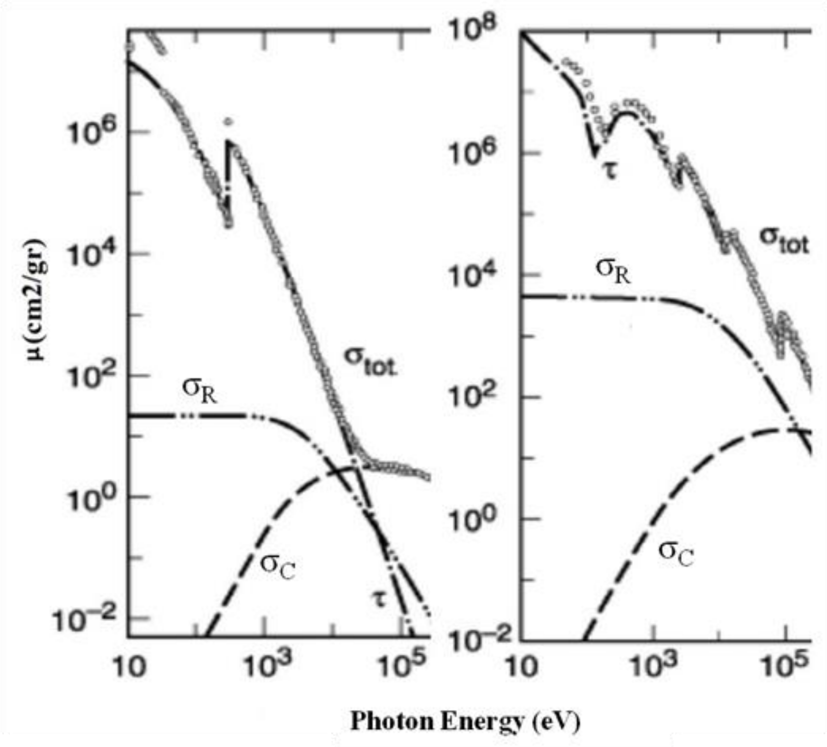

Figure 1.2. Mass attenuation coefficients (μ) for C (left) and Pb (right). In the plots are shown the contribution of: σ_C (scattering Compton), σ_R (scattering Rayleigh) and σ_{tot} ($\sigma_{Ph}+ \sigma_C + \sigma_R$)

In this figure the above-mentioned *absorption edges* are clearly visible. These edges, corresponding to the binding energy of the shells of the atom, are characteristic of each element.

1.3. Characteristic X-rays emission

As said in paragraph 1.1.3, after ionization there is a natural tendency for the electrons to rearrange themselves to return the atom to its lowest energy or ground state. The energy liberated in the transition from the excited to the ground state is emitted as an *X-ray* of energy given by the difference between the initial and the final state of the filling electron (Fig. 1.1).

Due to the fact that the atomic orbital energies are discrete and characteristics of the element, discrete emission lines are obtained. For example, if the vacancy is temporarily created in the *K* shell, a characteristic X-ray is produced when that vacancy is subsequently filled by an electron. If that electron comes from the outer *L* shell, then a photon is produced, whose energy is equal to the difference in binding energies between the *K* and *L* shells. This transition is identified as K_α *line* of the emitting atom. If the filling electron originated in the *M* shell, the photon so-produced, with slightly larger energy, is identify as K_β *line*. The *K*-series photons with maximum energy are produced when the vacancy is filled by a free or unbound electron, and the corresponding photon energy is then simply given by the *K* shell binding energy.

Vacancies created in outer shells by the filling of a *K* shell vacancy are subsequently filled with the emission of *L*-, *M*-, ... series of characteristic X-rays, as shown fig. 1.3. The same nomenclature is used also if the electron is extracted from the L, M,… shell: the fluorescence lines are named Lα, Lβ, Lγ, (Mα, Mβ, Mγ).. according to the provenance shell of the filling electron.

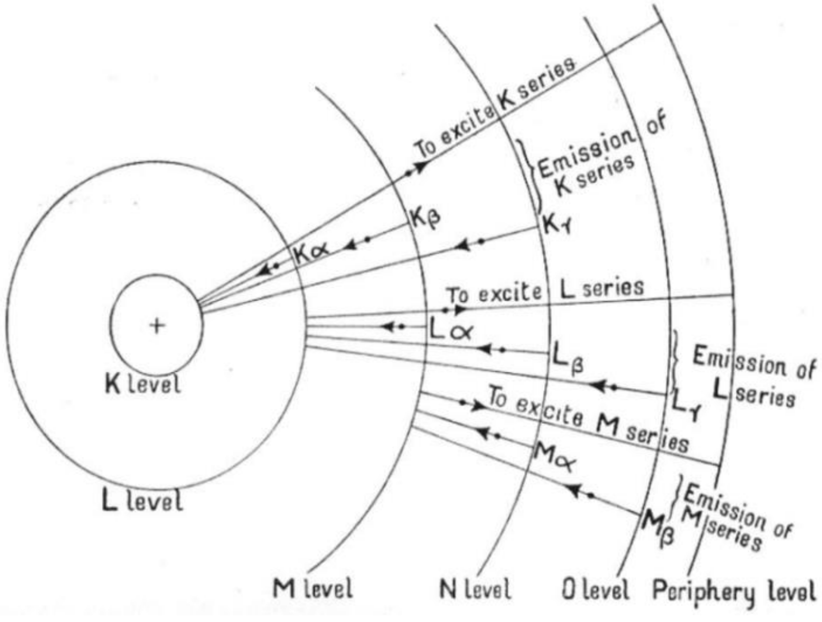

Figure 1.3. Scheme of characteristic X-ray nomenclature

Every element has its own X-Ray “fingerprint”, a unique pattern consisting of a combination of K, L, M, … lines, due to its peculiar atomic structure, which allows for unequivocal element identification.

The energy of the fluorescence lines provides information about elemental composition, while their intensities are related to the amount of the elements in the sample (the higher the number of produced X-rays, the higher the number of emitting atoms).

In some cases, the excitation energy of the atom is transferred directly to one of the outer electrons, causing it to be ejected from the atom. This process, where an electron may substitute the characteristic X-ray in carrying away the atomic excitation energy, is called Auger emission and represents a non-radiative, competing process with respect to X ray emission. The fraction of the electronic vacancies of a shell of an element *i* generating fluorescence is indicated by the fluorescence yield ω_i (Fig. 1.4). The fluorescence cross section, which is the probability that an X-ray is emitted after a photo-ionisation of the target atom, is directly proportional to the product of the fluorescence yield and to the photoelectric effect cross section.

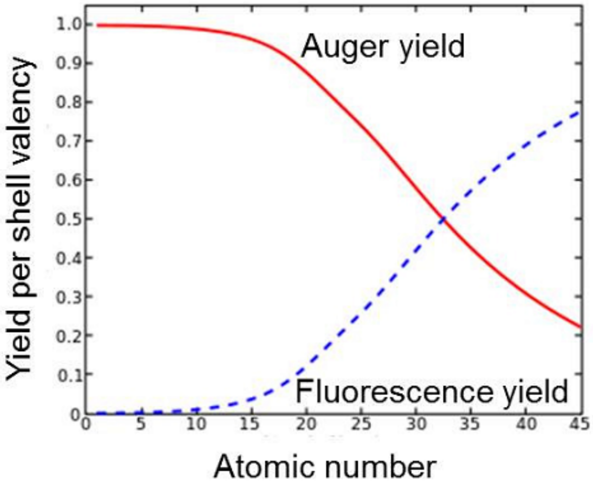

Figure 1.4. Auger and fluorescence yields: the two effects are in competition. For high Z elements a fluorescence phenomenon is more probable than Auger, while it is the opposite for low Z elements

1.4. XRF spectrometers

Several analytical techniques exploit beams of ionizing radiation, such as photons and particles, to study unknown sample by detecting the characteristic X rays emitted by the atoms when they return to their ground state.

These analytical techniques can be divided into wavelength-dispersive and energy-dispersive techniques. Among the latter, the most widespread are:

- *Particle Induced X-Ray Emission* (PIXE), when an ion beam (such as proton, α or other ions in the MeV energy range) is used;
- *Electron Probe Micro-Analysis* (EPMA), when the sample ionization is generated by electron beams with keV energies;
- *X-Ray Fluorescence* (XRF), in which the ionising radiation an X-ray beam.

The last one is the subject of this work and its principles are shortly summarised in this paragraph. In particular, we review the physical processes involved in the various part of the XRF spectrometer, i.e. the production of the primary beam in the X-ray tube, the absorption of the X-rays, both along the source-to-sample and sample-to-detector paths, and the interaction of the X-rays into the detector (Figure 1.5).

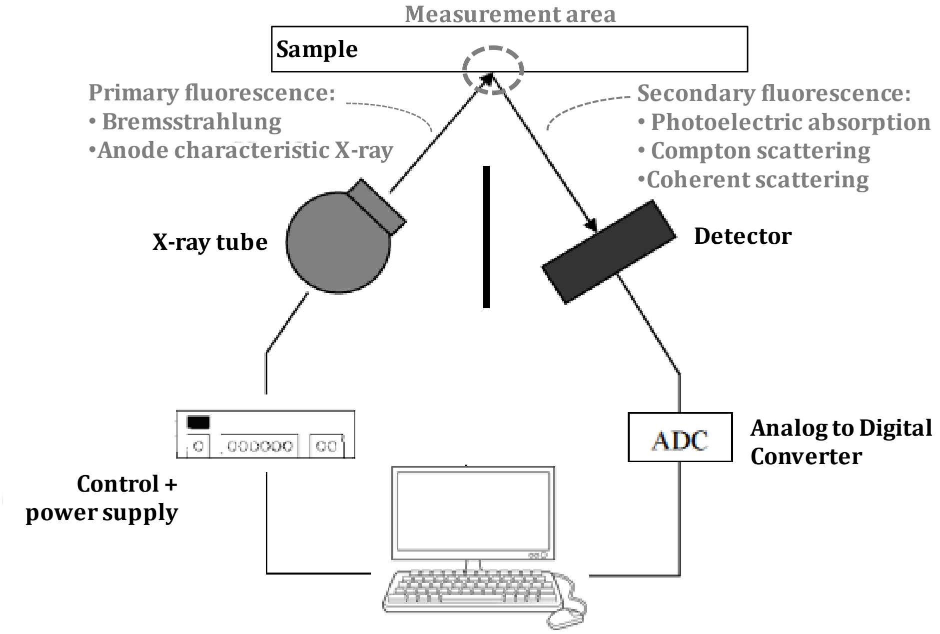

Figure 1.5. Scheme of a generic XRF spectrometer

Schematically a generic XRF spectrometer is basically composed by an X ray source, a detection system, a PC and radiosafety systems. In the next sub-paragraphs, they will be shortly described, with the related occurring phenomena.

1.4.1 Radiation sources

The most common radiation source for XRF analyses, also for this work, is the X-ray tube. The first type was the Crookes tube, dating back to the second half of the 19*th* century, later substituted by the cathode ray tube, or Coolidge tube (Fig. 1.6), mainly in side window geometry. We will focus our attention on this kind of devices.

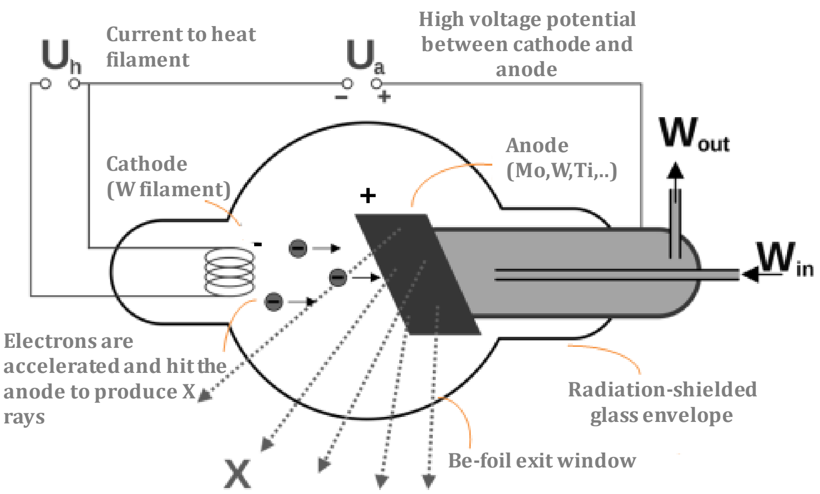

Figure 1.6. Layout of a side-window Coolidge X-ray tube. For high power applications, the X ray tube can be water cooled (in figure water inlet and outlet, Win e Wout, are reported)

This type of sources mainly consists of two electrodes in a vacuum chamber, as shown in figure 1.7. At one end it has the cathode, normally made by a tungsten filament, while at the other end it has the anode, typically a thick block of a high melting-temperature metal[3]. When the electric current flows in the filament, its temperature increases and electrons are emitted by *thermionic effect*. The electrons emitted by the cathode are accelerated towards the anode by a potential difference typically of few tens of kV. These collisions heat the anode material, so the tube must to be equipped with a cooling system, to keep anode below the melting point temperature [2], as shown in Fig. 1.6. The so-produced primary radiation exits the tube through a thin window (normally of few hundred microns of Be) and travels towards the sample in atmosphere. X-rays undergo absorption both in the window sealing the X-ray tube and in the atmosphere between the tube and the sample. These phenomena are described by the well-known *exponential attenuation* law of the X-rays, details of which are explained in paragraph 1.2.

When fast electrons interact in anode matter, a part of their energy is converted into electromagnetic radiation (*bremsstrahlung* radiation[4]) and another part, when it is sufficient to ionize the atoms in the target, into X-rays, characteristic of the anode material [3]. These two effect are responsible of the main components of the primary beam, which is emitted in all

---

[3] Anode materials are usually high melting point metals, such as Rh, Ag, or W, together with Ti, Cr, Co, Cu, Mo, Pd, or Au. The selection of the anode material depends on the intended application

[4] Bremsstrahlung radiation is the electromagnetic radiation due to the deceleration of electrons in the interaction with the anode material. It shows a continuous spectrum extending from 0 to the maximum electron energy, which depends on the applied voltage

directions. For this reason, the whole X-ray tube has to be shielded so that the beam exits only from the window (see later).

The fraction of the electron energy converted into *bremsstrahlung* increases with increasing electron energy and is larger for absorbing materials of high atomic number (proportional to the square of atomic number).

In figure 1.7, some X-ray spectra, acquired at increasing accelerating voltages (from 5 kV up to 38 kV), are report. From the figure the two components of the spectrum are apparent, i.e. the continuum bremsstrahlung spectrum, ranging from the minimum energy up to the maximum energy, and the characteristic X-ray lines of the anode material, in our case the Mo Kα=17.479 keV, Mo Kβ=19.607 keV and Mo Lα line at 2.29 keV. From the picture, it is also evident that the Mo K lines can appear only at energies higher than the Mo binding energy. Actually in figure 1.7, only the spectra acquired at voltages higher than 20 keV show the Mo K lines [4].

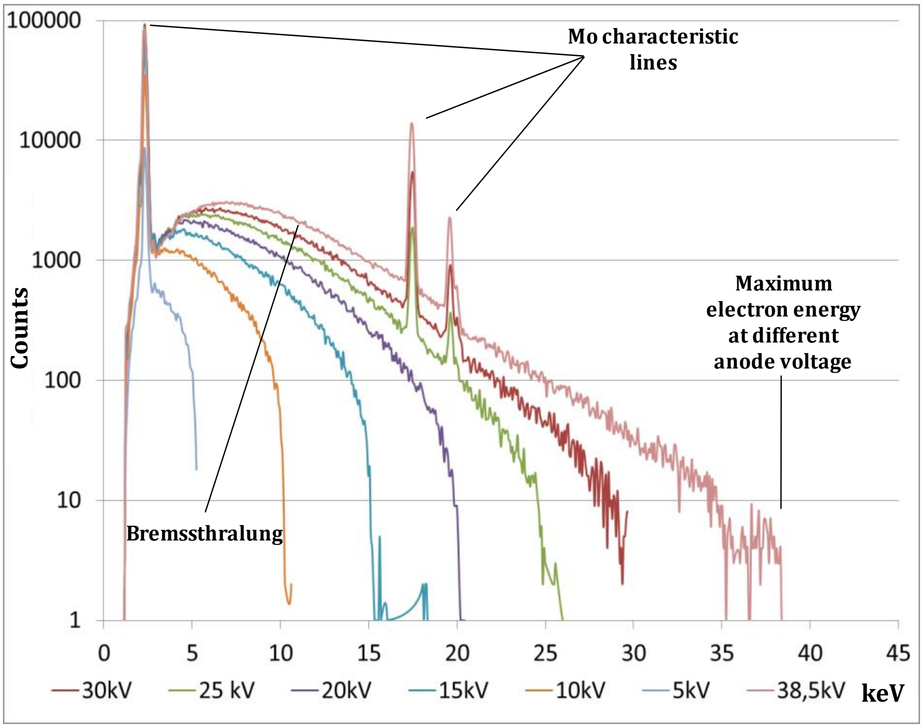

Figure 1. 7. Spectra of the primary beam obtained with a molybdenum anode, in vacuum, changing the anode voltage. The spectra are normalized for the anode current (40 μA) and the measuring time (120s). In figure is clearly visible the *bremsstrahlung* cut-off variation as a function of the maximum electron energy at different anode voltage

There are many commercially available tubes, of different sizes and parameters (voltage and current). Some types are very powerful and heavy and can be efficiently employed in laboratory set-ups. However, there is also a good choice of small and light ones, suitable for *in situ* analysis. In general, tubes for portable XRF devices have maximum voltages ranging between 30 and 60 kV and maximum currents between 0.5 and 1.5 mA. It has to be noticed that X-ray tubes are not permanent radiation sources, which means that they emit radiation only when turned on. Radiosafety rules for the use of non-permanent radiation sources are by far less stringent, which makes possible the use of XRF spectrometers also out of the laboratories, such as, for example, in museums or churches (see later).

Another kind of compact X-ray source is represented by radioactive sources, which unlike conventional tubes produce monochromatic beams. The radioisotope is chosen in order to avoid overlapping between its emission lines and the fluorescence signal we want to detect and with a half-life not too short. However, their radioactivity is always “active”, and this strongly restricts their use in public places. In addition, they typically produce low intensity beams and thus require quite long measurement times. These features make them not so suitable for CH application, above all for strict radioprotection restrictions.

The last kind of X-ray source widely used is represented by synchrotron radiation light facilities, usually equipped with many X-ray beam lines. These huge structures allow for obtaining very brilliant and monochromatic beams, which can be handled with complex and advanced optics to produced intense, high focused or semi-parallel beams. Unfortunately, they are incompatible with the request for *in situ* analysis, and even when the object transportation is possible the application procedure for beam time is quite long and complicated and intrinsically more expensive.

1.4.2 Detectors

The primary radiation impinges on the sample and induces the emission of *secondary radiation*, as explained in paragraph 1.1, mainly due to the photoelectric absorption, Compton scattering and Rayleigh scattering of the primary radiation in the sample. The X-rays emitted from the sample (secondary fluorescence) cross the path between the sample and the sensor(s) and are detected, most typically by Semiconductor Drift Detectors (SDD).

Solid state detectors consist of a semiconductor crystal (typically Ge or Si), in which the active area is composed by a *p* layer facing the X-rays, a middle part and a *n* layer that transfers the signal to a preamplifier. As said, photon absorption in the crystal originates photoelectron(s) [3]. If a voltage is applied, the motion of the so-produced electron results in an electric impulse with an amplitude proportional to the photon energy. This electric signal is then converted into a digital signal by the multichannel analyzer (MCA analyzer), which provides the energy spectrum.

To protect the semiconductor crystal, which is kept in vacuum or in a low-pressure low-Z inert gas atmosphere, usually the detector is equipped with a thin beryllium window, which necessarily absorbs the lower energy fraction of the spectrum (the typical 8 μm Be window transmits 50% of Na X-rays (1,04 keV), 8 % of F X-rays (680 eV), 3 ‰ of O X-rays (525 eV) and 10^{-6} of N X-rays (390 eV)). For particular applications, requiring a high sensitivity for light elements, devices with polymeric windows or with the naked crystal can be used.

Also in the sample-to-detector path, the secondary radiation undergo absorption, depending on the experimental configuration (air/He, thicker /thinner detector entrance window, detector crystal in gas or vacuum,…).

1.4.3. Radiosafety

Among the ionizing radiations, X-rays are characterized by an energy sufficient to induce alteration and damages to biological cells, therefore working with this type of source requires particular attentions. So adequate radio monitoring and radio safety systems are required. All the protective systems involve the instrumental workspace, above all for *in situ* measurement in public place (e.g. museums), where also the population has to be protected. For this reason, the law establishes limits for the exposition and the effective dose both for unexposed workers/public (1 mSv/year) and exposed workers (20 mSv/year).

The ICRP (International Commission on Radiological Protection) has based the radiological protection system on three fundamental principles: motivation of the practice, protection optimization, and limitation of the individual dose. In particular the general principle that we can follow is expressed in the ALARA radio safety concept: “As Low As Reasonably Achievable”. This principle considers the exposition time, the less the better, the distance from the radiogenic source, the more the better, and the shielding according to the type of radiation. The radio-safety discipline dedicated to the safeguard of workers and population is also clearly regulated by the italian D. Lgs. 230/95.

For radio-monitoring the operators are provided with personal dosimeters to determine the wearer’s radiation dose. In addition, all the equipment and instruments required for the XRF analyses must be properly shielded. The physical shielding must have suitable composition and thickness according to the type of radiation that must be shield. In particular, portable instruments for *in situ* analysis are open devices and therefore, although the X-ray source is shielded, the scattered and fluorescence radiation can in principle spread around the instrument. For this reason, in order to minimize the exposition to the radiation, and thus prevent any risk of damage to persons around, all stages of the analyses are managed by automated systems working in a controlled area (safe distance in the order of 1-3 m of diameter), where the access is forbidden to everybody during the acquisition.

1.5. X-ray fluorescence (XRF) analysis

1.5.1 XRF spectra

The secondary fluorescence spectrum obtained from the sample, excited using an X-ray tube, shows:

- the primary beam (Fig. 1.7) elastically scattered from the target material, characterised by the lines characteristic of the anode material, if the voltage applied to the source is high enough to excite them, superimposed on the *Bremsstrahlung* continuum;

- the *inelastic scattered peaks* (Compton scattering);

- the characteristic lines of the analysed sample.

In addition, some spectrum artefacts can be found, due to the interaction of the X-rays originated in the sample and the detector:

- Escape peaks

When the X-rays of the sample interact in the detector crystal (e.g. Si), they can induce a successive emission of a Si characteristic X-ray (E_{Si}=1.74 keV). If this phenomenon takes place close to the surface of the crystal, this photon can escape from the detector and only the photoelectron residual energy (E_e) given by the following equation is registered:

$$E_e = E_0 - E_{Si}$$

where E_0 is the energy of the ‘incident’ photon. This effect produces peaks, called *escape peaks,* at energy E_e lower than E_0, i.e. that of photons who underwent to full photoelectric absorption.

- Sum peaks

Another effect that can occur is the *sum peak*, indeed if two photons (E_{x1} *and* E_{x2}) arrive on the crystal with a very short time difference from one another, they can be seen as a single photon, resulting in single peak with energy:

$$E_s = E_{x1} + E_{x2}$$

1.5.2 XRF analyses

X-ray fluorescence spectrometry is a technique suitable for a wide range of applications in many disciplinary fields (environmental science, industry, geology, etc.), as it essentially provides a fast, sensitive, multi-elemental analysis. The XRF technique is widely exploited for CH applications, as no sample pre-treatment is required and it allows for non-invasive /non-destructive measurements, thus maintaining the integrity of the sample and making also

possible repeated measurements. In addition, the portable versions can be used *in situ* also on wide dimension and complex geometry objects.
XRF data analyses are fast and provide information on a wide range of inorganic materials, as actually this technique is blind to low elements ($Z<Z_{Na}=11$), as said in detector section (p.11), and no information on organic compound is achievable. Actually, some table-top instruments equipped with in vacuum sample chambers provide high energy and spatial resolution, allowing the detection also of very light element, but the samples have to be brought in the laboratory and often sampling is required. However these type of measurement are of interest for a very limited number of applications and not in CH field.

Generally, XRF qualitative or quantitative analysis can be carried out, depending on the application and the sample composition. The former allows identifying the elements present in the sample, but does not provide information regarding the quantity of each element, unless data are further processed [5]. The latter allows us to measure the absolute quantities of the elements present in the sample, taking into account the basic principle for which the detected line intensity is a function of both the element concentration (production of X-rays) and matrix composition (absorption processes). Then, taken into account all the involved processes, each fluorescence peak can be related to the element amount in the matrix[5] [6; 7; 8].

For accurate quantitative analyses, the following conditions must be met:
- homogeneous sample (no layers, no rust, no inclusions, ...);
- *infinite thickness*, i.e. the sample must be thick enough to absorb all primary X-rays.

In some instances, conditions for reliable *quantitative* analyses are not met but *qualitative* data interpretation is not satisfactory. Therefore, *semi-quantitative* analyses can be used, which allows the user to compare spectral data in order to obtain information regarding the relative concentrations of elements from different, although similar, samples. For example, this method would provide information such as “sample *A* contains approximately 20% more Ag than sample *B*” [6; 9].

Usually, XRF analysis can be carried out in point or in scanning mode, depending on the application. In traditional “single-spot’’ XRF analyses, the beam probes a region of the sample with dimensions equal to those of the beam itself. In non-homogeneous samples this analysis can result in misleading information, as the point investigated can be questioned

---

[5] As the peak intensity is influenced also by many other parameters, over the time some methodologies have been developed, in order to achieve valid and accurate data interpretation. Among these methodologies, one of the most used is the Fundamental Parameters (FP) method. An alternative and more empirical way to obtain quantitative information is preferred, such as the use of an experimental calibration curve. This curve is defined by measuring reference elemental standards with known concentrations of elements, in order to relates the specific known concentrations to peak heights

whether being significant or not for a comprehensive knowledge of the chemical composition of the object. Therefore, the main limitation of point mode analyses is the lack of information about the spatial distribution of the different elements in the sample.

To overcome this limitation, scanning mode acquisition was developed. Indeed, XRF elemental imaging allows for obtaining information both on material composition and spatial distribution of the elements in the scanned area. In this way, for each point of the scanned area, the relative fluorescence spectrum is acquired, which allows for the elemental distribution maps reconstruction, as described later (Chapter 2).

Exploiting this powerful techniques, almost all kinds of inorganic materials can be investigated, for example pigments (in paintings, mural paintings and ancient manuscripts), metals, glasses, and pottery, just to name some materials for interesting Cultural Heritage.

Material characterization can provide useful information to restorers and art-historians, helping for example to understand the manufacturing technique (for more details see Chapter 4). In archaeometric studies, it is important to determine the amounts of the trace elements, especially for mineralogical samples, because they can indicate the provenance ores and this information can be used to trace back the ancient trade-routes.

By characterizing material compositions, it is also possible to confirm the dating and the author attribution of an artefact, as e.g. when we are aware that some elements have a precise time collocation (e.g. they were used only after a certain date or only before). In this way, it is also possible to recognise forgeries and possible restorations and identify degradation products, a preliminary step necessary for proper conservation treatments (see Chapter 4).

CHAPTER 2

First generation XRF scanner of the LABEC laboratory

Cultural Heritage (CH) diagnostics are now well established and provide the foundation for conservation and restoration studies, which require initial knowledge of the materials composing the artworks and information regarding the conservation state.

The Labec (Laboratory of nuclear techniques applied to environment and cultural heritage) of INFN (National Institute of Nuclear Physics) in Florence has a long-standing experience in Ion Beam Analysis (IBA), in particular PIXE[1] [10,11,12], and radiocarbon dating [13,14,15].
Over the time, instrument transportability for CH diagnostic has become more and more important, as often artworks cannot be moved from their site, either because of the size or due to problems with permission issues, or simply because moving them to a laboratory is physically impossible, as e.g. in the case of mural paintings. For this reason the LABEC laboratory has turned its attention to the XRF technique, which allows for *in situ* analyses, contrary to what happens with the IBA techniques, which require to carry the artworks to an accelerator facility. So in 2008 the first generation XRF0 spectrometer for point analyses, with high sensitivity to low Z elements, was developed [16] and it has been successfully used for many applications on works of art (see [17, 18, 19] just to indicate a few among many).

Traditionally, XRF spectrometers have been used for single point measurements, where a small area, the dimensions of which are those of the X-ray beam spot on sample, is irradiated and the corresponding spectrum is acquired.
Unfortunately, most of the objects of artistic or historical interest have quite inhomogeneous structures, even within apparently uniform areas: ‘‘anomalous’’ details may be present even down to hundred-micron scale or smaller [20]. For this reason, traditional “single-spot’’ XRF analyses can result in misleading information, as the point investigated can be questioned

---

[1] Both with XRF and PIXE, X-ray emission is induced from the atoms of a target through the ionization of their inner shells and the subsequent electron transitions from outer shells. With PIXE, the inner shell ionization is produced by bombarding the target with a beam of ions in the MeV range, while with the XRF technique the primary beam is composed by X-rays in the tens of keV range. Both techniques provide multi-elemental analysis, in a non-invasive and non-destructive way. However, it is worth noticing that quantitative PIXE analyses are by far more straightforward and reliable than XRF one, thanks to the different interaction processes of protons and X-rays in matter

whether being significant or not for a comprehensive knowledge of the chemical composition of the object. For example, if in any of the case studies reported in Chapter 4 the analyses had been limited to few points just on the restored areas (sometimes chemically different and not distinguishable by visual inspection), the original pigment identification would have been incorrect.

So many efforts have been dedicated by the scientific community to developing techniques capable of mapping the elemental distribution of artworks, in order to overcome the outlined risk of misleading or ambiguous information. Reconstructing elemental maps over a whole surface of relatively large area would undoubtedly lead to achieving much more significant and reliable results than those obtained from multiple single-spot analysis.

In agreement with the scientific community, also at the LABEC laboratory a first generation scanning-mode XRF spectrometer was developed (XRF1), prior to my PhD training.

The portable XRF1 scanner allows for acquiring information over a whole area: at the same time both the spectra and the corresponding spatial coordinates are recorded, thus permitting to obtain elemental distribution maps, by far more significant and reliable than single-spot analyses.

At the beginning of my PhD training, some tests were carried out in order to better understand the acquisition in scanning mode. In this way, it was possible for me to gain a deepened knowledge of the XRF1 scanning system, pointing out its strengths and weaknesses. These preliminary results allowed me to understand how to overcome the evidenced limitations, and, then, how to develop the second generation XRF2 scanner. The work connected to XRF2 represents the core of my PhD work and is presented in Chapter 3.

In this chapter, a detailed description of XRF1 is reported, with the main functions necessary for the use of the instrument. In addition, some results from the experiences on CH field, gained at the beginning of my PhD training, are reported.

2.1. XRF1 hardware

The XRF1 scanner (Fig. 2.1) basically consists of a measuring head mounted on three motorized linear stages: the X and Y axis (green and red arrows respectively, shown in Fig. 2.1) allow for scanning, the Z axis (yellow arrow in Fig. 2.1) for manually setting the distance between the probe and the sample. The XRF1 controlling software has been completely designed in our laboratory.

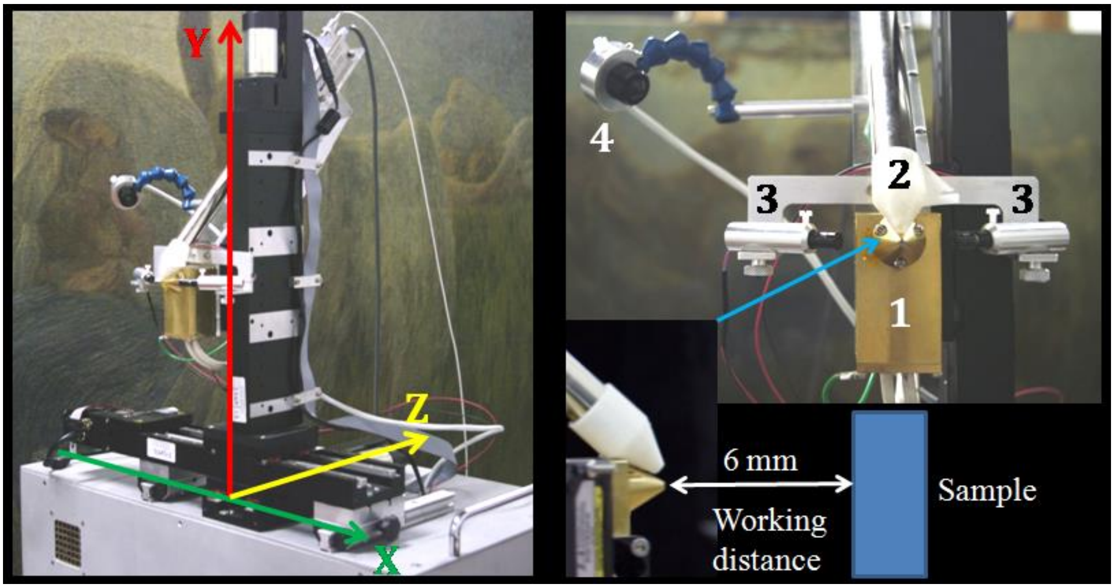

Figure 2.1. The first generation LABEC XRF scanner: on the left, the 3-axis motion system; on the right, detail of the measuring head (upper part) and the working distance (~6 mm, not in scale, in the lower part), measured from the outer surface of the collimator to the sample surface

The measuring head (Figure 2.1) of the instrument consists of:

1. A lightweight and small *Moxtek MAGNUM®* Coolidge **X-ray tube**, with a 127 μm Be exit window, 40 kV of maximum voltage and 0.1 mA maximum anode current [21]. Depending on the applications, it is possible to use either chromium or molybdenum anodes, in order to maximize the measurement sensitivity. To define the beam spot dimension, the beam is collimated with a 0.8 mm collimator [22]). The tube is shielded by a 4 mm-thick brass case, so that only the forward-emitted X-rays passing through the collimator can emerge out of the tube (this shielding fulfills the radio-safety issues for both workers and public, see par. 1.4.3, and allows us to work also out of the laboratory, for example in a church or in a museum).

2. An *XR100 SDD* (25 mm^2 × 500 mm of active area) **detector** by *Amptek*. The 8 μm thick beryllium entrance window is at about 20 mm from the beam impact point on sample [23]. For this first version, we used the detector power supply and the Peltier cooling system provided directly by the *Amptek PX5* module.

3. **Two laser pointers**, each one at 45◦ to the direction of the X-ray beam (Fig. 2.1), which allow both setting the correct sample-to-scanner distance (~6 mm from the outer surface of the collimator to the sample surface – scheme in the lower right part of Fig. 2.1) and choosing the desired irradiation zone. This is possible because, at the correct working sample-to-head distance (minimum beam waist size and maximum X-ray detection efficiency), the two laser spots on the sample surface merge into a single spot: in these conditions we know that the head is at the correct working distance (0.1 mm uncertainty), indicating the X-ray beam impact point on sample and, thus, the irradiation area.

The set-up and geometry of the measuring head of the XRF2 remain unchanged from this just explained, therefore also the working distance, extensively discussed in chapter 3.2, is measured in the same way and it corresponds to ~6 mm.

4. An *AXIS CCD P1214 Ethernet* ***HDTV*** **camera** [24]. This very compact camera (2 cm outer diameter and 4 cm total length) is cable connected (8 m maximum distance) to the control unit, which provides power and network connections. The camera allow for remotely controlling the positioning of the instrument and viewing the irradiation area also while the persons using the XRF1 are afar (as it is necessary to comply with radio-safety regulations).

X-ray tube and detector, lying on the same vertical plane, are both placed at 45°with respect to each other, with the former placed so that the beam is perpendicular to the target, kept in vertical position.

Measuring head motion is actuated by three fast and lightweight DC-current, high-precision *M414.8PD* linear stages by *Physik Instrumente* [25]. Each linear stage (X, Y and Z) is controlled by a Mercury TM/C-862DC controller, USB connected to the control computer.
The linear stages are placed on top of an aluminum box containing all the power supplies (motors, detectors, lasers, camera, etc.). The box contains also the 14 bit-digitizer (*DT5724* by *CAEN),* which converts and digitizes the pre-amplified signals from the SDD detector. The *DT5724* communicates with the acquisition computer via a fast optical connection, which allows for high acquisition rates, as in our case, where large amounts of data are acquired in short times (just to give the order of magnitude, we can acquire up to 100 MB of data in less than an hour, which corresponds to tens of kHz acquisition rates).
During the measurement, data are stored in a dedicated memory location of the control computer.

The hardware of the scanner was designed in order to minimize the total dimensions and weight of the instrument and actually the overall system (linear stages and measuring head) is installed on top of an aluminum box, with dimensions of 70 x 50 x 35 cm^3 and weight of 20 kg. Considering transportation, the main parts that must be carried are: the measurement station, computer and the radioprotection system. They can all be transported in three boxes using a car, instead of a track, as it was necessary with the previous generation, point-mode XRF0 spectrometer.

Radio-safety is actuated through 4 independent, light and easy-to-move posts, equipped with reflectors and Sick/Wl4 photocells, which are normally positioned to form a square of approximately 4 m^2 to delimit a no-access area[2] (Fig. 2.2).

---

[2] Tanks to the brass tube shielding, at the minimum allowed distance between the instrument and the operator (2 m, thanks to the fence posts, as described above), at the highest possible-ray intensity, the equivalent dose is less than 10 μSv/y and therefore not significant, as the maximum dose permitted for the population is less than 1 mSv/y

Figure 2.2. Image of the interlock system used to define the security area around the instrument

If a person crosses the line defined by a pair of posts, the interlock system turns off the X-ray tube and the system can only be switched on after clearance of the area. A red light switches on when X-rays are emitted; an emergency button is also present on the XRF1 to manually turn off the tube when pressed.

All the software used for motion, acquisition, elaboration and radio-safety has been developed by using the QT cross-platform application framework widely used for developing software and Graphical User Interface (GUI) [26]. The choice for this open-source platform allows us to easily adapt our instrument to future hardware developments and different experimental conditions. This could be impossible by using proprietary systems.

Thanks to these features, which make the system light, compact and safe, both for workers and public, the first generation LABEC XRF scanner is a truly portable instrument, suitable for *in situ* analysis, especially for CH applications.

2.2. Control and acquisition software

To map the area to investigate, an in-house software was developed by using the Qt Platform. For each pixel of the map, both the X-Y coordinates and the X-ray spectrum, acquired while the stage travels inside that pixel, are recorded. In this way the information collected from the whole area is rearranged in such way as to obtain the distribution maps of the elements. The maximum size of a single map is 20 x 20 cm^2, limited only by the range of the motorized stages.

The software is organised in three macro-functions, *Initialization*, *Point motion* and *Continuous motion,* every one with a dedicated window in the GUI (Graphic User Interface). All the functions are essential for the use of the XRF spectrometer and for this reason have been maintained in all the versions of the control software.

2.2.1 Function 1: *“serial” and “init” panels*

In order to allow the communication between the control computer and the stages, every motor has to be assigned to a different USB port. This is accomplished by using two spin boxes, as shown in Fig. 2.3 a (here, the X and Y motors have not yet been assigned to the respective USB ports and actually the buttons for the port assignment (“*Assign port X*” and “*Assign port Y*”) are still active). After the communication is established, the program identifies all the connected stages and sets up the motion parameters (minimum and maximum velocity, maximum displacement from the initial position, which in principle can be different for every stage).

After motor connection and identification, the “*INI X*” and “*INI Y*” buttons can be pushed, thus calling the initialization macro function, in order to move the stages to the reference position[3] and thus allowing for the absolute positioning of each stage, readable in the *“Posizione X*” and *“Posizione Y”* boxes in the lower part of the window, shown in Fig. 2.3 b. During the initialisation of each axis, the system is fully busy and the user has to wait until the initialization is complete before doing any other operation.

Motors are initialised sequentially. Should any problem in motor initialisation arise, the software will display all the warnings sent by the motor controllers, which allows for an easy and fast identification of the problem(s).

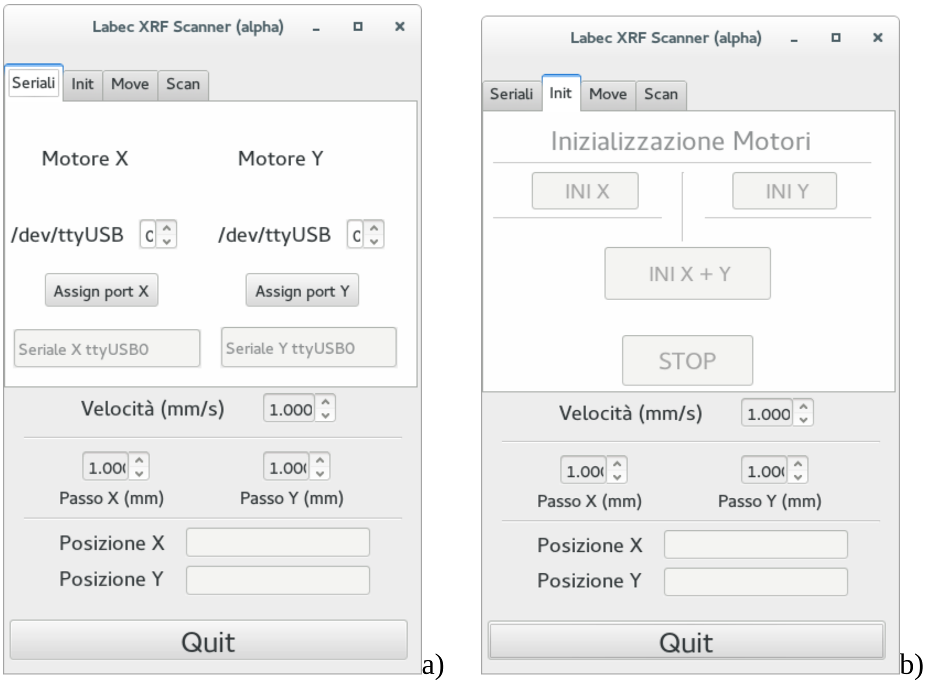

/dev/ttyUSB 0

/dev/ttyUSB 0

Seriale X ttyUSB0

Seriale Y ttyUSB0

Velocità (mm/s) 1.000

Passo X (mm) 1.000

Passo Y (mm) 1.000

Posizione X

Posizione Y

Figure 2.3. View of the GUI interface: (a) the page assign the USB ports to the stages, (b) the stages initialization page

---

[3] The reference sensors are used to reference the absolute position of the stage and are located approximately in the middle of each travel range

2.2.2 Function 2: Move panel

Muovi X a: 100.00
Muovi Y a: 100.00
Velocità (mm/s) 1.000
Passo X (mm) 1.00
Passo Y (mm) 1.00

Figure 2.4. View of the GUI interface for the point motion of the stages

By using the panel *Move*, shown in figure 2.4, it is possible to move every motor, and so also the measurement head, to any user-defined position, simply by selecting the final position in the two spin boxes *"Muovi X a:"* and "*Muovi Y a:"*. In each spin box the position can be selected in any value ranging from 0 mm to 200 mm, the latter corresponding to the full motor travel range (200 mm). Alternatively, it is possible to change the position of the stage of a discrete quantity, defined in the lower spin boxes (*"Passo X (mm)"*and *"Passo y (mm)"*)[4]. This is accomplished by simply pushing one of the four buttons (*Up*-, *Down*-, *Left*- or *Right-)* present on the left of the interface window. In both cases, the velocity defined in the spin box *"Velocità (mm/s)"*, is the same for both horizontal and vertical movements and can be chosen in the (5 µm/s – 50 mm/s) range.

This panel also provides info about the actual position, shown in the boxes "*Posizione X*" and *"Posizione Y*", which is called for every motor, as it can be required to simultaneously move all the axes.

The emergency S*top* button is defined as a general tool, in order to be able to stop the motion on all the axis with a single operation.

Usually, prior to an acquisition in scanning mode, this macro function is used to select a suitable area according to the type of analysis and/or sample geometry. Basically, exploiting the laser spot on the sample, it is possible to visualize the perimeter of the area to be scanned, within which the area of interest has to be included. In this way the vertices, required to work in scanning mode, can be identified.

---

[4] This step is however bigger than the minimum incremental motion (0,25 µm)

2.2.3 Function 3: Scan

Function 3 was designed to allow for a continuous stage movement, instead of a step-motion, as it is most common in commercial systems. A continuously-moving scanner represents a remarkable improvement with respect to step-motion instruments, although both can allow for elemental imaging, because in the latter data are acquired only when the stage is at rest, while with our method the instrument is always in acquisition, thus reducing the dead time connected to the movement from one position to the next one, noticeably increasing data acquisition efficiency.

Elemental distribution maps are acquired by performing a boustrophedon movement, where the continuous motion can be chosen horizontal, as in the *SCAN X-Y* mode (Fig. 2.5 a), or vertical, in the *SCAN Y-X* mode (Fig. 2.5 b).

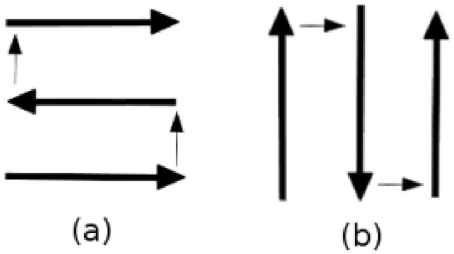

Figure 2.5. Scheme of the two ways that the scanning procedure can be set: a) *X-Y scan*, b) *Y-X scan*

For the elemental mapping, several parameters have to be defined by the users, as shown in figure 2.6 a.

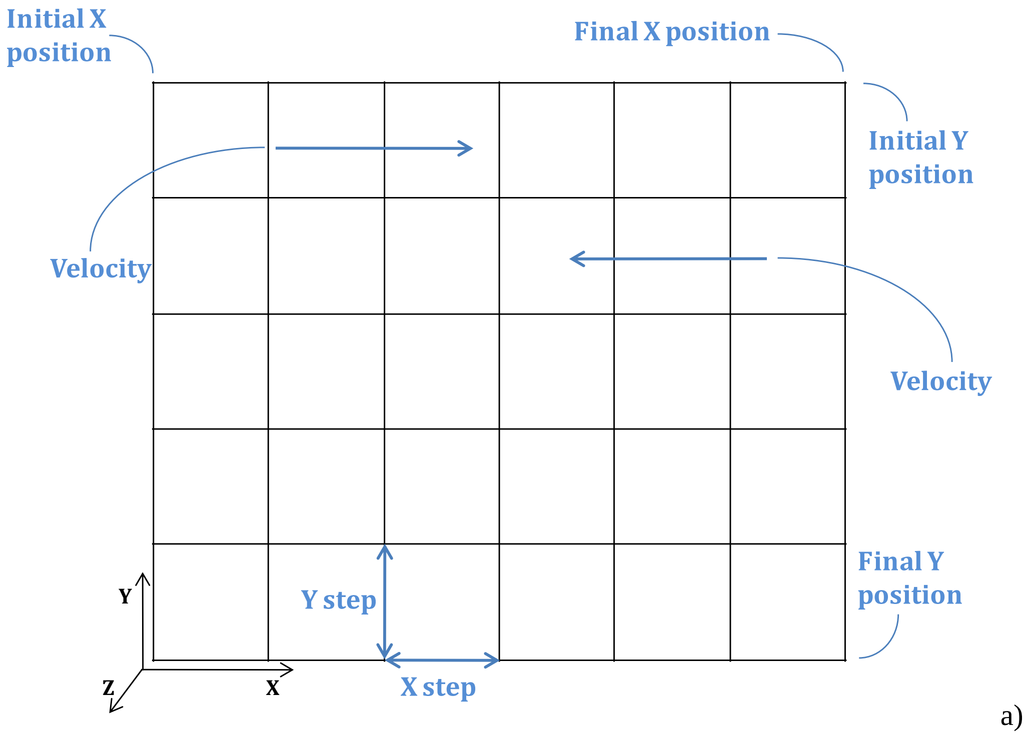

Xmin (mm) 0.000
Ymin (mm) 0.000
Xmax (mm) 200.000
Ymax (mm) 200.00
Velocità (mm/s) 1.000
Passo X (mm) 1.00
Passo Y (mm) 1.00

b)

Figure 2.6 a) Parameters required for the scanning mode acquisition; b) view of the relative GUI interface

The map parameters (initial and final x position, initial and final y position, velocity[5], x and y step[6]) are passed to the control program by seven different spin boxes, as shown in figure 2.6 b.

The “continuous motion” function is performed by nested loops and for every loop a singular motion is executed, as shown in figure 2.7. As an example, let’s consider now the loop dedicated to the motion along the x direction for the acquisition of the nth-row of the map. When the *end loop condition* is satisfied, i.e. at the arrival at the final x position, the next loop command executes the next singular motion, in this case a step in the y direction to reach the (n+1)th-row, and then starts the next loop for the acquisition of the (n + 1)th-row of the map in the reverse direction, and so on.

---

[5] The scan velocity can reach up to 50 mm/s

[6] The minimum value that can be set, for both step, corresponds the minimum incremental motion (0.25 μm)

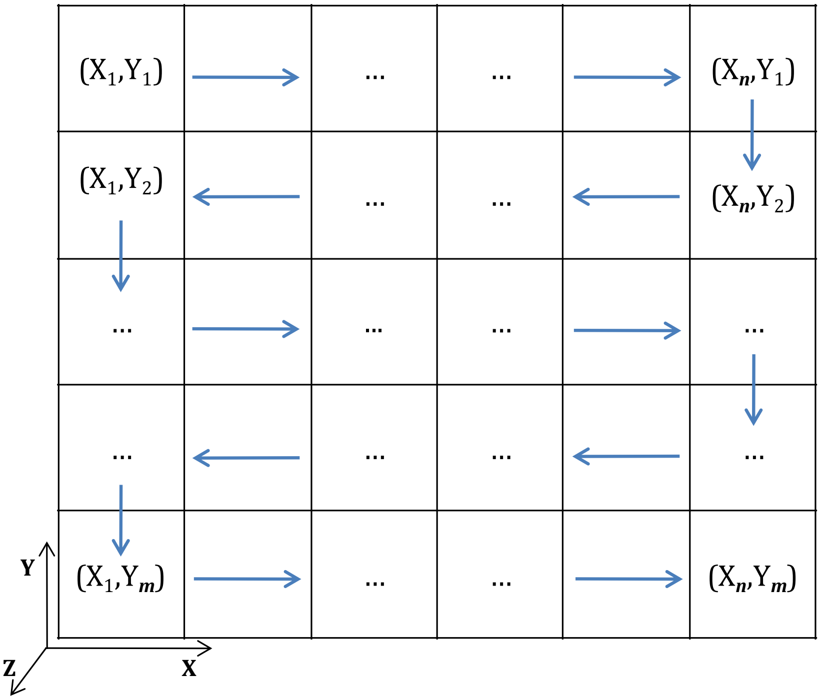

Figure 2.7. Scheme of the loop dedicated to the motion executed along the *x* direction for the acquisition of a map composed by the *n*-row and *m*-column

The selected “step values” (*passo X e passo Y)* define the pixel size, over which data are all summed into a single spectrum. To highlight the influence of the pixel size and the scanning velocity, examples are reported in the paragraph 2.4, after the detailed description of the map acquisition procedures.

2.3. Acquisition software

For data acquisition, the X-ray tube is manually turned on by setting its potential difference and anode current (typical values: 30 kV and 100 µA respectively)[7]. Then, the scan and the acquisition are switched on by the home-made software.

During the raster-scan measurements, for every *X-Y* position, the corresponding energy spectrum is acquired. This is possible because, while the measuring head is continuously moving, the *DT5724* digitizes the detector signals[8]. Each time the linear stage arrives at a position that is a multiple of the preset “step” value, the *X* and *Y* positions and the energy spectrum are stored in a dedicated segment of the memory, called *shared memory big*.

---

[7] This operation can be rather fast (tens of seconds) but some precautions must be taken and the increase in voltage and current should not be “instantaneous” to avoid discharges that might damage the tube

[8] The trigger for data acquisition is internal, i.e., a trigger signal starting the acquisition process is generated when the signal is above a user-defined threshold

All these data are organized in the same way, the events coordinate being written before the energy of the detected X-rays:

$$(x_1, y_1); E1_{11}, E2_{11}, \ldots, EN_{11}$$
$$(x_2, y_1); E1_{21}, E2_{21}, \ldots, EN_{21}..$$
$$\ldots$$
$$(x_j, y_k); E1_{jk}, E2_{jk}, \ldots, EN_{jk}..$$
$$\ldots$$
$$(x_n, y_m); E1_{nm}, E2_{nm}, \ldots, EN_{nm}$$

where x_j is the x position, y_k is the y position and $E1_{\mathrm{jk}}$, $E2_{\mathrm{jk}}$, ..., EN_{jk} the energies of the events acquired in that particular position, Fig. 2.8.

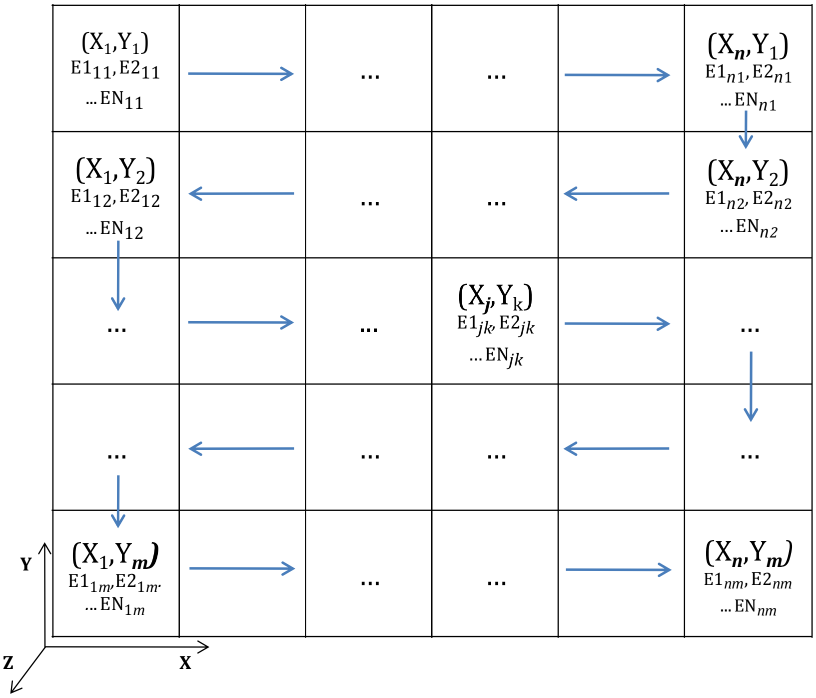

Figure 2.8. Scheme of a XY raster acquisition, with the positions and the energies, in the shared memory segment

As energies and positions could in principle have the same numerical value, we add identifier to their numerical values in µm[9], so that they cannot be misinterpreted as energy data in the successive data processing for the map construction (see next paragraph).

During the acquisition, the time spent in the different points is not always the same. Actually, the measuring head spends more time at the edges of the map, because when the head reaches the end of every row the other coordinate is incremented by the previously defined step, the motion direction is reversed so that the velocity cannot remain constant (both module and direction). Data acquired in the regions where the velocity is not constant, are

---

[9] The identifiers are simply big offsets added to the position values: 50000000 to x coordinates and 60000000 to y coordinates

typically cut away from the maps, to avoid including incorrect information in the elemental distribution.

The acquisition in point mode is performed with the same acquisition code described above and the outputs are stored in a segment of the memory, called *shared memory small*, in order to keep them separated from the big segment, necessary for the elemental mapping analysis.

The *shared memory small* is organized in 16383 channels. When a signal from the detector is digitized, its amplitude is determined and the counts in the channel corresponding to that amplitude are incremented of 1 counts and in this the way the single-point measurement spectrum is constructed. Before the acquisition is started, it is required to provide the measurement time, the predefined measurement time being 60s.

In both cases, when the data acquisition is finished or when the user stops the acquisition, it is possible to save all the data: the interface requests the user to insert a folder name; every file is saved in this folder created on the desktop, as a text file (*File.txt*). After this operation all the shared memory segments, both *big* and *small* ones, are freed up and the system is ready for a new acquisition.

2.4. Elemental map elaboration and GUI

The GUI dedicated to data visualization is divided in two windows (Fig. 2.9), one for the elemental map and another for the spectrum.

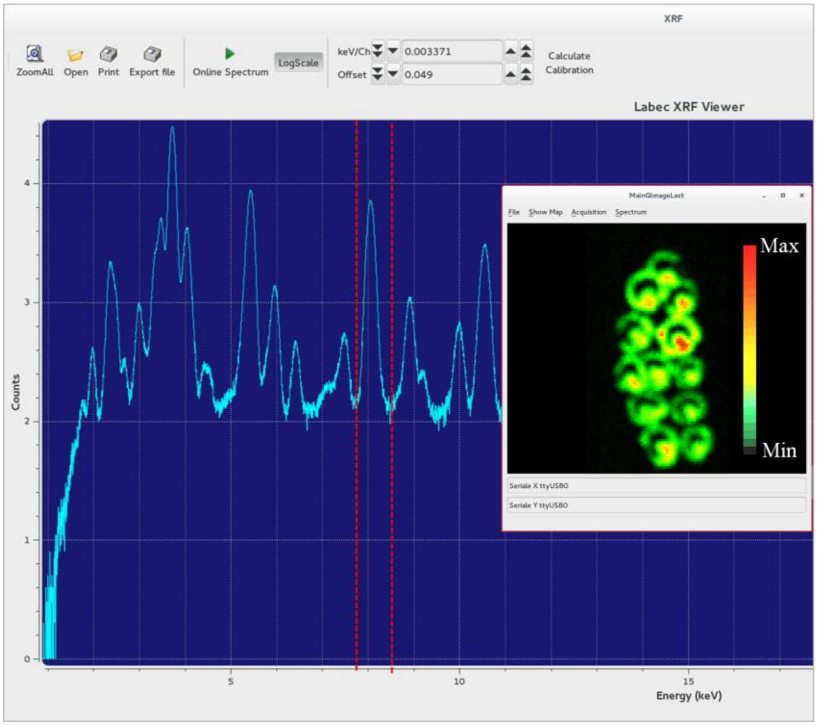

keV/Ch 0.003371

Offset 0.049

Seriale X ttyUSB0

Seriale Y ttyUSB0

Figure 2.9. Software interface of the XRF scanning system. On the right is shown the main window, where a map is visualized, on the left the spectrum window, where the spectrum of a pixel, of a sub-area or of the whole area can be displayed together with the reference RGB scale

To obtain the elemental map we have to simply select a region of interest (ROI) in the spectrum, usually an energy interval corresponding to a characteristic X line of an element such as, for example, the Fe Kα line or Pb Lβ.

Colours in the map are attributed as follows: first, M and m, respectively the maximum and the minimum number of counts in the selected ROI, are determined. The (M-m) interval is divided into 768 sub-intervals, coloured from black (m - colour n. 1) to red (M - colour n. 768). As a consequence, comparing elemental maps obtained from different ROI of the same spectrum, the same colour may correspond to different counts and different colours may correspond to the same number of counts.

When the acquisition button is pushed, both in scanning and point mode, a window opens and displays the online “total spectrum"[10]. The spectrum can be calibrated directly or by using a previous calibration.

After the acquisition, other two options are available: by clicking in a pixel in the map, the *spectrum* of that particular pixel is displayed; by selecting a rectangular area on the map (dragging the mouse), the spectrum of that area is displayed.

Besides the main procedure described above to construct the map, the main software contains additional features that make it more flexible to user demands:

- it is possible to blow up the map size for better visualization of detail;

- it is possible to return exactly to any measured point after a scan, simply by double-clicking on the corresponding pixel in the map. This feature allows to use the elemental distribution map as a guide for single spot analysis. Indeed, the best analytical approach is to perform in scanning mode a pre-analysis of an area of interest and then to select the most suitable point or sub-region, overcoming the problem of regional in-homogeneities, thus avoiding misleading information on the composition of the material under study.

In the following, I report examples of measurements highlighting the influence of the pixel size and the scanning velocity on the elemental maps.

A portion of an illuminated parchment has been analysed; to put into evidence the effect of the pixel size, I repeated the measurements at the same velocity (500 µm/s) but with different pixel sizes (1000 x 1000 μm^2, 800 x 800 μm^2, 500 x 500 μm^2 and 250 x 250 μm^2, as shown in Fig. 2.10), while to evidence the effect of changing the scanning velocity, measurements were performed at the same pixel size (500 x 500 μm^2) but at 2 mm/s and 250 µm/s. Spectra obtained for the two velocities are reported in figure 2.12.

---

[10] The “total spectrum” is the sum of the spectrum acquired in every pixel of the map

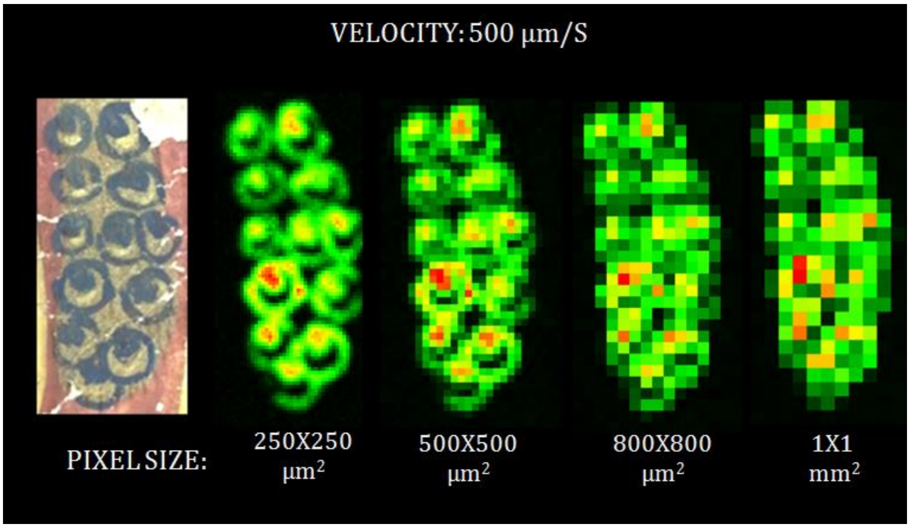

Figure 2. 10. Cu elemental maps of the same area for a velocity of 500 µm/s, obtained only by changing the pixel size from 250 x 250 µm^2 to 1000 x 1000 µm^2

As expected, by decreasing the pixel size, sharper elemental maps are obtained. Indeed, in the map acquired with a pixel size of 250 x 250 µm^2, the blue copper rings can be clearly distinguished, what is not possible with the larger step dimensions: the smaller the step, the finer the details of the target that the system can resolve, of course always being limited also by the beam dimension[11]. Being the beam spot size on sample about 800 µm, lowering the pixel size below 250 µm would not produce any substantial improvement in the information provided by the maps. This conclusion is supported by the intercomparison of the Cu maps acquired on a detail of the peacock tail (the area studied so far) with 100 and 250 µm pixel size (Fig. 2.11).

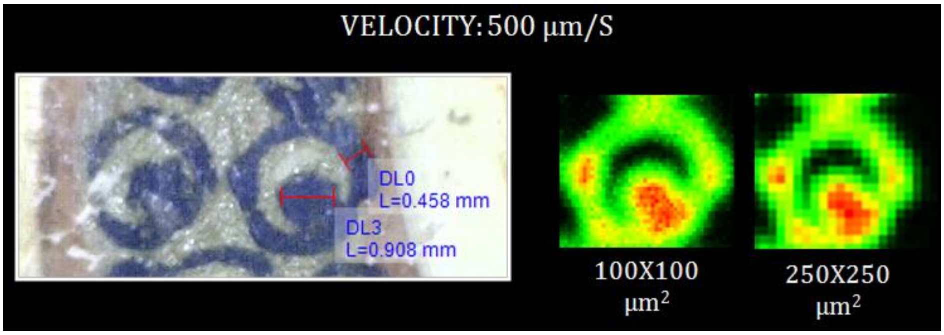

Figure 2. 11. Cu maps acquired on a detail of the peacock tail with 100 and 250 µm pixel size

From the intercomparison of the maps and the optical image of Fig. 2.11, it is apparent that reducing the pixel size we get just a minor improvement of the image quality, at a cost of factor 6 on the measurement time.

---

[11] As it is well known, the spatial resolution depends on both the probe dimensions (in our case, the size of the X-ray beam on the target) and the sampling spatial interval

The comparison between the two maps of figure 2.11 shows that by reducing the pixel size, we get a better image quality (as obvious), but we get only very minor (if any) improvement on the pieces of information provided by the map on the sample structure. In addition the info provided by the two maps on the sample structure is the same: for example, the black area (the “half-moon shaped area”), which corresponds to the inner grey area of the optical image, has the same dimensions in the two maps.

By the comparison of the maps with the optical image (Fig. 2.11), we can see that the “half-moon” dimensions are smaller in the formers than in the latter and actually both the maps fail to find its thin extremities; this is a direct consequence of the fact that the beam size on the sample is bigger of the thin extremities of the “half-moon”.

Thus I can conclude that the spatial resolution of the scanner is not sufficient and for such a fine scale study we need a higher spatial resolution. Therefore to allow for high spatial resolution, in the second generation XRF2 scanner set-up, described in the conclusion, collimators of different sizes (400 and 800 µm) can be used. A further improvement, not yet available, will be the possibility of using also a polycapillary lens, as detailed in the perspectives.

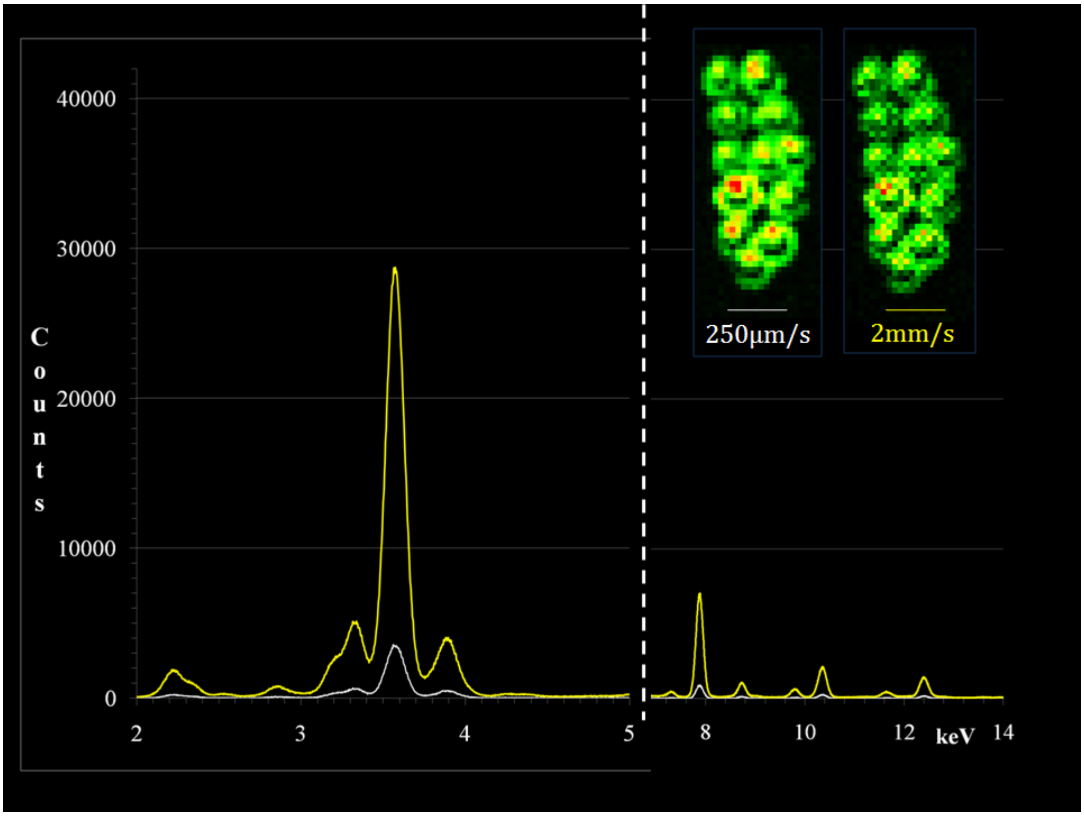

Figure 2. 12. Spectra of the same area as before, 500 µm pixel size, obtained with 2mm/s and 250µm/s scanning velocities

As far as the scanning velocity is concerned, lower values result in higher counts, since the corresponding spectrum is accumulated for a longer time. This is clearly visible in figure 2.12, where the energy spectra are reported for two scanning velocities. As expected, a direct proportionality between peak areas and velocities is observed and indeed for the Cu Kα line we have areas of ~ 48900 ± 200 counts for 2 mm/s and of ~ 388700 ± 600 counts for 250 µm/s, respectively, which scale accordingly with the velocity, within the experimental errors[12]. Lowering the scanning velocity increases the contrast in the map and possibly the number of visible details. Actually, statistical fluctuations do affect the pixel colour attribution and by increasing the number of counts per pixel we make these fluctuations relatively less influent. In this way, by lowering the scanning velocity, a better defined map is obtained.

---

[12] The error on the number of counts is largely due the statistical fluctuations, given by the square roots of the counts.

CHAPTER 3

The XRF2 scanner for Cultural Heritage applications

Accurate understanding of user needs is essential in developing successful products [27;28]. Studies of the origins of successful innovations have indicated that external sources are important inputs to the innovation process. These external inputs have been found to arise from a wide range of sources, including users, academia, suppliers, competitors and research laboratories. In particular, users or customers have shown to play an important, and sometimes dominant, role in the innovation process [29]. Indeed, good design and successful innovation are intimately linked to early and close consultations between the producer and representative customers, both in pre- and post-launch phases.

Innovation in response to user needs is prominent in scientific instruments, because scientists have a great deal to gain from involving the user in the design and development process. Indeed analysis of need and solution data lead from users can improve the productivity of new instrument development with rapid changes [30].

Feedbacks from users, through the use of the instruments, may range from the identification of faults, limitations and alternative uses, to the design and development of technical solutions, in order to overcome such limitations and to improve performances. This last paragraph perfectly describes the core of my PhD activity.

Thanks to the results obtained working with the XRF1, as shown in the previous chapter, it was possible for me to point out pros and cons of this first prototype, basing on CH samples measurements and observations, comments and notes from conservation scientists, physicists, chemists, restorers and art historians I was working with during the many measurement campaigns.

On the basis of these indications, several hardware and software developments were implemented in order to overcome the evidenced limitations. Therefore the second generation XRF2 scanner was designed and implemented for obtaining a more powerful instrument, suitable for studying samples with non planar surfaces, with an extended range of low-Z detectable elements, characterized by an acquisition interface allowing for an interactive optimization of the acquisition parameters. A lot of efforts have also been dedicated to improve the system in order to obtain a compact, lightweight, easy to handle and to use instrument.

My work for the software/hardware scanner development was performed in collaboration with the physicist co-workers of the Labec (especially Caroline Czelusniak and Lara Palla) in Florence and with the scientific group of the New York University in Abu Dhabi.

Tests were carried out on standard laboratory samples and on real Cultural Heritage case studies, to verify the correct functioning of the developments made to the XRF2 scanner and evaluate the extended capabilities of XRF2. The analyses carried out on CH samples have been possible thanks to many collaborations, as detailed in Chapter 4.

In this chapter I will focus the attention on the most relevant scanner upgrades, both for hardware and software, and the applications in the CH field highlighting their effectiveness.

3.1 Instrumentation and GUI

The new XRF2 scanner (Fig. 3.1), smaller and lighter than the previous one (Par. 2.1), and thus more easily transportable, was developed. The measuring head and motors have the same configuration as before, instead the total dimensions of the power supplies box are reduced from 70 x 50 x 35 cm^3 to 60 x 35x 5,5 cm^3. In addition, instead of an aluminium box, a carbon-fibre box was now used, much lighter and resistant, which allows for decreasing the overall system weight from 20 to 11 kg.

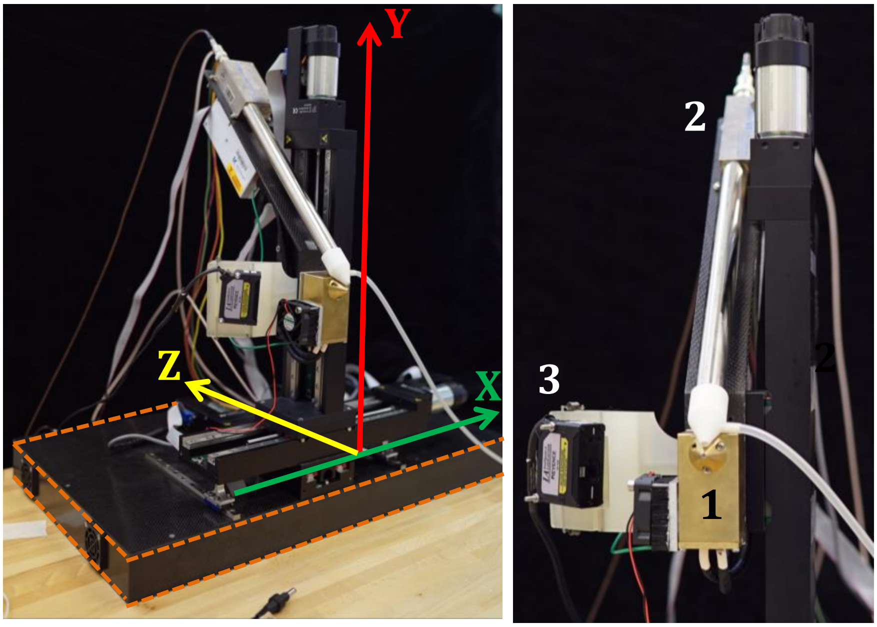

Figure 3.1. XRF2 spectrometer: on the left, the 3-axis motion system (horizontal X-axis in green; vertical Y-axis in red; lengthwise Z-axis in yellow) and the carbon-fibre support of the system (orange dotted line), which contains the desktop digitizer, the motor controllers and all the power supply units; on the right, a detail of the measuring head (1. X-ray tube, 2. SDD detector, 3. dynamic positioning system)

Basing on the experience gained in these years working with non-trained personnel, it has become clearer and clearer that the procedure for starting the scanner has to be extremely robust, as many mistakes can be done (such as, for example, wrong order of function activation or request of activating a function when the system is still executing the previous one), which can induce malfunctioning or even cause the system to hang up. To prevent users' mistakes, the system is now started by exploiting a step-by-step procedure, where no freedom is left to the user: the procedure activates every function following the correct order and assigning them the proper time to be executed, during which the system is not available to any other request from the user. In this way the user is forced to follow the correct "work flow".

A new GUI has been developed, simplified with respect to the previous one, in order to make it more "user-friendly". In the current version of the GUI, the three main functions[1] (initialisation, point motion and continuous motion, red boxes in Fig. 3.2), and all the new functions (see below) are integrated in the same window.

To exemplify the above, the new version of the procedure seen in Chapter 2 for starting the scanner is described hereafter.

---

[1] The main macro functions remain unchanged from those extensively described in chapter 2.2

Currently, when the user starts the program, only the *TTY_XY* tab is enabled, as shown in Fig. 3.2 a, which solely allows establishing the USB communication between the motors and the control PC. After this procedure is accomplished, the initialization function is enabled and the program shows the *Init* tab in the active status, as displayed in Fig. 3.2 b. It is now possible to proceed to the next step, in which the motors are initialised. Only when the initialisation is finished, the motors are ready and the tabs *Move_XY* and *Scan* are activated (Fig. 3.2 c - d) and become available to the user.

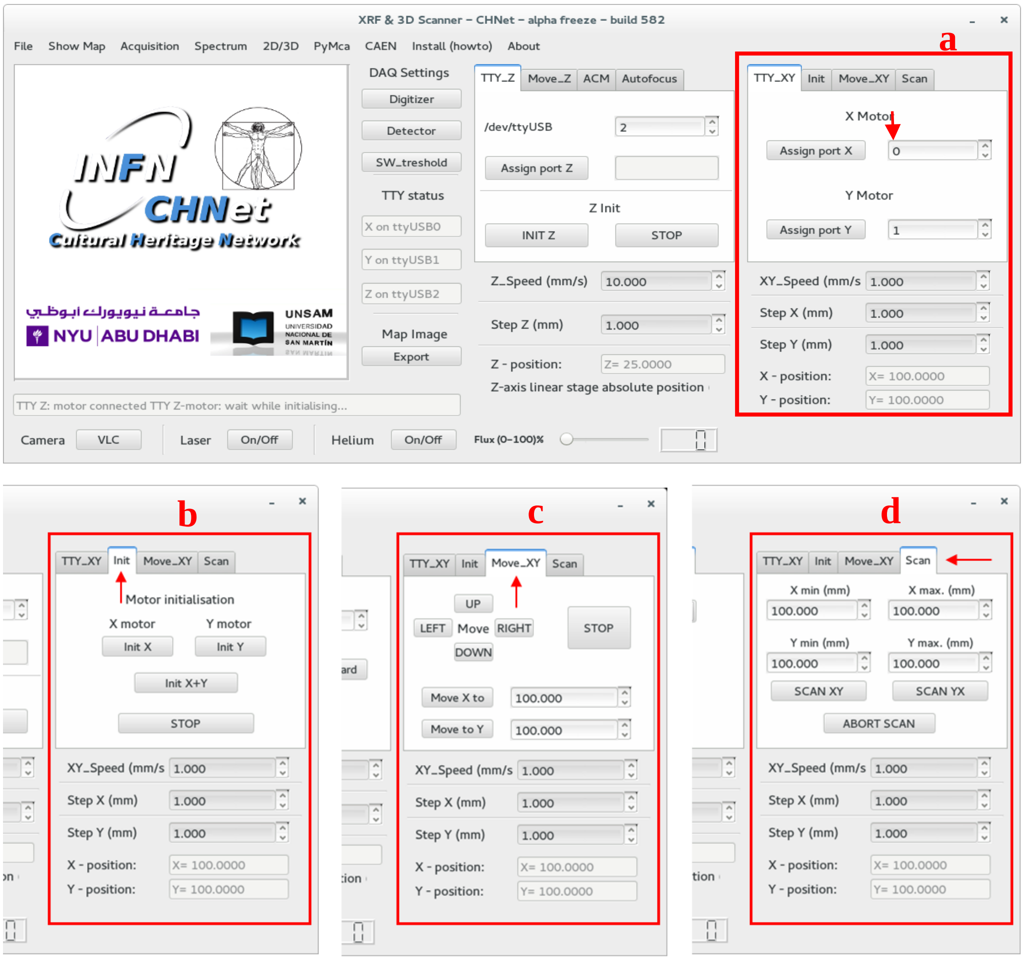
XRF & 3D Scanner – CHNet – alpha freeze – build 582

/dev/ttyUSB 2

X on ttyUSB0

Y on ttyUSB1

Z on ttyUSB2

Z_Speed (mm/s) 10.000

Step Z (mm) 1.000

Z - position: Z= 25.0000

Z-axis linear stage absolute position

TTY Z: motor connected TTY Z-motor: wait while initialising...

Assign port X 0

Assign port Y 1

XY_Speed (mm/s 1.000

Step X (mm) 1.000

Step Y (mm) 1.000

X - position: X= 100.0000

Y - position: Y= 100.0000

Move X to 100.000

Move to Y 100.000

X min (mm) 100.000

X max. (mm) 100.000

Y min (mm) 100.000

Y max. (mm) 100.000

Figure 3.2. View of the panels shown by the GUI at the beginning of the scanner activation procedure, in the time order in which they are activated (only c and d are contemporaneously activated): (a) USB port allocation, (b) initialization of motors, (c) linear motion of the stages, (d) scanning mode acquisition interface

3.2 Dynamic positioning system

As it is well known, XRF analyses, both in single point and in scanning modes acquisitions, are normally constrained to flat, planar surfaces. Actually almost all the applications carried out with XRF1 scanner during my PhD work have dealt with such samples, both in technological and in CH fields.

In our set-up, variations in the distance between the measuring head and the sample surface (Z-axis)[2]:

- change the primary beam dimension on sample;
- change the primary beam energy spectrum on sample;
- cause the axes of the primary beam and of the detector not to converge in the same point on the sample surface;
- change the detection solid angle;
- change the detected X-ray spectrum.

In conclusion, if the detection geometry varies, it is not possible to compare spectra obtained from different areas of the sample, as the same composition can result in different spectra and the same spectra can be ascribed to diverse compositions.

For many reasons in CH field it is frequent to find artworks with non-flat, non-planar surfaces. This may be due to artworks manufacturing, for example in the case of 3D objects or in the presence of three-dimensional decorations (see Fig. 3.6), or to degradation and aging phenomena, which can deform the surface (see Fig. 3.8) of the most part of support materials (wood, canvas, paper, parchment, wall, and so on). In addition, should samples exhibit irregularities or deformations (z-variation) greater than the very short working distance (~6mm), the measuring head of the scanner might even collide with the sample. This is of particular relevance for CH applications, where artworks are usually of great value and possibly fragile, so that any possible damage must be absolutely avoided.

In order to overcome the above-mentioned limitations, a part of the three years of my PhD was spent to equip the XRF2 prototype with a dynamic positioning system based on a laser telemetry sensor directly connected with the Z scanner stage[3] (Fig. 3.3). A positional feedback from the telemeter was used to automatically keep the scanner-to-specimen distance constant during the scan. With this positioning control system, the XRF scanner capabilities are extended, indeed now analyses can be performed for a widened range of sample geometries, without posing risks to analyzed specimens or sacrificing data quality.

---

[2] The set-up and geometry of the measuring head of the XRF2 remain unchanged from those of the XRF1, therefore the working distance, previously explained in Fig.2.1 of Chapter 2.1, is still as before ~6 mm

[3] The Z motor range is 50 mm, less than those of the X- and Y-stages

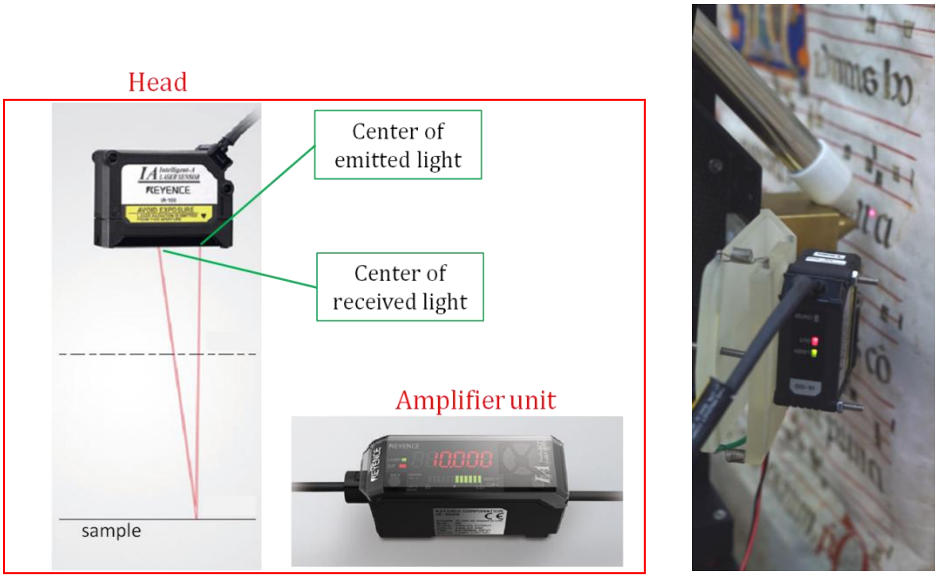

Figure 3.3. In the red square: the dynamic positioning system, composed by a laser triangulation sensor (head) and an amplifier unit; on the right, the final set-up of the upgraded instrument. The red light spot visible on the parchment surface is the spot of the laser beam exploited by the telemeter to adjust the distance

The dynamic positioning system is composed by a lightweight (130 g) analogue CMOS laser sensor (Keyence IA-100, Fig. 3.3 - left), an amplifier unit (Keyence IA-1000, Fig. 3.3 - centre) [31] and an Arduino ADC board (not shown) [32], which is connected via USB connection to the control PC. The sensor unit is mounted on the measuring head, as shown in Fig. 3.3 - right, in such a way that:

1) the sample-to-sensor distance[4] is 10 cm when the scanner is at ~6 mm (the working distance) from the sample;
2) the laser spot[5] and the X-ray beam coincide on the sample surface.

As shown in Fig. 3.3 - left, the sensor triangulates a laser beam (655 nm emission wavelength) to precisely determine the distance to the target, with an overall error less than 10 µm [31]. The signal output from the sensor is channeled to the amplifier unit, after which the Arduino ADC board performs the analog to digital conversion. Thanks to the internal calibration, this number corresponds to a distance, which is used by the scanner software to adjust the distance along the lengthwise Z axis and thus to keep constant the measurement geometry [41].

---

[4] The telemeter system can keep the sample-to-sensor distance constant if the distance varies in the (-25 mm; +30 mm) range around the reference distance R_d = 100 mm

[5] Laser spot dimensions are about 400 × 1400 µm^2, at the sensor-to-sample reference distance Rd = 100 mm

The autofocus software is composed by four main functions: *TTY_Z (Initialisation)*, *Move_Z*, *ACM* and *Autofocus*. Each of them is called from the same GUI interface, as shown in Fig. 3.4.

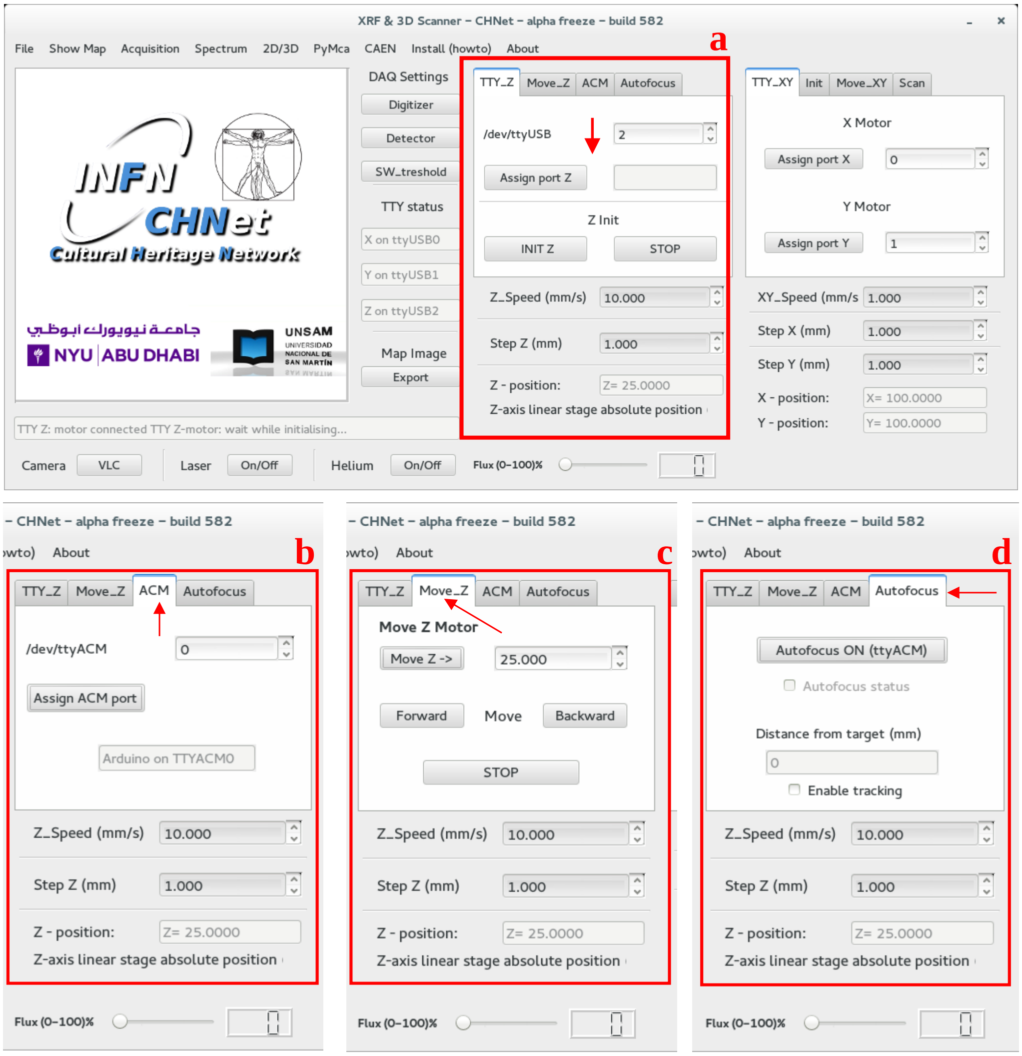

X on ttyUSB0
Y on ttyUSB1
Z on ttyUSB2
TTY Z: motor connected TTY Z-motor: wait while initialising...
/dev/ttyUSB 2
Z_Speed (mm/s) 10.000
Step Z (mm) 1.000
Z - position: Z= 25.0000
Z-axis linear stage absolute position
X Motor: Assign port X 0
Y Motor: Assign port Y 1
XY_Speed (mm/s 1.000
Step X (mm) 1.000
Step Y (mm) 1.000
X - position: X= 100.0000
Y - position: Y= 100.0000
/dev/ttyACM 0
Arduino on TTYACM0
Move Z -> 25.000
Distance from target (mm) 0

Figure 3.4. View of the GUI interface: (a) initialisation , (b) the allocation page for the ACM port, (c) linear motion of the stages, (d) autofocus interface

The macro-functions *Initialization* and *ACM* assign different USB ports to the Z motor stage and to the Arduino ADC, in order to allow the communication between them and the PC, thus avoiding conflicts.

As for the elemental mapping software (paragraph 2.2.3), when the PC connection with the Z stage is established (*Assign port Z)*,the button *INIT Z* (Fig. 3.4 a) can be pushed. In this way the initialization function is called, in order to move the stages to the initial reference position, corresponding to the middle of the motion stage range (Z=25 mm). After this operation is accomplished, the “*Move_Z”* and “*Autofocus"* tabs are enabled, and the positioning system can work.

The motion function called by the “*Move_Z”* tab is the same used for the linear motion of X- and Y-stage, already explained in paragraph 2.2.2.

The core of the pointing system is the *Autofocus* function, which effectively allows the interaction between the positioning system and the Z stage. The laser sensor measures the target-to-sensor distance every 10 ms and our software determines the mean deviation from the user-set “zero-point”, which corresponds to the working distance. This mean deviation value is the average calculated from every two successive values read from the sensor, and it is used by the *Autofocus* function to automatically regulate the working distance, continuously moving the Z motor toward the preset ”zero point”. For a more effective feedback action, an algorithm manages the Z velocities: small deviations in system-target distance are corrected at low velocities, while larger deviations at high velocities, etc. In our case, deviations smaller than 0,2 mm from the zero-point are compensated at 0,1 mm/s, while deviations greater than 5 mm are corrected at 5 mm/s.

In order to prevent any possible samples damage, various safety mechanisms have been included in the control software. For example, should the laser sensor lose sight of the sample or the measured deviation at any point exceed 15 mm, the motion of the Z-motor will be instantly halted. To further enhance the safety of the system, the GUI also includes an emergency *STOP* button, which allows for immediately stopping the Z motion.

3.2.1 Lead block test

Before using the laser tracking system on true CH samples, I have tested it on laboratory samples. In this test, a lead block with the front surface not parallel to the scanning plane (~ 30° angle between the two planes) was put in front of the instrument, as shown in Fig. 3.5 - left.

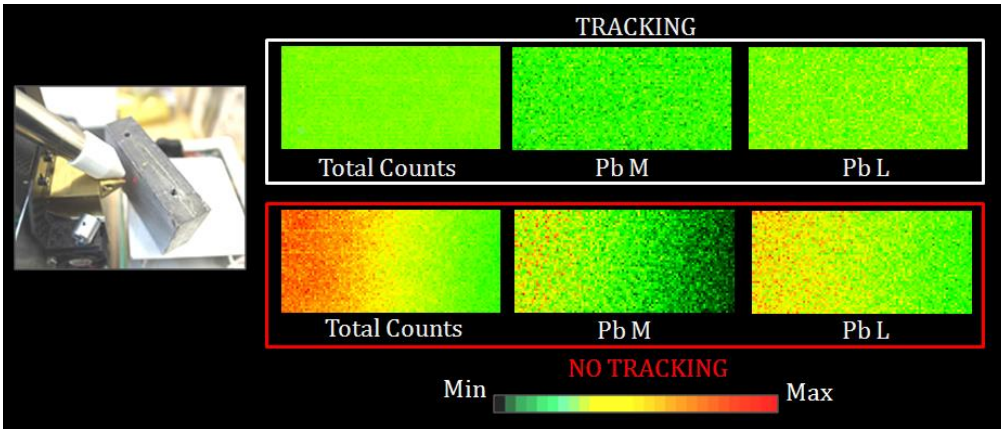

Figure 3.5. Experimental set-up for diagnostic test on angled lead block (on the left) and elemental distribution maps of total X-ray counts, Pb L*α* (10.55 keV) and Pb M*α* (2.34 keV) spectral lines, acquired with and without the tracking system, respectively

Tests performed by disabling the tracking system show noticeable variations in the elemental distribution maps (as shown in Fig. 3.5 - “No Tracking”). The intensity reduction in the right-hand side of the maps is particularly evident for the Pb low-energy X-rays (M*α* 2,34 keV), owing to the increased absorption in air (the higher the distance the greater the absorption) and to the misalignment of the detector and the primary X-ray beam (the detector and the X-ray beam axes converge at 6 mm from the end of the X-ray collimator nozzle); for different distances, the detector aims at a point different from the irradiated one and the detector efficiency is lowered or even nullified).

Instead, as hoped, the laser tracking system allowed for acquiring homogeneous elemental maps of the scanned area (as shown in figure 3.5 - “Tracking”).

3.2.2 Tests on the Madonna con bambino

These first successful results supported this approach and encouraged me to verify the effectiveness of the laser tracking system also on authentic CH samples. Thanks to the collaboration with the restorers of the *Opificio delle Pietre Dure*, I had the opportunity of applying the XRF2 scanner to the study of the ”*Madonna con Bambino*”, by unknown author of the 13th century. The problem for the analysis of this painting is exactly the same as for the lead block. Indeed, as frequent in that period, the Virgin’s head and the body are painted on two different non-coplanar panels (Fig. 3.6a). For the XRF measurements, the panel with the Lady’s body was kept vertical, so that the panel with the Virgin’s head jutted out towards the instrument, up to ~ 6 cm. The analyses on the head details were conducted putting the scanner at the working distance (~ 6 mm from the surface) when the scanner was aiming at the upper part of the region of interest. In this way, it was possible to analyze all the other parts of the region under study without any risk of hitting the sample when the tracking system was off, as the sample-to-scanner distance could only increase. Results are shown in figure 3.6 b.

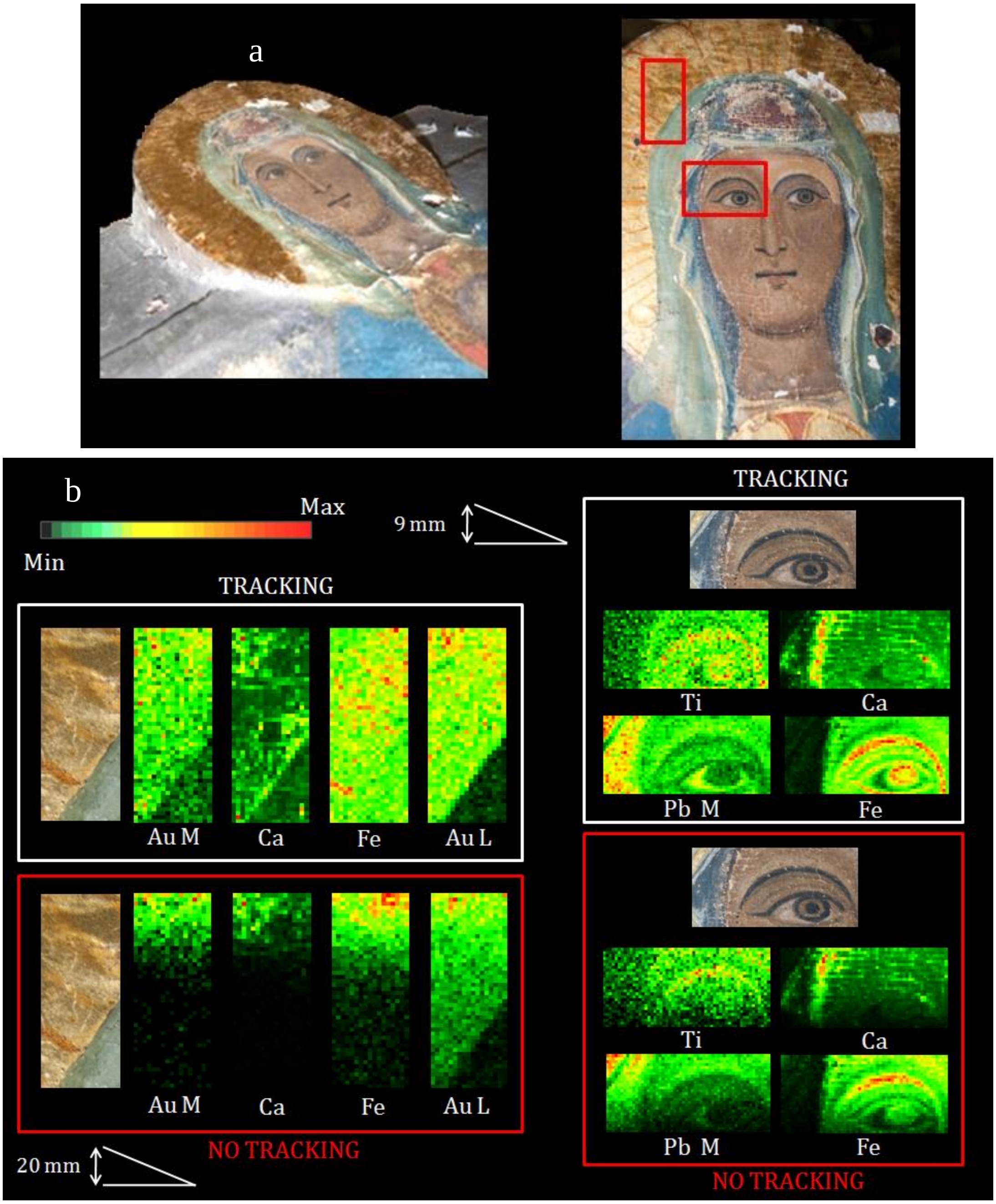

Figure 3.6. (a) On the left, the lateral view of the artwork, which allows appreciating how much the inclined panel juts out. On the right, details of the painting front view, in which the red squares highlight the investigated areas; (b) XRF elemental maps of the two analysed areas, acquired with and without the tracking system. The area "halo" is 2 x 5 cm^2 with a lengthwise (Z axis) variation of 20 mm, while the region "eye" is 6 x 3 cm^2 and corresponds to a lengthwise variation of 9 mm, as shown in white in the upper and lower part of the figure

In Figure 3.6 b, the differences between the measurements with and without the tracking system are clearly evident. Inhomogeneities in the maps, due to X-ray absorption and detector misalignment, are more evident in the maps of the “halo” than in those of the “eye”, as there has been a higher distance variation along the Z axis in the former than in the latter case (~ 20 mm and 9 mm respectively).

In contrast, with the tracking system active, X-ray intensity does not suffer of any alteration induced by the non-flat surface. This allows for correct pigment identification throughout the whole area; for example in case of the eye it was possible to asses that the brown pigment used is a brown ochre, a Fe rich pigment with Ti impurities, as the Ti and Fe maps show the same distribution and the same main structures.

The intensity attenuation with increasing distance is particularly relevant for the low-energy X-rays, such as the 2,12 keV Au M, the 2,34 keV Pb M and the 3,69 keV Ca K lines, for which we can even have a complete absorption, with consequent loss of information, as is the case of the lower part of the “halo” maps, corresponding to bigger sample-to-scanner distances. However, also medium-high energy lines are noticeably attenuated at the bigger distances, as it can be noted for example in the lower part of the 10,55 keV Pb L line.

These observations become apparent when looking at the spectra, such as for example those acquired on the area of the Virgin’s eye, with and without the tracking system (Fig. 3.7). In this case the maximum distance variation along the Z axis that the tracking system has to compensate is 0,9 cm, as already mentioned above.

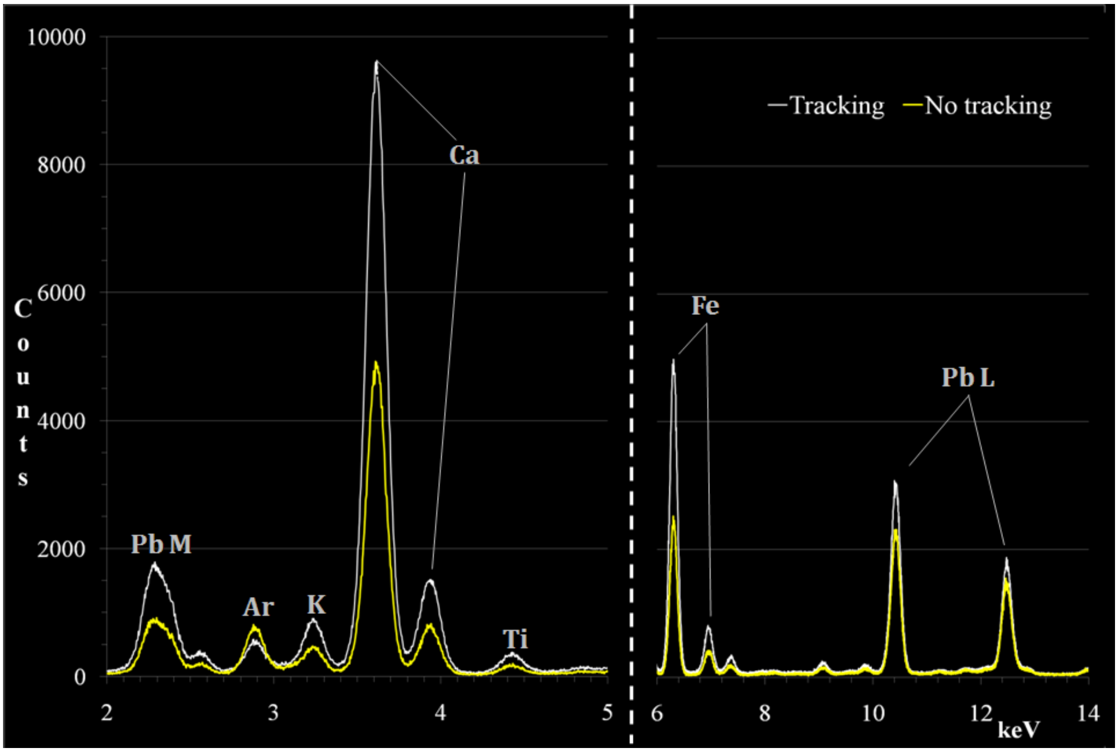

Figure 3. 7. Spectra of the area acquired on Virgin's eye, with and without the tracking system

All the peaks of the spectra acquired with the tracking system are higher than those acquired without the tracking system and the differences are smaller at higher energies (compare for examples the differences between the Fe and Pb L peaks in the two conditions).

To quantify the above-mentioned behaviours, in Tab 3.1, I report the peak areas of the elements of interest for the spectra in Fig. 3.7.

Element	**Energy (keV)**	**No tracking (Counts)**	**Tracking (Counts)**
Pb M	**2.34**	**26900**	**49400**
Ar	**2.95**	**34900**	**27300**
K	3.31	21300	42200
Ca	**3.69**	**222700**	**442200**
Ti	**4.51**	**10700**	**21300**
Fe	**6.39**	**44800**	**91400**
PbL (L3M5)	10.55	145900	187200

Table 3. 1. Peak areas of the elements of interest obtained scanning the same area (Virgin's eye in Fig.3.6) with and without the tracking system. In green, we report the elements whose spatial distribution are shown in figure 3.6

As it can be seen, all the peaks areas increase when passing from the “no-tracking” to the “tracking” configuration. In particular, we roughly have a factor 2 in the ratio of the “tracking/no-tracking” peak areas for all the elements up to Fe, for which this effect is more severe. This ratio gets then lower and lower with increasing X-ray energies and actually it decreases down to 1,3 for the Pb L lines. Only the Ar peak decreases when passing from the “no-tracking” to the “tracking” configuration and therefore the ratio gets lower (0,8). This is reasonable because without the tracking system the primary X-rays air-path increases and thus more Ar X-rays are produced. As a whole, the spectra alterations due to the irradiation and detection geometry variation can determine a wrong reconstruction of the sample composition and are thus to be avoided with the utmost attention.

3.2.3 Tests on an illuminated parchment

As in CH field most of the artwork supports, such as parchment, canvas and paper, are characterised by surfaces often uneven and/or undulated, the second test on CH samples was carried out on an illuminated parchment, crumpled with wrinkles and deformation up to 2 cm (Fig. 3.8), as a consequence of aging and/or alteration phenomena occurred to the vellum sheet[6]. The analysed illuminated manuscript, dating from about AD 1340, consists of a vellum sheet, partly restored at an unknown date (for more details see Chapter 4). This case is by far more difficult than the previous one, because distance variations occur randomly, changing abruptly from point to point, and the maximum distance variation along the Z axis that the tracking system has to compensate is 2 cm (Fig. 3.8).

---

[6] Parchment is made of processed animal skin and consists mainly of collagen proteins, which forms *fibres*. These collagen fibres are stabilized by intra and intermolecular cross-links and hydrogen bonds. Under unfavourable storage conditions (heat, humidity, light and air pollutants), these links can break, leading to deterioration of the collagen structure. Ageing conditions, in fact, can induce changes of the intra-fibres structure; in particular, hydrolytic or oxidative phenomena can cause the breaking of the collagen backbone chains and generate fibre cracks, up to the macroscopic evidence of denaturation, when the fibres contraction takes place (shrinkage). Many aspects of parchment deterioration can be related to changes occurring to the collagen fibres and in its molecular structure, causing changing in parchment physical macroscopic properties

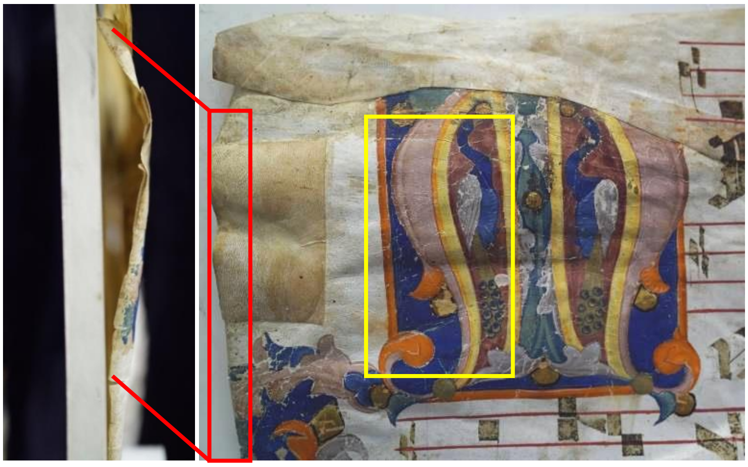

Figure 3.8. Lateral and frontal images of the parchment, highlighting the magnitude of the wrinkles and deformations. In yellow, the portion of the calligraphic initial selected for the analysis is shown

A 55 x 95 mm portion of the calligraphic initial, shown in Fig. 3.8, was selected for my tests, as the majority of the illuminated peacock's body lies in correspondence of a ”bump”, which juts out of ~ 1,2 cm, thus making the analysis really challenging for the tracking system. The corresponding elemental maps, ordered from low- to high-energy, are presented in Fig. 3.9.

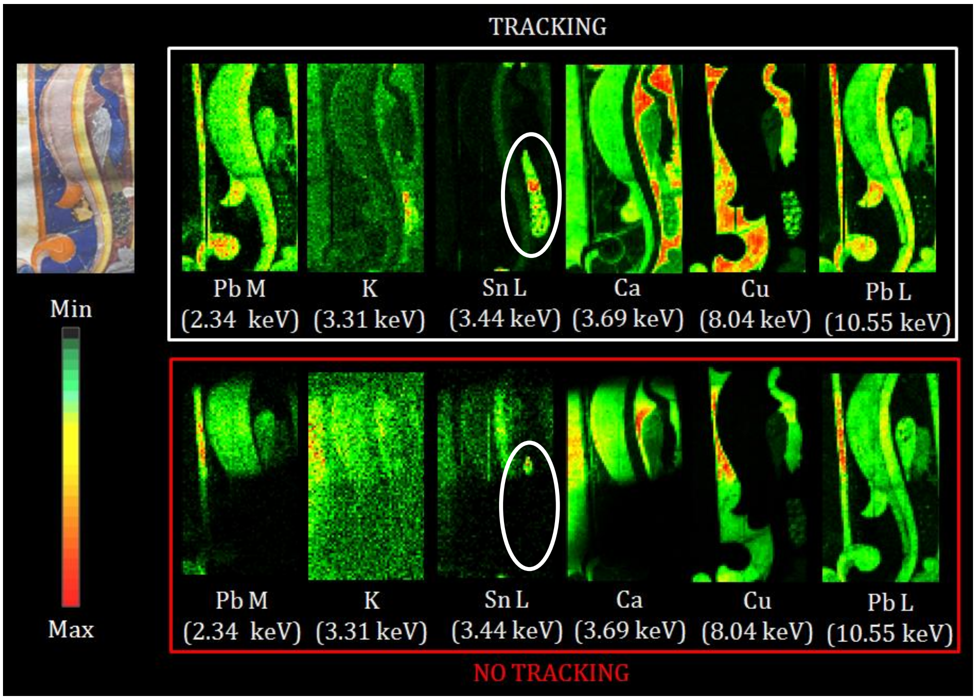

Figure 3.9. Optical image of the scanned area and the most interesting elemental maps, from low to high energy, acquired with (top row) and without (bottom row) the laser tracking system

The maps acquired when the tracking system is active do not show "abnormal" attenuation in any part of the maps. The tracking system prevented the loss of information in the lower part of the scanned area and allowed for a detailed characterisation of the materials employed for the illumination, such as pigments, gildings and for the restorations throughout the scanned area (for more results see Chapter 4).

On the other hand, without the tracking system, the maps extracted from the lower-energy lines (Pb M, K, Sn L and Ca) have the correct intensity only in correspondence to the parchment "bump" (upper half of the area), where the sample-to-scanner distance has roughly the correct value. Instead, where the parchment is concave (lower half of the area) the sample is more distant and the low-energy X-rays are more absorbed. Similar considerations can be drawn also for medium-high X-ray energies, such as Cu and Pb L, for which the absorption effects becoming less and less evident at increasing X-ray energies, as it can be noticed by the Cu and Pb L maps in Fig. 3.9.

These above-mentioned behaviours become apparent when looking the "total spectra", shown in Fig. 3.10, related to the whole scanned area of Fig. 3.9, obtained with and without the tracking system active.

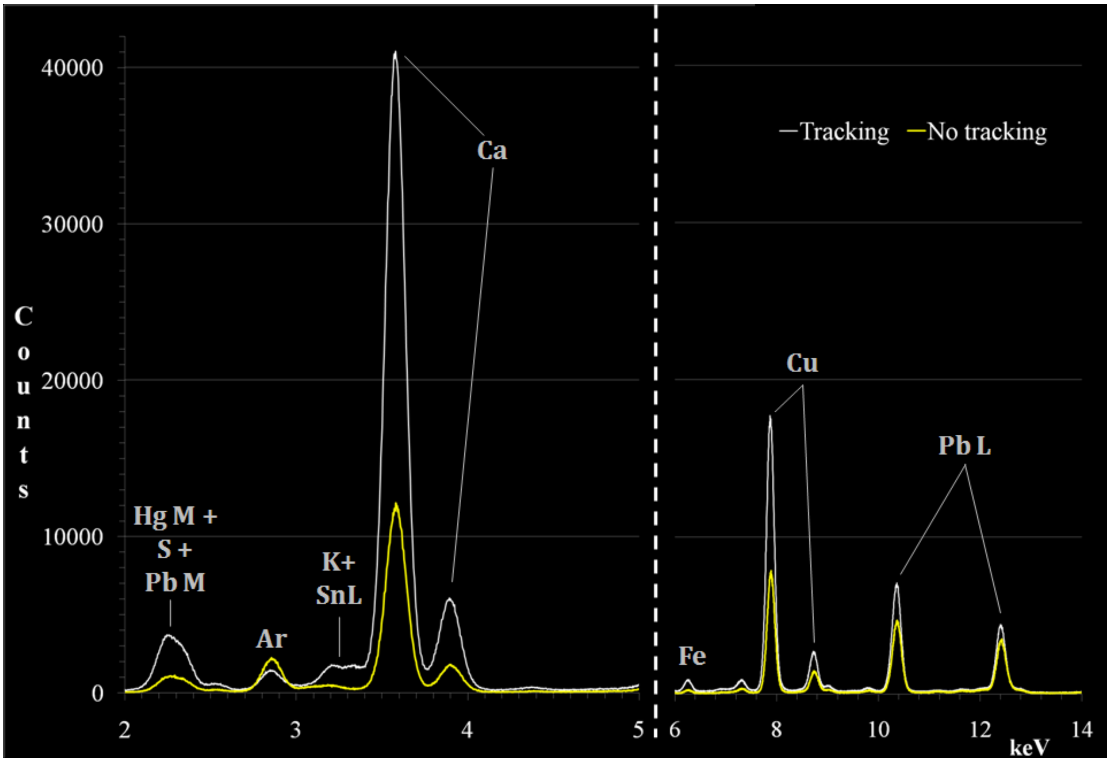

Figure 3.10. Spectra of the area acquired on the illuminated calligraphic initial, with and without the tracking system

By comparing the two spectra we can appreciate that all the peaks of the “Tracking” spectrum (white) are higher than those of the “No tracking” one (yellow), apart from Ar, for which, as in the example of the previous paragraph, the air target increases. Also in this case the differences get smaller at higher energies (compare for example the differences between the Ca and Pb L peaks in the two conditions).

To quantify the above-mentioned behaviours, in Tab 3.2, I report the peak areas of the elements of interest for the spectra in Fig. 3.10.

Element	Energy (keV)	No tracking (Counts)	Tracking (Counts)
Pb M	**2.34**	**38100**	**124600**
Ar	**2.95**	**99200**	**68300**
K	**3.31**	**19600**	**70100**
Sn L	**3.44**	**10600**	**75500**
Ca	**3.69**	**545700**	**1813000**
Cu	**8.02**	**466100**	**1041400**
PbL (L3M5)	**10.55**	**318900**	**440200**

Table 3. 2. Peak areas of the elements of interest obtained scanning the same area (calligraphic initial) with and without the tracking system. In green, we report the elements whose spatial distribution are shown in fig 3.9

As it can be seen, all the peaks areas increase when passing from the “no-tracking” to the “tracking” configuration, apart from the Ar peak, for which the same considerations presented in the previous example on the “*Madonna con bambino*” can be drawn. In this case, the ratios of the “tracking/no-tracking” peaks areas for the elements of interest varies from 7,1 for low energy X- rays (Sn L line) down to 1,3 for the higher X-ray energies (Pb L line). It can be noted that the ratios for the low energy X rays vary more than in the previous example on the Virgin’s eye. This effect has multiple causes, as explained in par. 3.2, the most important of which are, in this case:

- the detector geometrical misalignment and the air absorption are more severe in this case than in the previous of the Virgin’s eye because of the increased length along the Z axis when the tracking system is not active. As far as air is concerned, for the low energy Pb M X-rays, the transmission factor is ~ 0,7 for a distance of 0,9 cm (as in the case of the “eye”) and only 0,4 for a 1,2 cm distance (illuminated initial);
- in the area of calligraphic initial, materials have distributions by far less uniform than the “Virgin’s eye” area.

A case where the above-mentioned effects are both present and have heavy influence, is the case of the Sn distribution in the peacock's tail, whose peak area shows the greatest variation (tracking/no-tracking ratio ~ 7). The tail is present mainly in the lower concave part of the scanned area (white circle in Fig. 3.9) where Sn X-rays cannot be detected if the tracking system is not active (greater sample-to-scanner distances), which explains the lack of the tail in the no tracking Sn map.

In conclusion, the reported tests have shown the power of the tracking system. Indeed, the XRF scanner capabilities are now extended: analyses can be performed for a wide range of non-planar sample geometries, without posing risks to analyzed specimens or sacrificing data quality.

3.3 XRF2 high-performance acquisition system

In collaboration with the physicists of my group, a new high-performance, dedicated acquisition system was developed for the second generation XRF2 scanner. The major hardware upgrade has been the adoption of a new ADC (DT5780- 100MS/s, 14 bit by CAEN) [33], with improved performances. Now, the detector is directly powered by the digitizer itself, thanks to the remotely-controlled high-voltage output, which allows setting up the detector from afar, an option not available in the previous XRF1 scanner (see paragraph 2.1). In this new configuration, it is now possible to easily power on the detector by simply pushing the button "*Detector*" in the *DAQ section* of the new GUI (red square in Fig. 3.11). This option allows for a much faster, easier and safer starting of the scanner, as now it is not any more necessary moving the control computer to the detector, an operation which can be very difficult in some experimental conditions, such as when working on scaffoldings, unstable structures or in hardly accessible sites. This improvement has also allowed for increasing the compactness and lightness of the instrument, reducing the number of power supplies.

As already said also in the description of the XRF1 (paragraph 2.1), the DT5780 digitizes the detector signals and sends it to the control PC, via optical link. The digitizers of both XRF1 and XRF2 allow the user to change the signal acquisition parameters according to the detector characteristics, visualizing in "real time" the effect of the parameter changes. This enables the acquisition of signals from diverse detectors still using the same hardware.

In the XRF1, after optimizing the acquisition parameters for the detector in use by using a program (DPP-PHA) external to our acquisition software, the so-obtained parameters are inserted by the operator into our C++ main acquisition program, which has to be recompiled to obtain the proper executable file. At this point, these parameters are directly loaded by the acquisition software each time a new acquisition started. As this procedure resulted unusable by non-trained personnel, in the XRF2, the configuration procedure has been made straightforward. Indeed, all the parameters for detector signal manipulation can be directly modified in the window opened by the button "*Digitizer*" in the *DAQ section* of the new GUI (Fig. 3.11).

The last command in the *DAQ setting* corresponds to the *"Threshold"* button. It allows setting a low level threshold for the digitizer to get rid of the small-amplitude signals, typically due to electronic noise, which produces unnecessary digitizer dead-time, thus interfering with the acquisition of the sample signals.

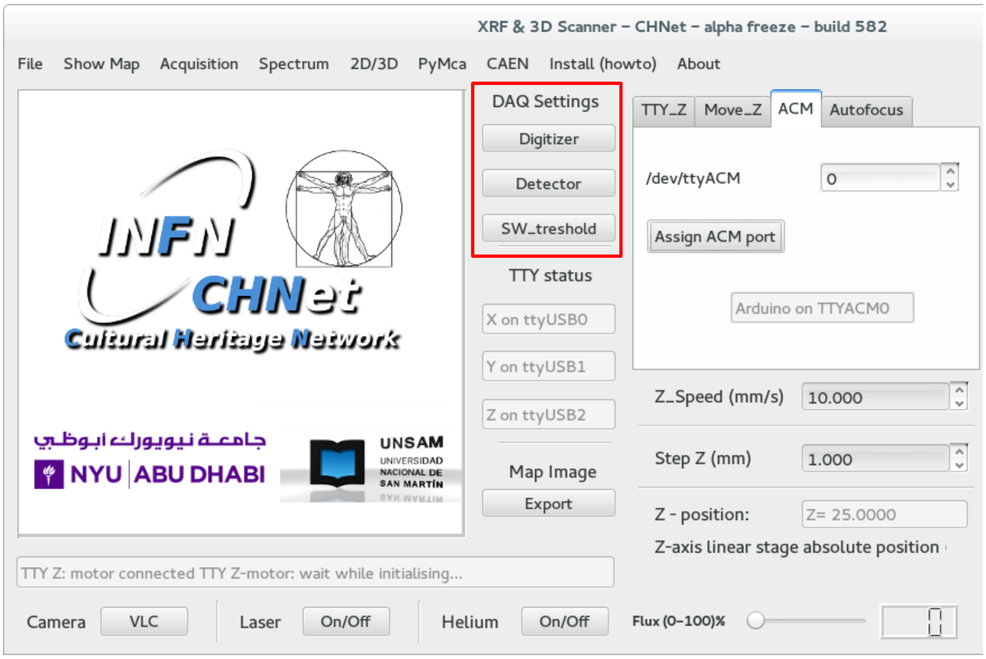

X on ttyUSB0

Y on ttyUSB1

Z on ttyUSB2

/dev/ttyACM 0

Arduino on TTYACM0

Z_Speed (mm/s) 10.000

Step Z (mm) 1.000

Z - position: Z= 25.0000

Z-axis linear stage absolute position

TTY Z: motor connected TTY Z-motor: wait while initialising...

Figure 3.11. View of the DAQ section of the GUI interface: "Digitizer", for setting the parameters for the detector signal manipulation; "Detector", to switch on/off the detector; "Threshold" allows setting an acquisition level threshold

3.3.1 *Energy resolution*

As explained in the previous paragraph, XRF2 allows configuring the parameters connected with data treatment and acquisition. This has a direct influence on the detector energy resolution (ER), i.e. the ability of the detector to distinguish X-ray lines with close energy values and to discriminate and possibly identify different elements in the spectra (Fig. 3.12). The resolution of energy-dispersive detectors is conventionally expressed as the FWHM of the Mn Kα (5.89 keV) [34].

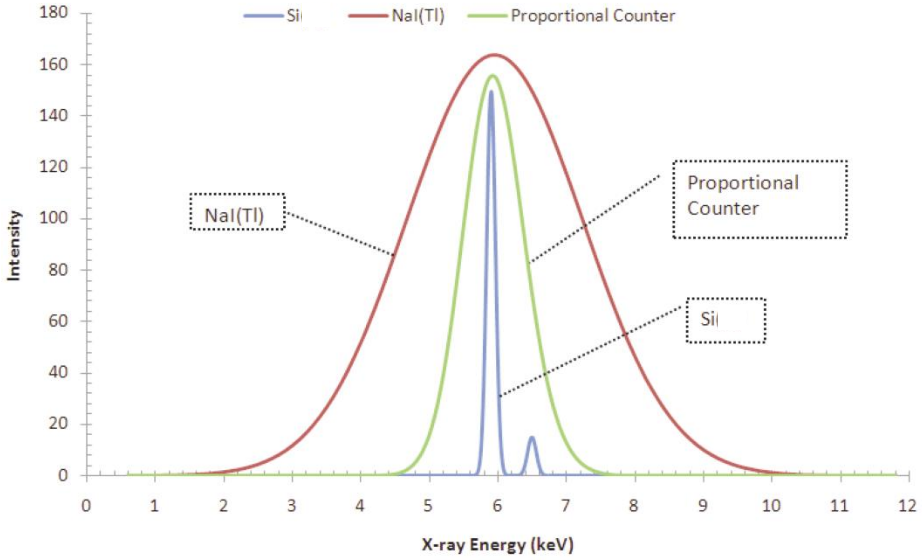

Figure 3.12. An example of the effects of different energy resolution values for the detection of the same X rays. In the plot, three cases are reported for the detection of the 5.89 keV X rays from an ^{55}Fe source: a NaI(Tl) detector (3.0 keV), a proportional counter (1.0 keV) and a Silicon detector (150 eV)

In particular, the width of detector signals is affected by electronic noise due to the pre-amplification/amplification system as well as by fluctuation in the number of carriers produced in matter[7]. Operating with the digitizer parameters it is possible to limit the noise contribution and improve the ER. I have tested diverse parameter configurations in order to obtain the best possible ER for the used detector.

ER was measured to evaluate the possible energy resolution worsening due to our system (noise contributions due to HV detector power supply, scanning motor power supplies, motor controllers, etc.). Measurements were carried out:

1) in single spot mode, with the original Amptek power supply, data acquisition hardware and software. No other electronic device was present or in use during this measurement, which is to be considered as the reference configuration, producing the best possible ER;
2) in single-spot mode, with the digitizer powering the detector and collecting the data, still without any other device connected or active. This has allowed evaluating possible ER worsening due just to the acquisitions system of the spectrometer, without any contribution due to motors and related devices;
3) in scanning mode.

---

[7] Since this factor is intrinsically related to the physical processes concerning the detection of X-rays it cannot be changed

I did not find any ER worsening when passing from the Amptek original acquisition system (only available for point mode acquisition) to the XRF2 acquisition, both in point and in scanning mode, with ER=147 eV in all the above-mentioned configurations.

Usually, in CH field, objects under study are intrinsically heterogeneous and thus composed by many elements. It may happen that the characteristic lines of elements important for the analyses partly or totally overlap. This makes the material compositional identification challenging for the XRF technique. In such a case, it is of great importance to have an ER as good as possible. However, any option allowing to overcome, at least partly, the problem of overlapping lines can be of great importance for the analyses.

Actually, in most commercial systems, imaging software only allows selecting an element and displaying the elemental map of the chosen element. Of course, this approach works nicely in most of cases but cannot be applied when elemental lines largely overlap. Following my suggestions, the imaging software of the XRF2 system allows for choosing any desired energy interval and it is not anymore mandatory to choose a pre-determined energy interval for creating the maps.

This option proved to be crucial in materials study whose elemental lines largely overlap, as shown in the following results, obtained from the analyses of the modern painting, "*Misure e curvature*" by Bice Lazzari (1967) (Fig. 3.13). This was possible thanks to the collaboration with the *Opificio delle Pietre Dure* (OPD) in Florence and the Peggy Guggenheim Museum in Venice.

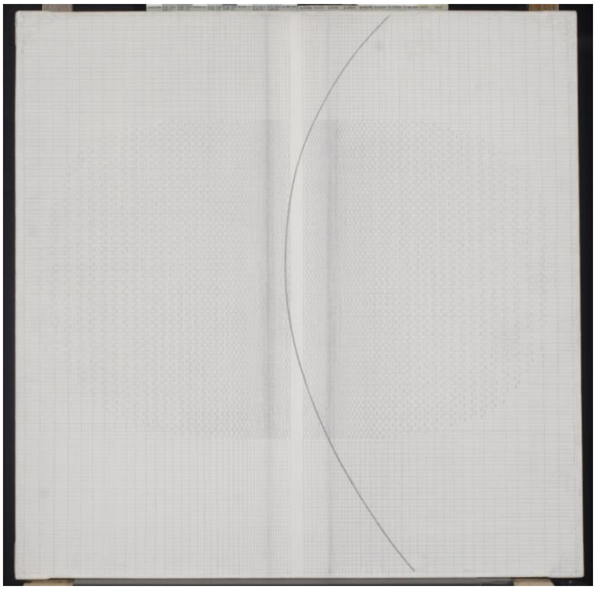

Figure 3.13. Picture of *"Misure e curvature"* painted by *Bice Lazzari*

This canvas is totally painted with white barium-based tempera and restored by using a titanium-white pigment[8]. The characteristic elements of these pigments show a large overlap of the X-ray lines: Ba L lines (Lα - 4,46 keV; Lβ - 4.92 keV) and Ti K lines (Kα - 4,51 keV; Kβ - 4,93 keV). To overcome this problem, the elemental maps have been obtained by selecting energy regions on the left part (red rectangle Fig. 3.14) and on the right part (blue rectangle Fig. 3.14) of the "Ba + Ti" peak in the spectrum.

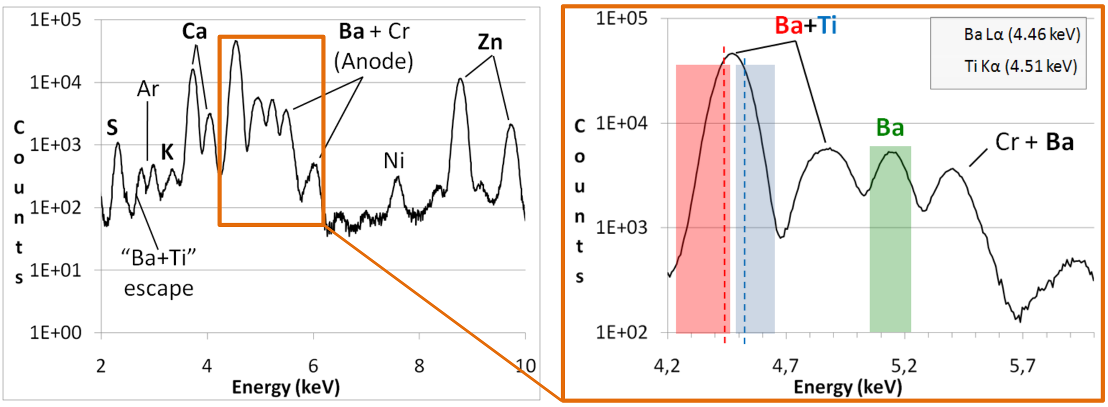

Figure 3.14. A portion of the spectrum relative to a whole map (on the left), a detail where the ROI's selection, to obtain the elemental maps, are highlighted (on the right)

For comparison, in addition to the maps obtained as explained above, also the Ba-L$\beta_{2,15}$ map (5.15 keV - green rectangle Fig. 3.14), a line characteristic uniquely of Ba, is reported. Results obtained in one of the sixteen areas of the painting studied during the diagnostic campaign are reported in the picture below (other results will be presented in paragraph 4.1.3). These results would not have been obtained with the standard approach, were the energy interval for every element is predetermined.

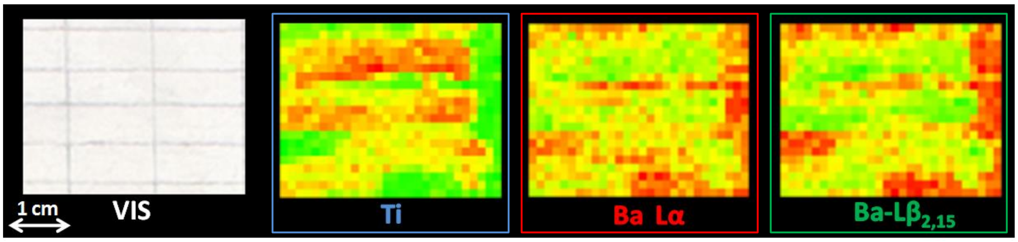

Figure 3.15. Picture and corresponding Ti Kα , Ba Lα, Ba L$\beta_{2,15}$ distribution elemental maps of the restored areas

---

[8] More pieces of information on the artworks and all the results concerning the painting palette and the restoration material can be found in paragraph 4.1.3

The corresponding spatial distributions allowed distinguishing the two elements, identifying clearly the position and dimension of the areas corresponding to the *lacunae* (restored with Ti-white) and of the surrounding original Ba-based pigment.

These tests confirmed that the good energy resolution and the above mentioned option of the XRF2 imaging software are really useful to overcome the problem of the Ba and Ti X-ray overlap.

3.3.2 Light element detection

Basing on the experience gained so far at the Labec laboratory on the XRF and IBA techniques [35], the XRF2 prototype was equipped with a continuous helium flow. It is well known that the use of helium flow during the measurement extend the range of detectable elements towards the low atomic numbers, minimising the absorption in air of the secondary radiation, emitted by the sample, with energies down to about 1 keV.

As shown in figure 3.16, helium is conveyed from a gas bottle to a plastic nozzle (red square) installed on the top of the detector, in front of the entrance window. In this way, helium fills the volume of the plastic nozzle in front of the detector entrance window and then flows outwards, creating an atmosphere with a reduced air content both along the secondary and primary X-ray paths. In this way, low energy X-ray absorption is strongly reduced and this allows for detecting X-ray even down to sodium (~ 1 keV), which is normally impossible with commercial instruments. Helium is injected from the detector, as the attention is mainly focused on the secondary X-ray transmission; of course in the so-produced atmosphere, air content is reduced but not suppressed and its presence is attested by the Ar peak.

The helium flow is directly controlled by the new GUI interface, where it is possible to switch on/off the flow and to set the desired flow rate simply by sliding the cursor in the scrollbar (see in Fig. 3.16, green square). The helium flow can be set to any value ranging from 0 up to 40 l/min, corresponding respectively to 0 and 100% in the GUI scrollbar. Usually for CH application a flow of 2 l/min (~5 %) is enough.

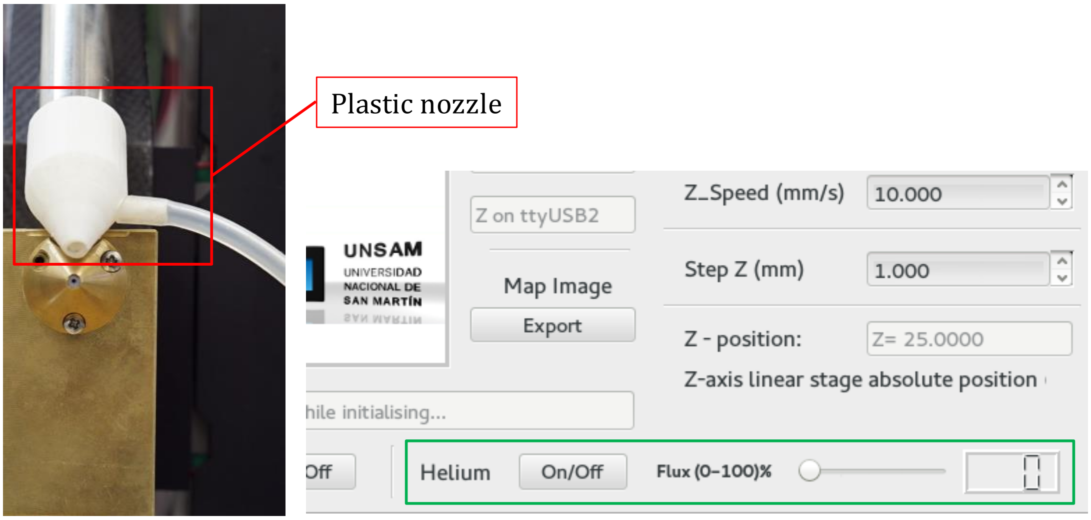

Z_Speed (mm/s) 10.000

Step Z (mm) 1.000

Z - position: Z= 25.0000

Z-axis linear stage absolute position

Figure 3.16. Detail of the plastic nozzle to convoy the helium flow in front of the exit window of the detector, on the left; detail of the GUI interface to control the helium flow directly through our software, on the right

For CH diagnostic, the identification of low-Z elements is of fundamental importance to get a more detailed material characterisation and is of special interest in the study of supports, pigments, restoration materials and alteration/degradation products.

To stress the importance of this feature, whose implementation and test I personally took care of, in this paragraph a particular application of the XRF2 is reported. During my PhD training I had the opportunity to analyse a Romanic mosaic (Fig. 3.17). The focus of this work was to locate glass *tesserae* composing the mosaic and to identify their composition.

As is well known, ancient glasses were generally obtained by a mixture of naturally occurring materials (beach sand and a crude source of alkali) containing silica, alkali and lime [36]. This practice continued all across the Mediterranean region through late antiquity. Besides the oxides of Si, Al and K, which define the basic composition of the glass recipe, further components are added as colorants or as an additional flux material [37]. As these glasses are mainly characterized by light elements, the glass *tesserae* are perfect samples to test the true effectiveness of the XRF2 equipped with the helium flow. The analyses focused in particular on the brownish and greenish *tesserae* (highlighted in Fig. 3.17 with the yellow squares), following the indications given by the restorers.

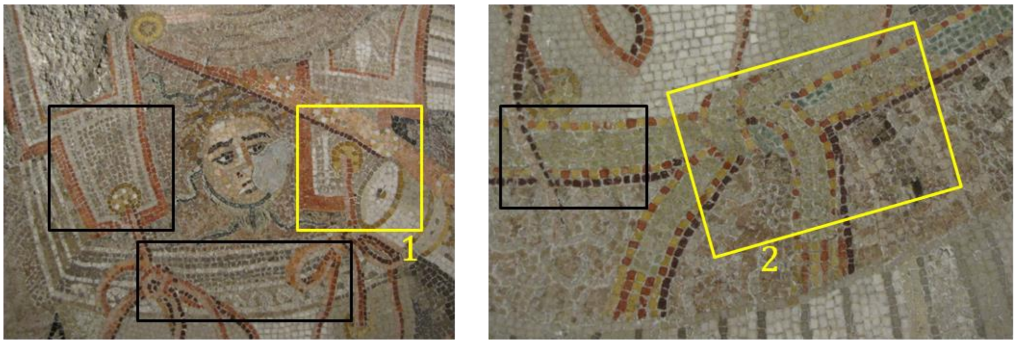

Figure 3.17. Image of two different areas of interest for the diagnostic campaign, which represent some dressing decorations. The analyses focused in particular on areas with brownish and greenish *tesserae* (the studied areas are highlighted in the pictures with the yellow squares)

Below, only two examples are shown, concerning the results for the brownish-glass and the greenish-glass *tesserae*. In the Fig. 3.18 the Si and Ca elemental maps are reported, in order to discriminate glass and stone tesserae. To have a complete characterization of the glass *tesserae* also an example of “sum spectrum”[9], referred to the scan acquisition on AREA1, is reported. The spectrum shown in Fig. 3.18 is comparable with all the others obtained from the scanned areas on glass.

---

[9] The “sum spectrum” is the spectrum referred to the whole scanned area, obtained by the sum of the spectrum of each pixel

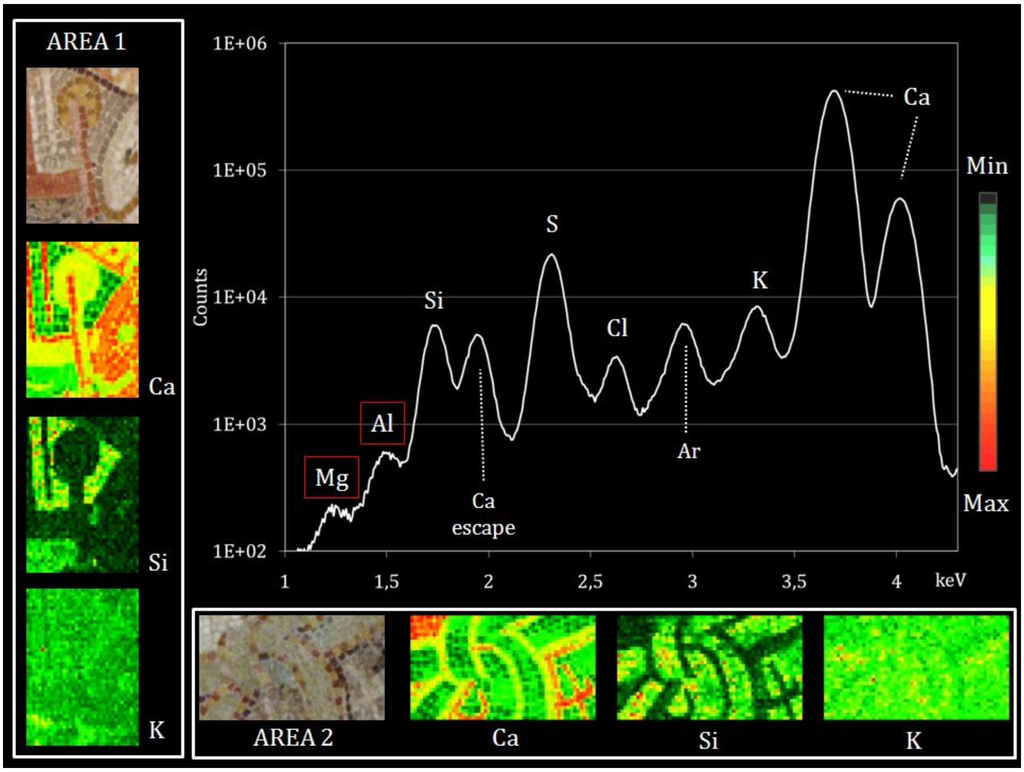

Figure 3.18. The main components of the glass *tesserae* are shown both in the "sum spectrum" (similar for all the analysed areas) and in the elemental maps, for two different areas. The S and Cl peaks in the spectrum are probably due to the alteration products (such as gypsum or soluble salts) formed by the degradation of the mortar. The Ar peak is due to excitation of air between the measuring head and the sample along the X-ray path

Exploiting the Si map, it is easy to locate the glass *tesserae* composing the mosaic. In the AREA 1, the Si distribution is clearly linked to the brownish *tesserae* inside the triangle-shaped decoration (upper part of the area) and to the integration of the *lacuna*[10] (lower part of the map). A similar Si distribution is visible into the AREA 2 for the greenish *tesserae* inside the knot belt and for the brownish *tesserae* in the lower part of the map, corresponding to the dress. In all the analysed areas, Si and K maps (the former having statistics by far higher than the latter) show similar spatial distributions, suggesting the presence of traces of the K in the glass composition.

In both areas, the Ca distribution suggests two separate sources for this element: the white *tesserae*, made of calcareous stone material, and the mortar, composed mainly by calcium carbonate. The mortar can be identified in the Ca maps as the lines surrounding the glass

---

[10] The signal of Si into the *lacuna* is probably due to the presence of the sand, added as a filler for mortar production

tesserae. Summarising, it can be noted that the Ca distribution due to the mortar and the Si distribution due to the glass are complementary.

In addition to the presence of the above mentioned elements, the "sum spectrum" also shows the presence of Al and Mg. For these two elements, the peak-to-background ratio is too low to obtain significant spatial distributions, which appear to be similar to the background one. Therefore, it is not possible to uniquely link Mg and Al to glass. Nevertheless, considering literature, some hypotheses can be done. For example, the presence of Si, Al, K, Mg could suggest the basic composition of silicate-alkaline-lime glasses. In particular the low amount of Mg, Al and K would denote a glass classified as 'low magnesium–low potassium' (LMLK) glass [38]. However, the combined presence of K and Mg could suggest another hypothesis: the addition of a plant ash-based flux to the matrix during the glass production. Indeed, silicate-alkaline-lime glasses can be produced combining a plant ash with quartz sand[11] [39].

The XRF imaging results put into evidence also the presence of further components in the glass composition, probably added as colorants [40]. Indeed, the two different colours of the analysed glass tesserae, the brownish and greenish ones, are characterised by different elements in addition to those of the glass matrix (Fig. 3.19).

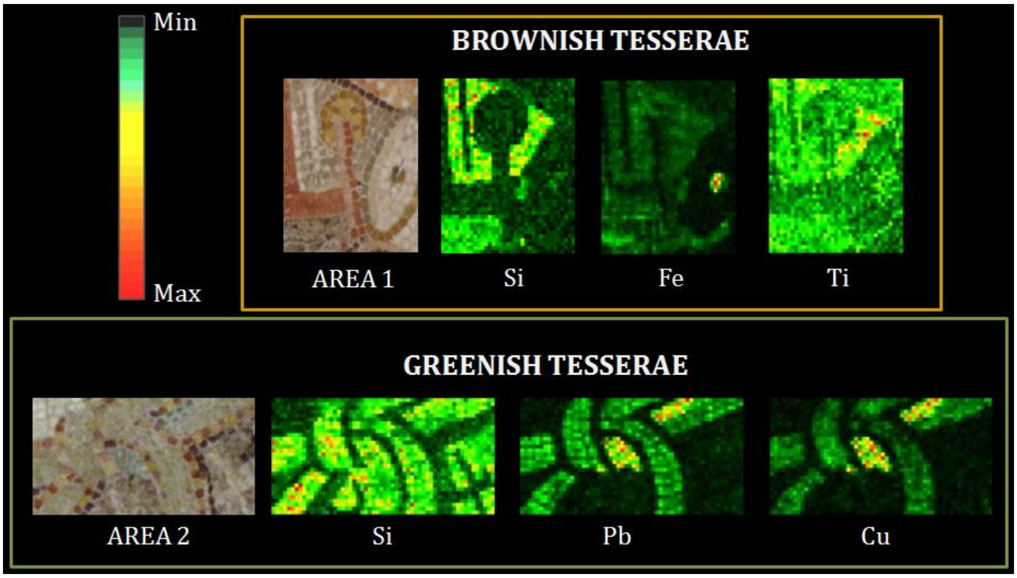

Figure 3. 19. XRF distributional maps of the elements characteristic of the further components added to the glass matrix for colouring the *tesserae*

---

[11] Silicate-alkaline-lime glasses can be divided into two categories: plant ash glass, combining a plant ash with quartz sand; and natron glass, combining soda rich mineral with quartz sand. Before the middle of the first millennium BC, plant ash glass was produced from its raw materials in Egypt and Mesopotamia. Thereafter, natron glass became the predominant type of ancient glass in the whole Mediterranean area and in Europe, this until the ninth century AD (Freestone et al., 2002a; Shortland, 2004)

The brownish *tesserae* of the AREA 1 are characterised also by the signal of Fe and Ti. As well known, Fe, responsible for the brown colour, is usually added to the matrix of glass as oxides, in its trivalent states [41]. In this case, the correlation between the distribution of Fe and Ti suggests a non-intentional introduction of iron, instead of the use of raw material containing both these two element [42].

Instead, the greenish *tesserae* are characterised by the presence of both Pb and Cu. This can suggest the use of lead-glass, in which Pb is added to increase the brilliance, coloured with a green Cu-based chromophore. Otherwise a mixture of a blue Cu-based chromophore and lead can be supposed, as it is well known that Cu- chromophore in presence of PbO can turn to green [40].

3.4 Acquisition and data analyses extended toolkit

In this section several minor, but nonetheless important implementations are presented. In addition to the major upgrades, in the software and in GUI interface some functions were added, in order to simplify the use of the scanner or to make easier data analysis.

As the “on line” visualization of the map during the measurement is not yet available, on the basis of my “on field experience”, a rate meter (Fig. 3.20), displaying the real-time X-ray detection count rate, was added.

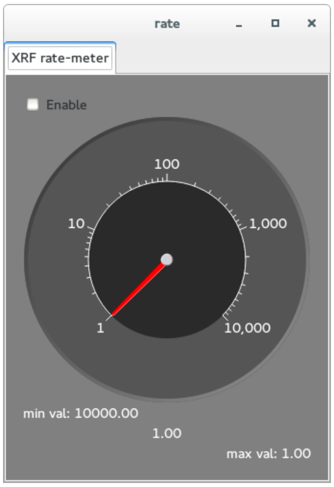

☐ Enable

min val: 10000.00

1.00

max val: 1.00

Figure 3.20. GUI interface for the rate meter (counts per second)

This instrument provides real time indications about the statistics which can be acquired in the current measurement, in order to decide *a priori* whether it can be sufficient for the analyses or not, thus avoiding wasting of working time.

Another function was introduced in the GUI, which works on the number of channel of the spectra. CAEN digitizers, both in XRF1 and XRF2, acquire 16384 channel spectra. Typically, we do not need such a high number of channels, as the energy range of our XRF spectra is most often within 10-20 keV and only seldom extends up to 30 keV. Such a high number of channels decreases the statistical content of each channel without any significant improvement in detector energy resolution[12]. So, if counts in the 16k are not enough for reliable data analysis, we can now re-elaborate the spectrum, grouping the channel by a factor 2 (8192 channel spectra) or 4 (4096 channel spectra). This operation can be directly carried out by exploiting the functions “16k” (standard mode), “8k” (channels grouped by a factor 2) or “4k”(channels grouped by a factor 4) in the spectrum GUI (Fig. 3.21, top right).

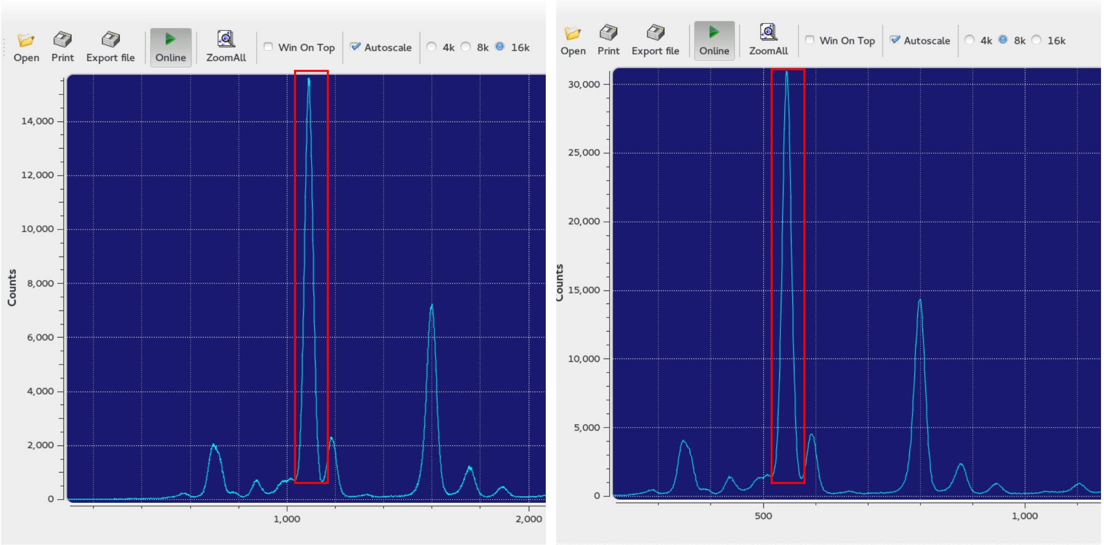

---

[12] With 16384 channel we have between 1 and 2 eV per channel, which means that a peak at the smallest possible width of 140 eV corresponds to 70-140 channels (16k), 35-70 (8k) and 18-35 (4k), well adequate for normal statistical treatment, such as peak fitting

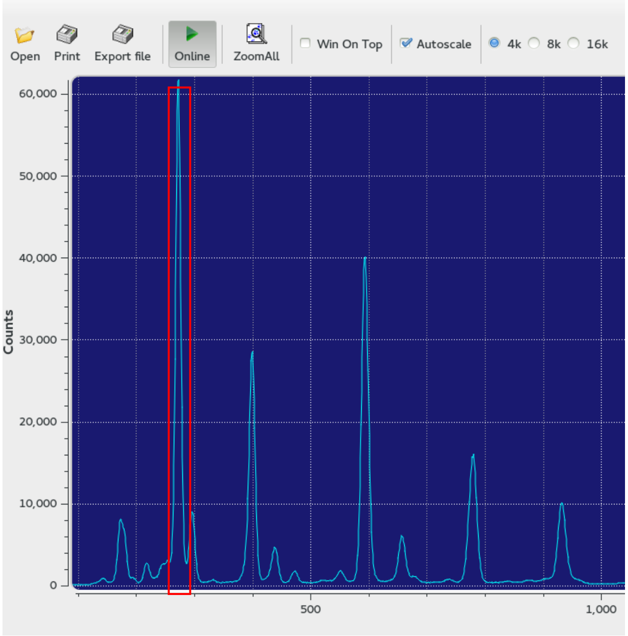

☐ Win On Top ☑ Autoscale ● 4k ○ 8k ○ 16k

Figure 3.21. One example of the same spectrum in the three different modes of re-elaboration: "16k"-the original acquisition-, "8k" and "4k"

An example of a 16384 channel spectrum transformed into 8192 and 4096 channel spectra is reported in Fig. 3.21. From the pictures it is easy to observe that both the centroid and the maximum number of counts of each peak change proportionally when grouped by a factor 2 or 4. For example, the peak highlighted with the red square in the first picture, corresponding to "16k" acquisition mode, has the centroid channel $C_{max,16k} \sim 1050$ and maximum number of counts $N_{max,16k} \sim 15000$. With the function "8k" (second picture), the re-elaborated spectrum has $C_{max,8k} \sim 525$ and $N_{max,8k} \sim 30000$, while with the "4k" function (third picture) has $C_{max,4k} \sim 263$ and $N_{max,4k} \sim 60000$.

As one of the main purpose of this PhD thesis is the *imaging* data analyses. A program to convert our files in a format useful for the PyMCA *imaging* toolkit was developed. *PyMCA* [43, 44] is a set of open-source software tools for XRF analysis that has become a standard for users of most beam-related laboratories and for many X-ray based investigations. This software, developed by the European Synchrotron Radiation Facility (ESRF), is suggested by the guidelines of the International Atomic Energy Agency for XRF data analyses of single spot measurements (qualitative and quantitative analyses) and elemental map elaborations.

Some of the functions used by PyMCA are already available also in our instrument, such as the visualization of the spectrum for a portion of the whole scanned area (Selected region) or for each pixel of the map. Some others have not yet been implemented, the most important of which is the fitting procedure for spectra data analyses. The PyMCA fitting procedure can work with multiple lines and background subtraction and makes possible quantitative analyses, in a fast and easy way. Just to give an example, the PyMCA fitting routine was used for extracting the areas of the peaks in the intercomparison of the analyses with and without the tracking system on the *"Madonna con bambino"* and on the illuminated parchment, discussed above in this chapter.

For the *imaging* analyses, *PyMCA* input has to be divided into different files, each of which is the spectrum of a progressively enumerated pixel of the map. For odd rows, the imaging algorithms adopted by *PyMCA* and by our software assume the same order of the spectra, while for even rows the two programs assume reversed orders. This problem was overcome with a dedicated C++ routine, developed to switch data from our to *PyMCA* format. In this way, this recently added routine is able to generate the correct ordering of the files and thus to produce a *PyMCA* compatible file format.
Our *file.txt*, obtained by the scanning acquisition mode, can be easily converted by simply clicking the "*PyMCA*" button in the new GUI interface. An example of the elemental maps as displayed both with our software and with PyMCA is reported in Fig. 3.22, where the maps acquired on the detail of the peacock's tail (Par. 2.4) are shown.

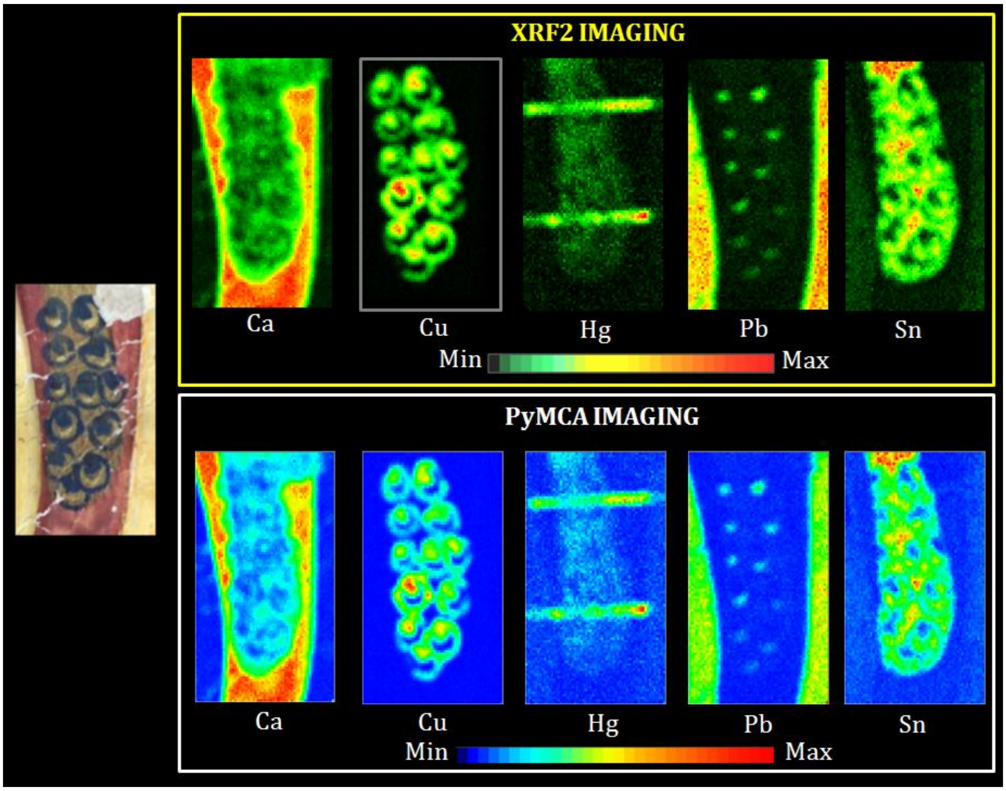

Figure 3.22. An example of the elemental maps as displayed both with our software and with *PyMCA*. In the picture, the maps acquired on the detail of the peacock's tail, already shown in paragraph 2.4, are reported

PyMCA ROI imaging and *RGB* tools allow for analysing the correlation between different elements in the same area, by assigning three different colour (red "R", green "G" and blue "B") to different elements. These three spectral bands are combined by the program to obtain a false colour map.
In Fig. 4.23 some example of false colour maps, which were obtained combining the same elements reported in the previous image, are shown.

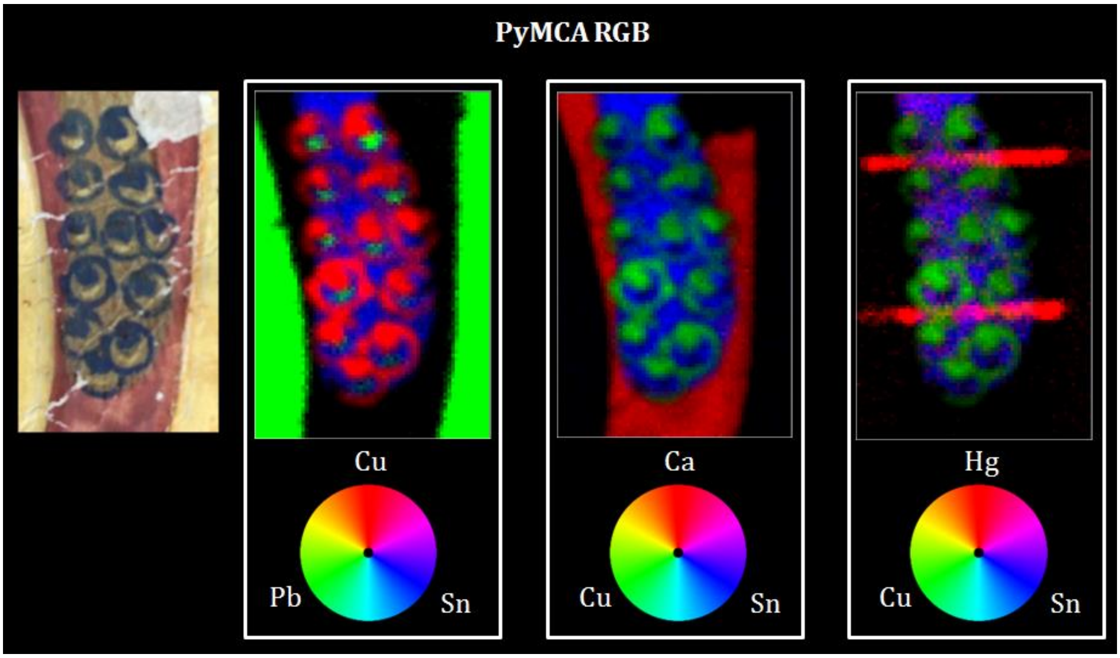

Figure 3. 23. Some examples of false colour maps, obtained combining the Cu, Sn, Pb, Ca and Sn energy ROIs are shown

Several elemental maps can be combined to form RGB composite images (Fig. 3.23), highlighting the presence of two or more chemical elements in the same area, thus facilitating the identification of pigments or composite materials. As said, the correlation between multiple elements present in the same area can be difficult to infer from a limited number of single-point spectra, but it becomes possible and often clear by using direct elemental imaging. However, there can be cases in which the element correlations can be difficult to point out; in these cases the RGB imaging tool can provide a precious help in identifying the unknown materials.

As an example we shortly note that in figure 3.23 the simultaneous presence of Hg and Sn in the same area, the former associated to the R and the latter to B bands respectively, produces intermediate pink colours in the peacock's tail. Thus, at a glance, the presence of this intermediate colours clearly indicates the use of a composed material where both elements are simultaneously present. This way of presenting the obtained results noticeably enhances the readability by the non-trained personnel, thus making results more usable. In this particular case, the simultaneous presence of Hg and Sn in the gilded tail suggests the use of artificial Purpurin (for a detailed discussion of the material used for the illuminated initial gilding restoration, see par. 4.3.2).

CHAPTER 4

XRF imaging for material investigation in Cultural Heritage field

As well known, for the study, conservation and restoration of valuable cultural/historical artefacts, analytical methods, able to provide information about the chemical composition of the materials, are required [45]. Indeed, the decision of a suitable conservation/restoration treatment is connected to the materials, the manufacturing process and the conservation state of the artwork and a deepened knowledge of the object under study allows for choosing the most appropriate products and procedures to be applied by restorers [46]. In addition, in some cases, material studies, performed before, during and after the conservation interventions can give information also about the efficacy of conservation and restoration strategies.

Considering the artistic and historical value of the object, analyses are preferably carried out respecting the physical integrity of the object under investigation, avoiding damages. For this reason, non-invasive analyses are considered the first and best approach for diagnostic campaigns [47, 48, 49]. In addition, portable instruments are required for *in situ* analyses, to carry out measurements on site (i.e. in the museum or in the archaeological site) without moving the artworks to the scientific laboratories.

Finally, as already explained in Chapter 2, most of the objects of artistic or historical interest have quite inhomogeneous structures, even within apparently uniform areas, thus they often represent problematic samples for “single spot” compositional analysis, since these features are not easily identified by visual examination [20].

Among non-destructive, non-invasive, portable, analytical techniques, suitable for imaging, XRF plays a noticeable role in Cultural Heritage.

Therefore, to highlight the great potential of the XRF imaging analyses, a lot of time of my PhD training was dedicated to reliably apply this approach to Cultural Heritage samples. To accomplish this task, I carried out a wide diagnostic campaign on a total of 30 artworks, among which paintings of the “Old Masters”, such as Simone Martini, Botticelli, Leonardo, Raffaello, Carracci, and of modern painters, such as Manet, Previati, Lazzari, Leger, Buffet and Picasso (proposed attribution).This was possible thanks to the collaboration with the *Opificio delle Pietre Dure* (OPD) of Florence, one of the world's most renowned centres for artistic restoration, with other groups of conservation scientists and privates interested in CH diagnostic.

In the wide majority of these applications, the instrument allowed me to easily find the answers to restorers' questions, as for the identification of the painting palette, as well as the discovery of "*pentimento*"[1], restorations or alterations occurred over time. In addition, it was possible to have information about the technique used to create artworks and details, such as in the case of gilding technique. Quite unexpectedly, in many cases the XRF compositional imaging approach allowed me to also get indications about the artworks stratigraphy. Notwithstanding the XRF scanner is now a truly user-friendly instrument.

For my PhD thesis, a huge amount of data has been collected in the many diagnostic campaigns, during which the acquisition time (detailed for all the reported case studies) is only a small fraction of the total time required to achieve sufficient information (through measurements and data analysis) to solve when possible the issues raised by the restorers and art historians.

In this chapter only the most significant results will be presented, in order to highlight the capability and versatility of the XRF mapping analyses. I remind here that colours in the map are attributed taking into account the maximum and the minimum number of counts for each selected ROI. As a consequence, for elemental maps obtained from different ROIs, the same colour may correspond to different counts and different colours may correspond to the same number of counts.

4.1 Material investigation

The three case studies reported in this paragraph show examples of results achievable with XRF imaging: indications about the deeper layers (preparation layer and imprimatura), characterisation of the panting palette and discovery of "hidden" features, such as *pentimenti*.

The case studies reported here concern the identification of pigments used during different periods: Renaissance, Baroque and "Modern" period. The examples are chosen in order to give an idea of the evolution of the pigments used over the time.

---

[1] *Pentimento* is an underlying painting in the artwork, evidence of revision by the artist

4.1.1. Renaissance period: "La Muta" by Raffaello

The first example concernsan early work of Raffaello's maturity: *The Portrait of a Young Woman*" (Fig.4.1), also known as "*La Muta*", an oil panel (64 x 68 cm^2), painted in between 1507-1508.The examples reported below are a part of the results of the study published on Microchemical Journal[2], during the second year of my PhD.

Figure 4.1."*Portrait of a young woman*", painted by Raffaello

The XRF analysis was conducted over twenty-one areas, selected in agreement with the restorers, in order to obtain deepened information about *pentimenti* and the painting palette. The analysed areas (in total 240 cm^2) were acquired in 6 hours and 42 minutes. For all the measurements, we always used 35 kV anode voltage, 100 µA anode current, 1x 1 mm^2 pixel size and 1mm/s scanning speed.

For the following two examples (fig. 4.2 and 4.3), the Ca and Pb (low and high energy) maps are reported to point out the information on the deeper layers of the painting.
As seen in the figures hereafter, there are variations in the Ca distribution in both areas. Ca shows higher absorptions in correspondence of high-Z elements. Indeed, heavy elements absorb Ca X-rays, producing a sort of "negative image" of the area. This behaviour suggests the existence of a underlying preparation layer, most probably composed of gypsum ($CaSO_4$),

---

[2] Ruberto C. et Al., Imaging study of Raffaello's "La Muta" by a portable XRF spectrometer, Microchem. J. (2015); Vol. 126, pp.63-69 (DOI: 10.1016/j.microc.2015.11.037)

applied to produce a hard smooth surface for panel paintings[3], standardly used at Raffaello's time [50; 51; 52].

Let's now consider the Pb maps of high (Lα line - 10.55 keV) and low (Mα line - 2.3 keV) energy: the formers are by far more homogeneous and intense than the latters (Fig. 4.2 - 4.3). This difference can be explained considering that the low-energy Pb M X-rays are absorbed practically by any overlying pigment (especially in cases of thick and/or high-Z applications). This means that, if the Pb M X-rays are detected, they originate from a shallow layer, while if only the Pb L lines are detected, the Pb contribution must arise from a buried layer. Therefore the intercomparison between L- and M-line maps indicates that lead white pigment (($2PbCO_3{\cdot}Pb(OH)_2$) [53; 54] was applied at two different depths, in both a deep layer (imprimatura[4]) [55; 56] and in a shallower pictorial layer.

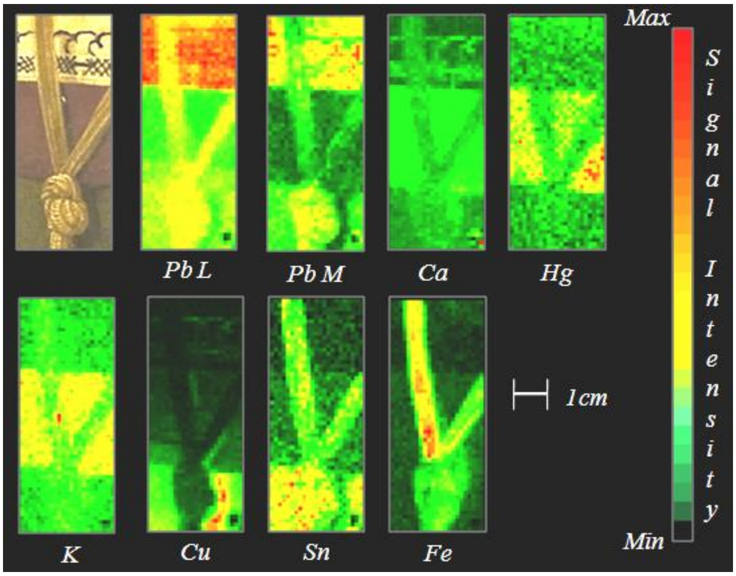

Figure 4. 2. XRF elemental maps of the bodice detail, in correspondence with the necklace, are presented. The elemental maps include Pb (high energy L and low energy M), Ca, Hg, Cu, K, Sn and Fe

Into the necklace (Fig. 4.2), the overlapping distributions of Sn, Pb, Fe and K can be noticed. The simultaneous presence of Sn and Pb suggests the use of tin-lead yellow pigment (Pb_xSnO_x), formally known as "*giallorino*" [57; 58]. Additionally, coherent distributions of Fe and K usually occur in presence of ochres, where K can be found as a trace element (for

---

[3] Actually this type of preparation layer was commonly used also for different supports (as canvas) and in other periods

[4] Imprimatura come into standard use during the Renaissance, particularly in Italy. It indicated a colour layer used to create a ground for a painting according to the classical technique. The imprimatura over a toned gesso or a toned primer reflects the light through the overlaying painting layers, almost creating a 3-D effect

more details, see par. 4.1.2). Ochres were widely used during the Renaissance. So I can assume that Raffaello probably mixed *giallorino* and ochre to obtain his unique “gold” color.

Furthermore, the Cu map in figure 4.2 shows a clear correlation with the green region, thus suggesting a copper-based pigment[5], such as *Verdigris* ($Cu(CH_3COO)_2$) or *Malachite* ($Cu_2(CO_3)(OH)_2$) [59; 60; 61], that could have been used by Raffaello. In the same area we also observe the simultaneous presence of Sn and Pb, suggesting that Raffaello painted this section using a mixture of *giallorino* and a copper-based pigment, to obtain a warm green.

In Fig. 4.3, the elemental maps of Pb (low energy), Ca and Hg, reveal the presence of two bows, highlighting at a glance the presence of “hidden” features of the painting (*pentimenti*), which represent the evidence of a revision by the artist. Many other underlying paintings were discovered, such as in the shoulder of the lady’s dress or in the hands; all of them were characterized by XRF scanning analyses, although not reported here for brevity.

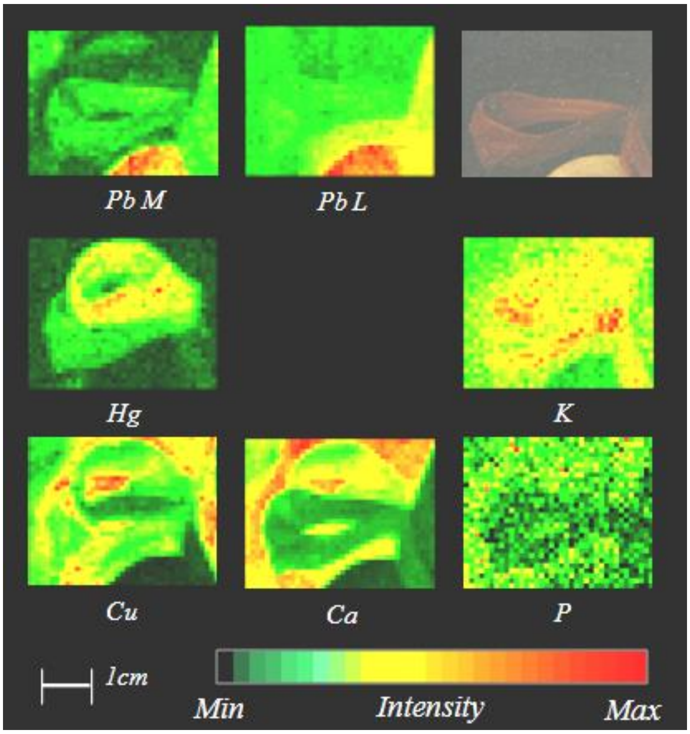

Figure 4.3. XRF elemental maps of the area surrounding the bows: the results for Pb (high energy/L-line and low energy/M-line), Ca, Hg, K and Cu are shown. The figure shows one example of *pentimenti*, where the elemental maps of Pb (low energy), Ca and Hg reveal the presence of two bows — one visible and one hidden

---

[5] XRF analysis, being an elemental technique, is not able to discriminate among the variety of copper based pigments, as the only characteristic element typically detectable is Cu

Both bows are characterized by the distribution of Hg, which shows a noticeable increase where the two bows overlap, suggesting Raffaello's use of cinnabar (HgS)[6] for painting red regions. This is also confirmed by the results to the red part of the bodice, mainly characterised by the Hg distribution can be noticed (Fig. 4.2).

In the red areas, also the presence of K is noticeable (Fig. 4.2 – 4.3). This element, as previously mentioned, can suggest the use of ochres, but, in this case, the K signal is higher than the Fe[7] one, which is almost negligible, thus suggesting that Raffaello did not use ochres to paint red areas, but probably a potassium-containing compound, mixed with cinnabar. The potassium-containing compound could be the "*Allume di rocca*" ($KAl(SO_4)_2 \cdot 12(H_2O)$)[8] [62], commonly used as a mordant for organic red lakes (semi-transparent color) [63; 64] at Raffaello's lifetime.

In addition, the comparison between the Hg and Pb maps (Fig. 4.3) highlights compositional differences among the two bows. The "hidden" ribbon shows higher intensity of Hg than the "visible" one, which is instead characterized by higher Pb content. The addition of lead white could be motivated by the need of increasing the opaqueness of the semi-transparent red color, as the "visible" bow was painted directly upon the black background (as we can see from the Cu map in Fig. 4.3 and as explained hereafter).

The black background is denoted by high counts of Cu, Ca and Pb (Fig. 4.3). The last two elements are due to the contribution of the preparation layer (gypsum) and imprimatura (lead white) respectively, as previously mentioned. Then, the Cu signal can be reasonably assumed as characteristic of the black background. This result is confirmed by the Cu distribution in the black lace embroidery (Fig. 4.2).

Also the Ca distribution, in the lace embroidery (Fig. 4.2), and the P distribution, in the background (Fig. 4.3), can give information for the characterization of the black colour. In the first case, the lacing is located on the painting's topmost surface, where Ca X-rays from the deeper preparation layer are absorbed by intermediate layers and especially by the lead white application in skin and lace. Therefore, the growth of the Ca signal in the lace suggests the presence of this element in the topmost black pigment, in association with Cu.

P spatial distribution in the black background, with the exception of the interior of the "visible" bow, also suggests the presence of P in the topmost black layer, as the low energy (2 keV) P X-rays are easily absorbed by any interposed layer. In addition, P lines in the spectra

---

[6] S K lines largely overlap Hg M- and Pb M- lines, so it is not possible to obtain a map which is really connected with only S

[7] An ochre-based spectrum would be characterized by an intense Fe peak with only a small signal of K peak

[8] Unfortunately, we can only infer the existence of potash alum by the spectrum's K peak, as characteristic Al emissions are of too low an energy to be detected by in-air XRF analysis (it was not possible to use He, as at time the helium flow equipment was not yet implemented)

acquired on the lace embroidery are statistically significant and this confirms the presence of this marker, although in too low quantity for reconstructing its spatial distribution. The co-presence of Ca and P suggests the use of black bone[9]. Therefore Raffaello probably created this black shade by mixing a copper-based pigment with a black pigment[10], possibly bone black.

The other scanned areas further confirmed the Raffaello’s use of cinnabar, *giallorino*, ochre, bone black, red lake, copper and lead white pigments. This information is summarised in Table 4.1.

Colour	Characteristic elements	Pigments
Green	Cu, Sn, Pb	Green-copper based pigments (*Malachite*, *Verdigris*, etc.) and tin-lead yellow
“Gold”	Pb, Sn, Fe	Lead white, tin-lead yellow and ochres
“*Incarnato*”	Pb, Hg	Lead white and cinnabar
Red	Hg, K	Cinnabar and red lake
White	Pb	Lead white
Darker areas (shadow)	Fe, K, Ti	Addition of ochres
Brighter areas	Pb	Addition of lead white

Table 4.1. Pigments used in “Portrait of a young woman” and their detected characteristic elements

Further examples of the results obtained in this study of “*La Muta”* can be found in the published paper.

4.1.2. Baroque period: “Cristo in Gloria e Santi” by Annibale Carracci

In this paragraph, the case study of the “*Cristo in Gloria e Santi*” (Fig. 4.4), an oil *tempera* on canvas, painted by *Annibale Carracci* around 1600, is presented.

---

[9] This pigment is obtained by charring animal bones and consists of 15-20% carbon and 60-70% calcium phosphate. Usually, with single-point XRF analysis, its determination would be hard, if possible, because Ca signals originate from the pigment are indistinguishable in the spectrum from the one due to the gypsum preparation layer (CaSO4)

[10] Generally, XRF analysis is unable to discriminate among a multitude of black pigments, most of which are organic compounds

XRF analysis was conducted over twenty-three areas, selected in order to characterise the painting palette. The analysed areas (in total 320 cm^2) were acquired in about 9 hours and 15 min. For all the measurements, the standard conditions were 30kV anode voltage, 100 µA anode current, 1 x 1 mm^2 pixel size, and 1mm/s scanning speed.

Some examples of the measurements carried out on this painting are shown, focusing the attention on the characterization of ochre pigments.

Figure 4. 4. "*Cristo in gloria e Santi*", painted by Carracci

In any historical period and also in the baroque time natural earths were extensively used as pigments, due to their high availability, high colouring capacity and stability under a variety of weather conditions.

Among natural earths, different types of pigment can be found: ochres, red earths, Sienna and Umbers. They can be classified according to colour, provenance and composition. All natural earth pigments contain iron compounds as main component[11]. They can be therefore distinguished by the diverse amounts of the minor components in accessory minerals (such as Ti, Ca, K, Mn, Mg), which influence the colours of the ochres.

Differences in the composition of the earth pigments constitute the main aim of this paragraph. In the following, some results on yellow, brown and green earths are presented.

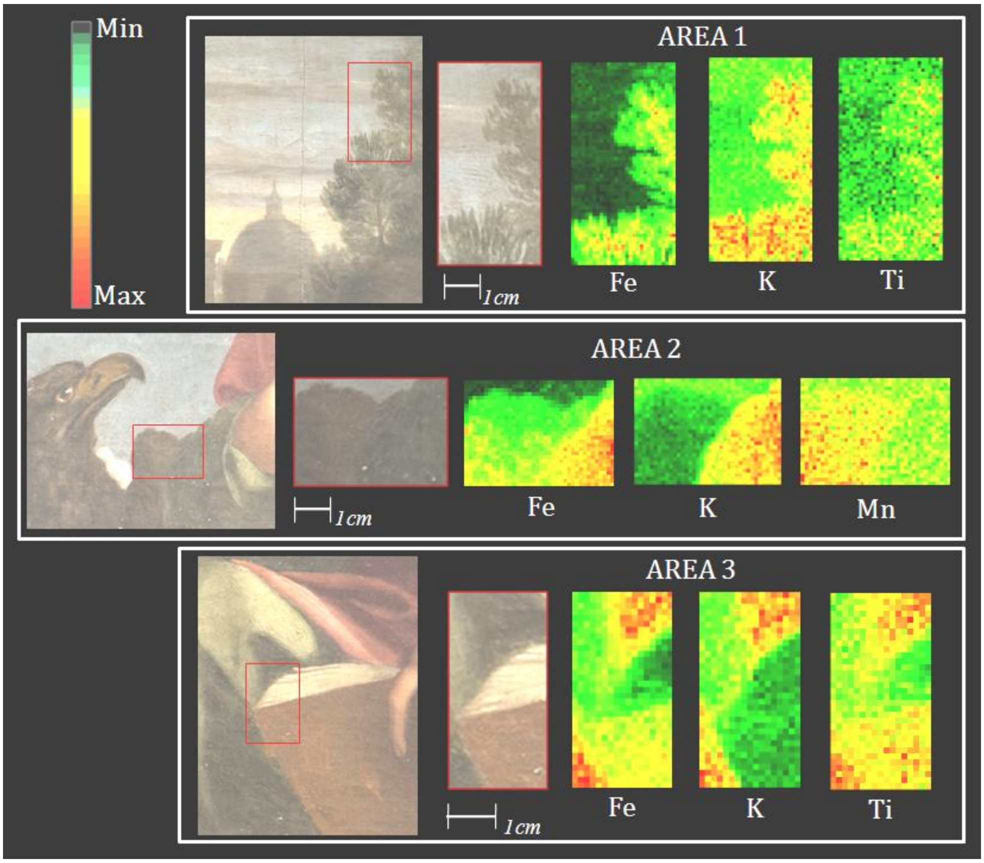

Figure 4.5. XRF elemental maps detailing the distribution of characteristic elements (Fe, K, Ti, Mn) in three different earths: green, brown and yellow

As we can see in figure 4.5, all the analysed areas show the presence of Fe as the major element, thus clearly indicating the use of natural earths. The main discrimination can be made observing the distribution of minor components (Ti, K and Mn).

---

[11] The XRF technique is not able to distinguish among different iron compounds, such as oxides, hydroxides or carbonates, as the unique detectable element is Fe

- Green pigment:

This pigment, used to paint the trees (AREA1) and the dress (AREA2 - 3), is characterised by the simultaneous presence of high counts of K and low counts of Ti, in addition to Fe. The high content of K suggests the use of a green earth, whose hue is generally ascribable to the presence of a mixture of hydrated aluminosilicate minerals of magnesium, iron and potassium, such as glauconite or celadonite [65, 66].

- Brown pigment:

In AREA2, in correspondence of the brown pigment used to paint the eagle, the Mn and Fe spatial distributions are in good agreement, suggesting the presence of a “burnt” Sienna pigments or a “burnt” Umbers. Both these pigments are characterized by the presence of manganese dioxide (MnO_2) impurities. The formers are yellow-brownish pigments, made of silica and clay containing a mixture of hydrated ferric oxides [67]; the latter are instead dark pigments composed by silica and a mixture of iron oxides, typically used for painting shadows or for shading colours. Considering the chemical composition of these two natural earths, no discrimination between them is achievable by XRF technique.

- Yellow pigment:

The yellow pigment used to paint the book (AREA3) is characterized by the co-presence of Fe, Ti and K, as the green pigment above described, but with different proportions. Indeed, the yellow pigment presents a remarkable decrease of the K intensity and an evident lowering of the Fe intensity, while for Ti, only a moderate decrease seems to be present. These different behaviours are clearly visible in the maps acquired on the AREA3 and shown in Fig. 4.5, where the yellow pigment of the book is compared directly with the green of the dress. The corresponding elemental ratios, calculated from the peak areas of the spectra acquired on areas corresponding to both pigments, are: K/Ti=3, Fe/K=7 for the yellow pigment and K/Ti=10, Fe/K=2 for the green pigment. The noticeable variation of the Fe/Ti and K/Ti ratios, when passing from green to the yellow pigment, confirms the conclusions drawn by directly comparing the elemental maps of AREA3 and suggests the use of a generic ochre for the yellow pigment.

Generally speaking, ochres are natural earth pigments varying from dull yellow to red. The colour of the pigment depends on the nature of the chromophore: the darker red ochres are richer in iron oxide (i.e. haematite), while the paler yellow ochres mainly contain hydrated iron oxide (such as goethite) [68]. Another factor that can also influence the yellow colours of the ochres, as already said, is the presence of other minerals, in this case probably composed by K-minerals, or other metal oxides, explaining the presence of Ti.

For a complete characterisation of the painting palette, in table 4.2 the results obtained from all the scanned areas are summarised.

Colour	Characteristic Elements	Pigments
Green	Fe, K, Ti	Green hearts
Brown	Fe, K, Mn	Sienna pigment or umbers
Yellow	Fe, K, Ti	Yellow ochre
Blu	Cu	Copper based pigments (Azurite)
	None	Hypothesis of Indigo o Ultramarine
Pink	Fe,	Cinnabar and red lake
White	Pb	Lead white
“Gold”	Pb, Sn, Fe	Lead white, tin-lead yellow and ochres
“*Incarnato*”	Pb, Fe, Ti, K	Lead white and ochres
Darker areas (shadow)	Fe, K, Ti	Addition of ochres
	Hg	Addition of cinnabar
Brighter areas	Pb	Addition of lead white

Table 4.2. Pigments used for paint this baroque canvas

4.1.3. Modern period: “Misure e Curvature” by Bice Lazzari

The historic evolution of pigments is closely related to developments in technology and chemistry. Before the Industrial revolution, the range of colours available for art was limited, as most of the pigments in use were earths and other mineral pigments. In addition, some colours were costly or impossible to obtain. The industrial and scientific revolutions brought a huge expansion in the range of synthetic pigments, manufactured or refined from naturally occurring material, such as cadmium yellow (1825), artificial ultramarine (1829), cobalt blue (1810) and many others [69]. In particular, starting from the second half of the 17th century, new white pigments were studied, in order to substitute the toxic lead white (widely used in the past), such as zinc white[12] (late 1700), Blanc fixe[13] (late 1700), titanium white[14] (1800)

---

[12] Zinc white (ZnO) has now almost the same importance that the lead white had in the past for artists . There are many processes to produce this pigment. The most used is the French method of manufacturing, also known as

and lithopone (late 1800)[15]. Anyway, all these pigments became really available as pigments for art work starting from 1900 [67].

In this paragraph, results referred to the painting "*Misure e curvature*" by Bice Lazzari (1967) are presented, more detailed than those shown in par.3.3.1, in order to give information also about pigments used in modern times. This artwork is a canvas painted with a white tempera, on which the artist has drawn up thin lines with graphite (Fig. 4.6). Later, some *lacunae* formed in the opera were restored by using a titanium-white pigment.

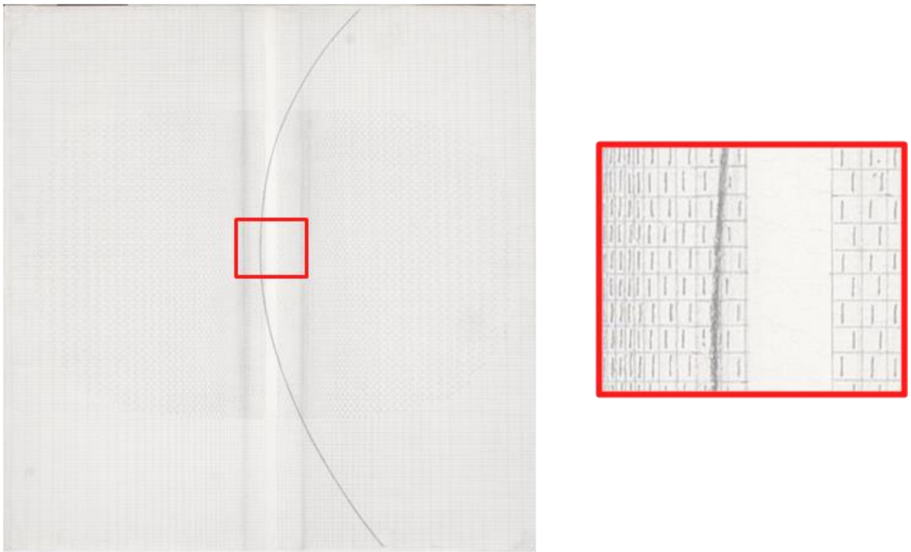

Figure 4.6. *"Misure e Curvature"*, painted by Bice Lazzari. On the right, a detail of the painting is shown, to make it possible to appreciate the painting and drawing technique

Sixteen areas were acquired, selected in order to distinguish the original white Ba-based pigment from the restoration titanium white. Actually, both pigments are white and the painting layer exhibits apparently uniform surface, making the restored *lacunae* not easily identifiable by visual examination (details in Fig. 4.7). The analysed areas (in total 130 cm^2)

"indirect process", in which zinc vapor is produced from molten metallic zinc, burned in an oxidizing atmosphere at temperature of 150 °C. The white oxide fumes are collected in a series of chambers

[13] Blanc fix ($BaS0_4$) is the name given to the artificial barium sulphate made by the precipitation of barium chloride solution with sodium sulphate. It is not opaque enough to be ground alone, therefore it is generally added to other oil pigment

[14] Titanium white (TiO_2) is the whitest pigment and has the greatest hiding power. For the preparation of this pigment, the principal titanium ore (ilmenite) is digested with concentrated sulphuric acid, and the coagulated mass of impurities (iron and titanium sulphates) which is formed is dissolved in water. The so-obtained precipitate is neutralised with barium carbonate and is then calcined

[15] Lithopone is a co-precipitated pigment, which is made by adding zinc sulphate to a barium sulphide in solution ($ZnS + BaS0_4$). This pigment can be obtained also by a precipitation of zinc sulphate and barium sulphate, such as the Blanc fixe

were acquired in 3 hours and 46 minutes. For all measurements, the conditions were: 35 kV anode voltage, 100 µA anode current, 1 x 1 mm^2 pixel size, and 1mm/s scanning speed.

In the following, two examples of the distribution maps of the main elements are reported.

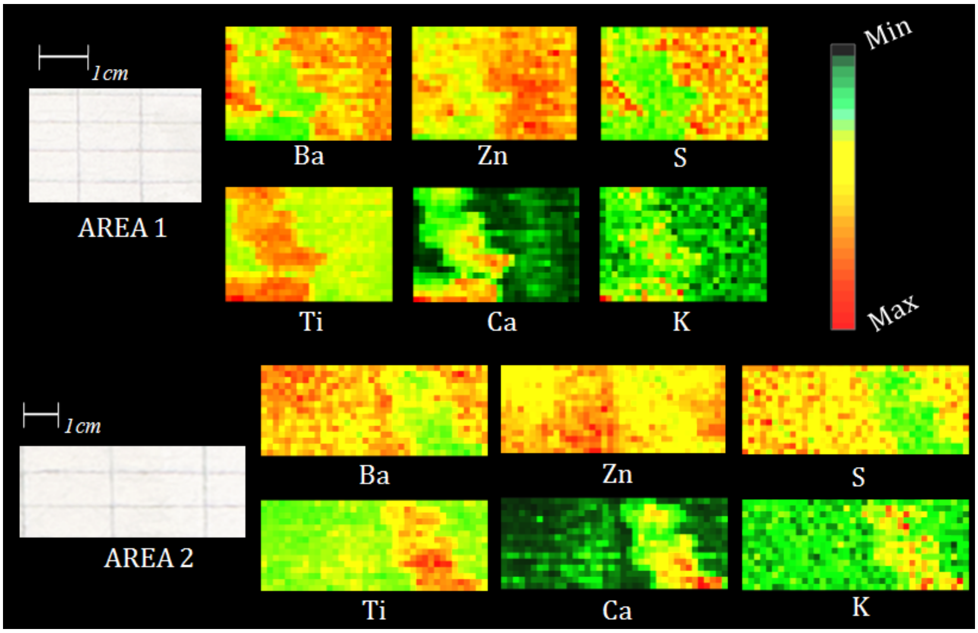

Figure 4.7. XRF elemental maps of the area surrounding the restored *lacuna*. The results for Ba, Zn, S, Ti, Ca and K maps are shown. The figure reports one example of discrimination between the original pictorial layer and the restored part

The Ba and Ti distributions, in both areas, allow for a clear identification of the position and dimension of the *lacunae* (restored with Ti-white) and the characterization of the surrounding original Ba-based pigment. Same conclusions have been obtained for the area shown in par. 3.3.1 and for all the others, not reported here for brevity.

In the original pictorial layer, in addition to Ba, also the presence of Zn and S can be noticed. The co-presence of these three elements might indicate that the original painting layer is composed by lithopone ($BaSO_4$ + ZnS) or by a mixture of Blanc fixe (barium sulphate) and zinc white.

For the two examples in figure 4.7, also the Ca and K maps are reported, to point out the information on the deeper layer of the painting, as already explained for the case study on "*La Muta*" (Pg. 67). The Ca and K distributions, probably due to the Ca-based preparation layer and the canvas respectively, are similar to the Ti one. In both areas, inside the lacunae, Ca and K show higher intensities than outside, attesting the loss of the original Ba-painting layer and the lowered absorption due to the present pictorial integration, made of a lighter Z element.

A similar behaviour is present also in the AREA3 (Fig. 4.8, black circle), where a thinning of the painting layer is pointed out by the simultaneous decrease of the Ba- and the increase of the Ca-intensity, which strengthen the idea of a deeper Ca-based preparation layer, probably gypsum.

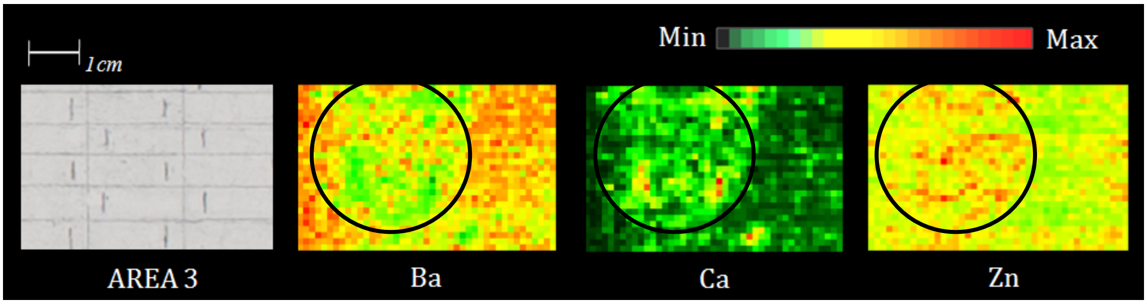

Figure 4.8. XRF elemental maps detail an altered area. The results for Ba, Ca and Zn are shown. The figure presents one effect of the painting layer degradation processes

In correspondence of the thinning of the painting layer of the AREA3 (Fig. 4.8), the Zn shows the same distribution of Ca (deeper preparation layer) and a distribution complementary to the Ba one (painting layer). These considerations suggest the existence of two different Zn sources, both in the painting layer and in an intermediate layer (imprimatura).

Summarizing, the obtained results suggest this structure for the painting (front to back): shallow pigment layer (Ba + Zn), intermediate imprimatura (Zn), preparation layer (Ca) and canvas (K). This hypothesis is also strengthened by the comparison of the spectra acquired both on the front and on the rear side of the painting[16] (Fig. 4.9).

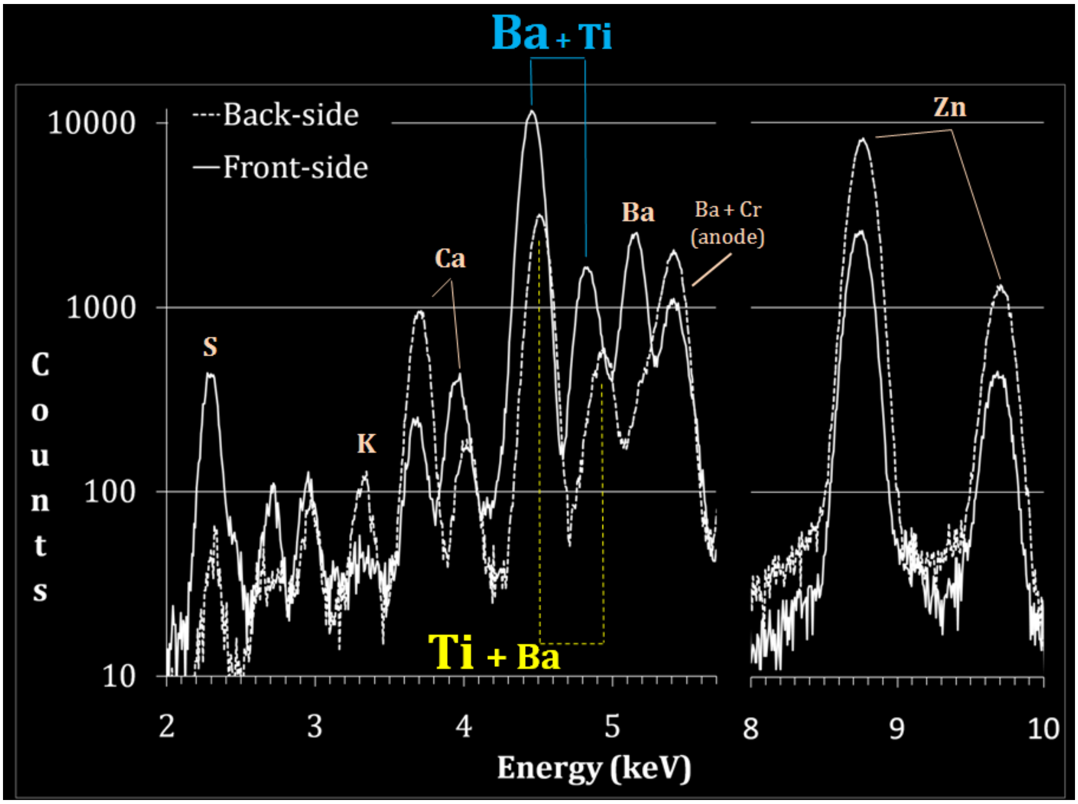

Figure 4.9. Spectra are obtained on the same number of pixels on the front- and the back- side of the painting. The elements useful for the discrimination between the different layers composing the paint are highlighted in different colours

When passing from the spectrum of the front-side to that of the rear-side, a clear increase of the K and Ca counts can be noted, thus confirming the rear surface as their origin. In the same way, the increase of Zn counts, in conjunction to the decrease of the Ba counts, can be noted. This supports our interpretation of a double Zn source, both in the painting layer and in an intermediate imprimatura. Actually, in the case of a unique Zn source in the painting layer, a decrease of Ba counts should be accompanied by an even higher Zn counts decrease (being Z_{Zn} lower than Z_{Ba}), which is not the case.

---

[16] Spectra acquired on the same number of pixels on the front- and the back- side of the painting. In this way the spectra can be directly compared, as they have been obtained in the very same experimental conditions (same area, measurement time, geometry and acquisition parameters, such as HV and current of the X-ray tube, etc.). Therefore, the differences of the two spectra can only be due to different sample compositions

4.2 Manufacturing processes: Gilding technique

During my PhD training, I also had the opportunity to analyse different typologies of gildings. Thanks to the chemical characterisation, it was possible to achieve information about the manufacturing processes and to characterise the employed metals.

As any other artistic technique, over the time the gilding technique has evolved, both from the material and the technical point of view, in agreement with the style of the religious period. Indeed, gildings were usually privileged for artworks or decorations in religious art production (such as gilded sculpture, icons, illumination of religious manuscript...), highlighting the prosperity of monarchs.

Basically, "gilding" is the process of covering an item with a thin layer of metal foil, usually gold. The application of other types of metals may also be referred to as "gilding". The gilding techniques have been various and differed, even in the same period of time, depending on the artist, the customer, the geographic contexts and the style of the gilded areas. In this chapter, I report two case studies referring to two different gilding techniques used in the same historical period (around 1300).

4.2.1 Illuminated parchment

The first example refers to a fragment of an illuminated manuscript, dating from about AD 1340, previously mentioned in Chapter 3. The sample, consisting of a vellum sheet, is a musical notation, composed of a system of six tetragrams on each page, with neums and text of the chant written in *littera rotunda* and decorated with calligraphic initials and a figured illuminated letter (Fig. 4.10).
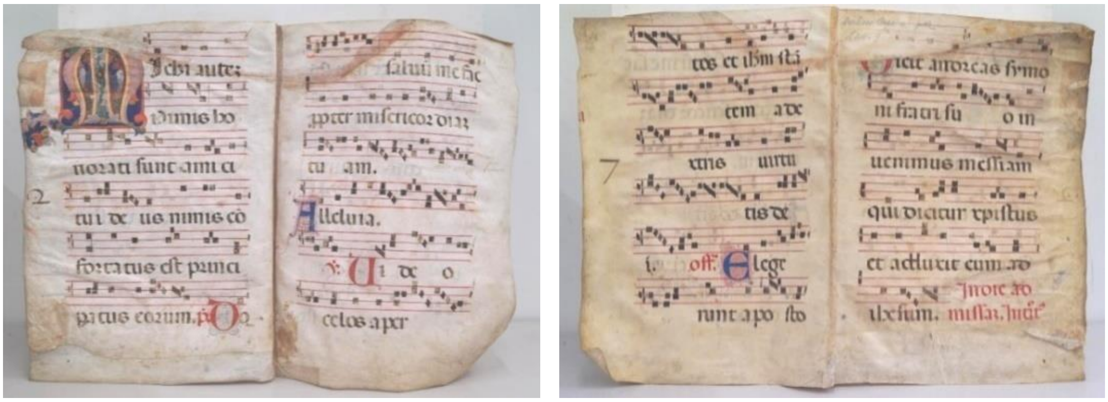
Figure 4.10. Image of the front and back side of the antiphonary

The analysed areas (in total 140 cm^2) were acquired in 4 hours and 35 minutes. For all the measurements, we used 35 kV anode voltage, 100 µA anode current, 1 x 1 mm^2 pixel size and 1mm/s scanning speed.

The calligraphic initial of the antiphonary is enriched with several gilded circular decorations (optical image in Fig. 4.11), which were analysed in order to understand the material composition and the gilding technique.

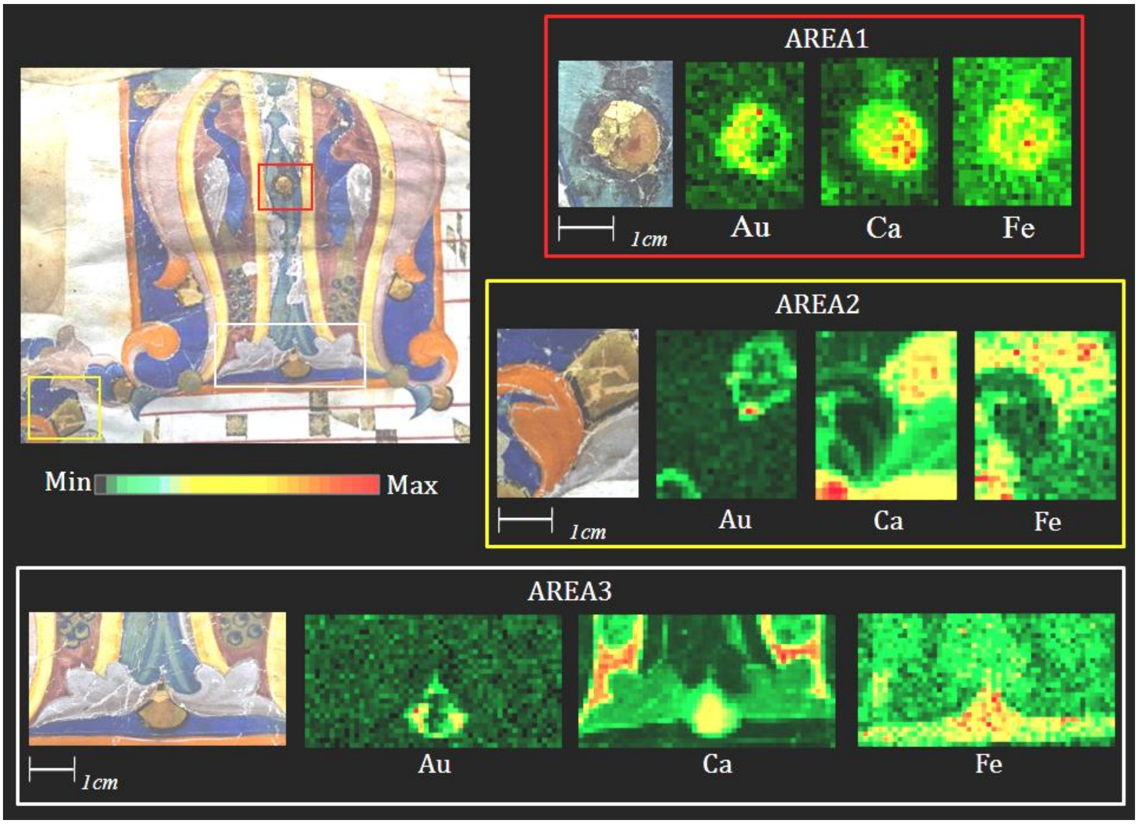

Figure 4.11. Details of the calligraphic initial, where the gilded circular decorations are clearly visible. The Au, Ca and Fe elemental maps of three different gilded decorations, highlighted in the optical image with colour squares, are shown

All the analysed areas show the presence of Au in correspondence to the decorations. The Au spatial distributions are basically concentrated along the border of the decorations, thus suggesting a partial loss (detachments) of gold occurred over the time. Therefore, the hypothesis of the use of pure gold as original precious material in gildings can be done.

Inside the gildings, we can note the co-presence of Fe and Ca, with spatial distributions largely overlapping the Au one and with intensities much higher here than in the surrounding areas. Residuals of calcium can be found in parchment, as during the manufacturing process the vellum sheet was usually treated with slaked lime ($Ca(OH)_2$) in order to obtain a suitable support for writing. In correspondence to the gilded decoration, the Ca distribution is too intense to be only due to the presence of this element in the support, as can be easily seen by comparing the Ca intensity inside the gilding and outside, throughout the whole analysed region. This suggests the presence of a Ca-based preparation layer (such as gypsum) for the gilding.

The presence of Fe, instead, suggests a priming, also known as "Armenian bole" or "*bolus*"[17] [62**],** usually applied to flat and fine gypsum ground (mixed with organic glue) [70]. The use of this type of multi-layer preparation has a double function: a chromatic one, because the bole gives a warm red or ochre tonality to the hue of the gold surface, and supporting one, as the preparation allows further treatments of the metallic foil, such as for example burnishing [62; 71].

All these pieces of information allowed me to suppose that the gilded decorations were made of pure gold leaf, applied with the water/oil gilding technique ("*a guazzo"*)[18].

These conclusions are also confirmed by the observation of the macro optical image (Fig. 4.12), where the gold metal foil residuals and the red bole preparation can be appreciated.

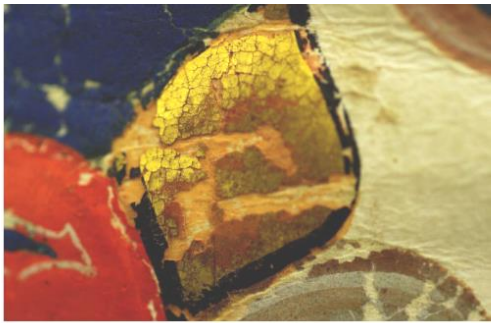

Figure 4.12. Macro optical image details one gilded decoration of the Antiphonary calligraphic initial

4.2.1 "Crocifissione" by Simone Martini

The second example concerns some results obtained by the analyses on the "*Crocifissione*" painted by Simone Martini during the first half of the 14th century. He was one of the major figures of early Italian painting, of great influence on the international gothic style. Simone Martini is also known for its skills in miniature painting and gilding decorations. This is clearly visible in the picture of fig. 4.13 and in the details of figure 4.14of the "*Crocifissione*", in which Simone Martini used several typologies of decorations to adorn the background of this religious artwork.

---

[17] Usually bole is a mixture of iron-rich clay (or ochre) and animal glue. Therefore, the characteristic spectrum of this coloured layer (from yellow to red) is similar to that one of the natural hearts, shown in par. 4.1.2

[18] As obvious, these two gilding techniques exploit respectively water and oil or resins (or a mixture of them) for the adhesion of the gold leaf to the preparation. With the XRF technique it is not possible to have information about water organic compounds

Figure 4. 13. The "*Crocifissione*" by Simone Martini

For the diagnostic campaign carried out before the restoration, in collaboration with the *Opificio delle Pietre Dure,* twenty areas (in total 236 cm^2) were acquired in 6 hours and 41 minutes. For all measurements, the measurement conditions were: 35 kV anode voltage, 100 µA anode current, 1 x 1 mm^2 pixel size, and 1mm/s scanning speed.

In Fig. 4.14, two different gildings are shown: a brighter continuous band ("Gilding Bright") and a darker, diamond-shaped band ("Gilding Dark").

Figure 4. 14. Detail of the wood panel to highlight the brighter continuous band ("Gilding Bright") and the darker band with diamond-shaped decorations ("Gilding Dark")

In Fig. 4.15, I report the results obtained in two different regions (AREA1 and AREA2), in which both the types of gildings are present. The obtained-results allowed me to identify the manufacturing process of exploited gilding technique.

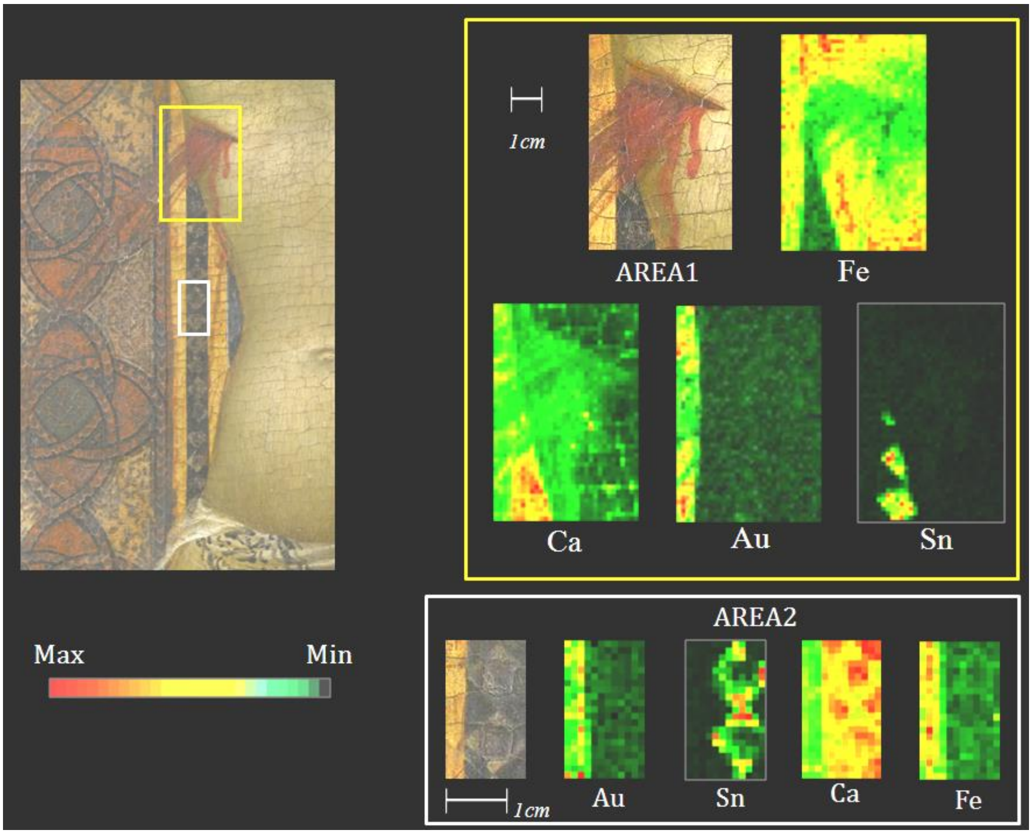

Figure 4. 15. The figure reports the Ca, Au, Sn and Fe elemental maps obtained on two areas in which both the Gilding Bright and Gilding Dark decorations are present

The elemental maps concerning the "Gilding Bright" show results similar to those obtained for the gilded decorations of the parchment. Indeed, in both AREA1 and AREA2, the Au and Fe distributions are clearly visible and largely overlap, suggesting also in this case the application of the gold foil on an iron-rich bole with the"*a guazzo"* technique.

A difference can be found in the Ca distribution maps of the two areas; indeed, this element is present throughout all the analysed areas, a clear indication of the use of a Ca-based preparation, probably gypsum, as painting background. This conclusion is confirmed in particular by the Ca map of AREA1, which is characterised by higher Ca intensity in correspondence to the pattern of cracking occurred in the pictorial surface (*craquelures*). These *craquelures* leave uncovered the Ca preparation layer and allow the low energy Ca X-rays reaching the detector instead of being absorbed in overlaying layers, as in the case for the *craquelures* in the pictorial layer of the Christ's ribs (right side of the AREA1).

About the "Gilding Dark", different results, both for the metal used and the application process, have been achieved. First of all, the Sn spatial distributions of both areas, corresponding to the diamond shapes (Fig. 4.15), suggest the use of a tin foil, cut into single pieces, and highlight the goldsmith's skill of Simone Martini. This is particular evident in the Sn maps of AREA1, where the "Gilding Dark" decorations follow exactly the form of the body (on the left of the area).

In addition, in correspondence of the diamond decoration, no Fe seems to be present, thus suggesting the absence of the bole.

In conclusion, for the "Gilding Dark", I hypothesise the use of a tin foil applied with mordant (*a missione*). Indeed, in this technique, the bole is substituted by an oily-resinous mordant, which sometimes was added with pigments, as driers, and varnishes. This conclusion is strengthened by the ancient recipes [62], where this type of gilding is usually recommended for small details, as the small carved pieces of tin foil used by Simone Martini for the "Gilding Darks".

4.3 Alterations and restorations

As it is well known, during aging all the parts composing the artworks (from support to surface varnishes) undergo several degradation processes, as a result of external and intrinsic causes, compromising the conservation state of artworks. Different damages can occur depending on the materials composing the artworks, the manner in which they are preserved and the environmental conditions. Therefore, degradations can have different magnitude and affect different parts of the artworks: from structural changes (decrease of stability and strength of material support) to surface changes (colour change, formation of patinas or alteration products, degradation of the painting layer even up to its detachment and loss). Therefore, over the time, a work of art can undergo several restoration or conservation treatments, also regarding different areas depending on the damages gradually occurred.

For this purpose the XRF imaging is a useful tool, as it allows obtaining information on the conservation state and about restorations occurred over the time. Indeed, usually this technique can be used to locate previous restorations, as in the case of the Lazzari's painting (par. 4.1.3), as well as to detect inorganic alteration products.

4.3.1. Alterations

A complete analysis of the state of conservation of the paintings represents a noticeable aid and guide for its restoration, taking into account the severe damage due to natural decay processes. In this case, the XRF imaging can provide valuable information for correct planning of the cleaning procedures.

One example of decay products are the metal oxalates, which are usually associated with greyish-brown, highly insoluble surface films (crust or *patina*), in addition to other degradation products (sulphates, nitrate and/or chloride). Copper- and calcium- oxalates are usually formed from the alteration of organic ground layer preparations[19], binders for pigments[20], finish coatings[21] (such as varnishes), other organic compound and/or from the presence of anthropogenic pollutants [72]. The organic substances frequently used in the past and cited as ingredients of ancient recipes are generally natural compounds, such as sugars and carbohydrates, proteins, oils and lipids, or resins.

The study of the origin of these alteration films and the role of the organic substances, which could have been applied on the artwork surfaces, is still open. Indeed, two different hypothesis are still discussed: one suggests a common biogenic origin, in which the oxalates are formed as by-product of microorganisms' metabolism of organic compounds [73]; the other consider the oxalate films as a product of the oxidative degradation of ancient organic treatments applied on the surface by reactive species present in the natural and polluted troposphere [74; 75].

During the analyses of the conservation state, it is frequent to detect oxalates together with other degradation products, even when there is no evidence of their presence by visual observation. This has been the case of the "*Adorazione dei Magi*" (Fig. 4.16), an early painting of Leonardo da Vinci, commissioned by the Augustinian monks of San Donato a Scopeto in Florence during 1481. Unfortunately, the following year Leonardo departed for Milan and he left this work unfinished. Therefore the painting is manly composed of few materials: gypsum for the preparation layer, lead white for the imprimatura and a black pigment for the underdrawing. No painting layer was added, as the painting is unfinished. This feature makes it of extreme importance, as it allows for a deepened understanding of the technique used by Leonardo to create the preparation and the underdrawing. For its high historical and technical value, besides the beauty, the panel is exposed to the *Galleria degli Uffizi* in Florence.

Over the time, some conservation treatments occurred; in particular, several coatings and glue layers were added over the original materials.

---

[19] Ground layer preparations can have different compositions, depending on the artworks manufacturing period: basically they are a mixture of an inorganic filler and an organic adhesive. The former is usually gypsum, calcium carbonate or silica, and the latter are animal glues, starch, sugar and oils

[20] For adhering to the preparation, a binder have to be added to the pigments, in order to obtain a homogeneous and solid layer. Also in this case, different typologies of adhesive can be found in literature, depending on the painting techniques: animal glues, gums, whole cows' milk, casein, albumen and yolk from eggs, oils

[21] Varnishes overlying the painting layer can have different compositions on the bases of their role, such as finishes/protective coating or restoration treatments occurred during time for making again bright the painting layer. Therefore, discrimination among different varnishes can be hard. Usually they are mainly composed by mixtures of organic compounds, such as sugars, proteins, Arabic gum, molasses, oils and lipids and resins

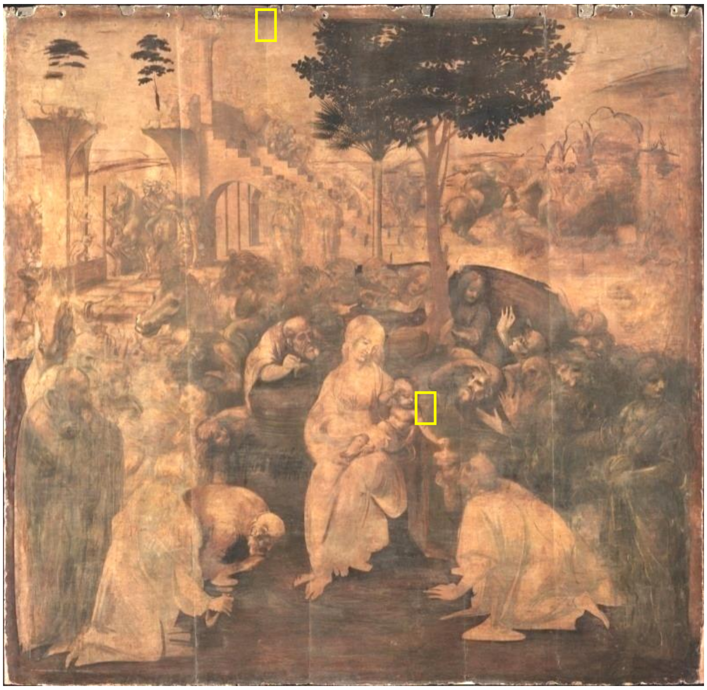

Figure 4. 16. “*Adorazione dei Magi*” painted by Leonardo da Vinci

In order to characterise the original materials composing the artwork and evaluate its conservation state, eleven areas (in total 138 cm^2) were acquired in 8 hours and 9 minutes. For all measurements, I worked with 35 kV anode voltage, 100 µA anode current. Due to the many issues raised by the restorers and art historians, different pixel size (1 x 1mm^2, 500 x 500 µm^2 and 250 x 250 µm^2) and scanning speed (1 mm/s, 500 µm/s and 250 µm/s) have been used, depending on the analysed area.

The most interesting results concern the varnishes and the cleaning procedure carried out by the restorers. In the following, the elemental maps of two areas (yellow squares in Fig. 4.16) are reported, as they resulted of great interest for the above-mentioned issues.

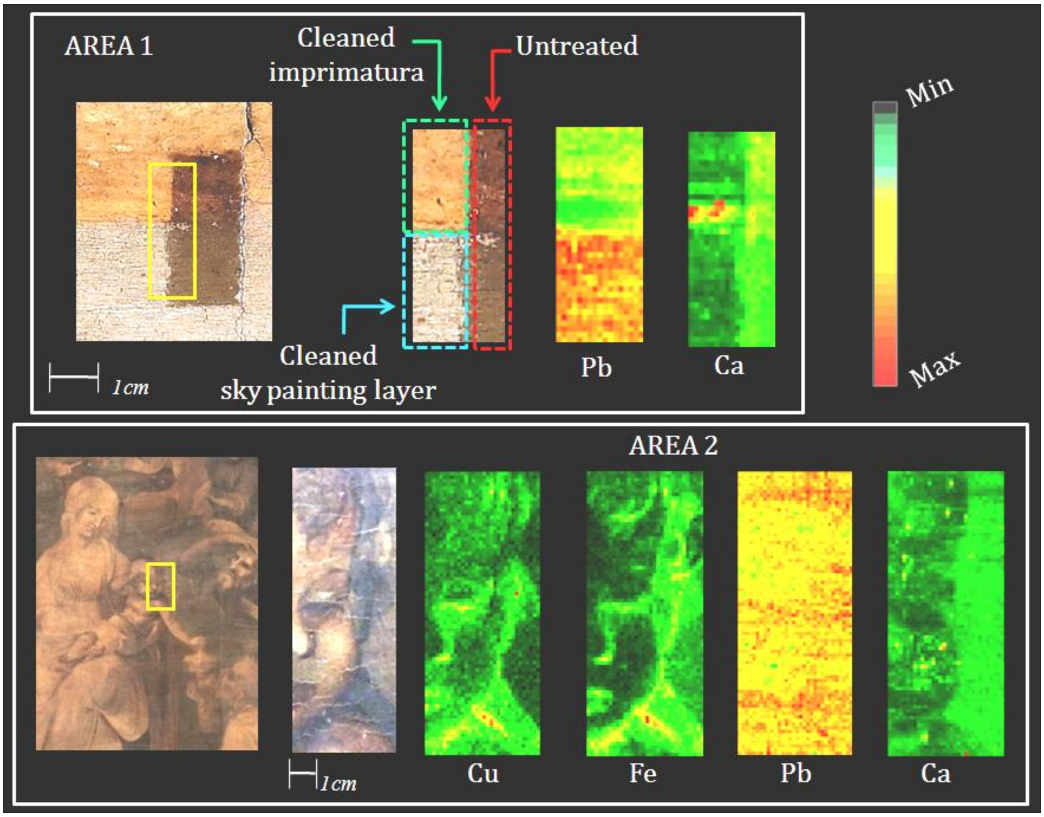

Figure 4. 17. Details of two different areas: AREA 1 in the sky, near the frame in the upper part of the paint; AREA 2 on the Child's face. Both areas were acquired with a 500 µm pixel size and 1 mm/s scanning speed

In the Fig. 4.17, the AREA1 is reported together with the Ca and Pb maps. The studied region is divided in two parts: the left-hand side was cleaned before the XRF analysis, the other was left in its pristine conditions.

The AREA1 is mainly characterised by Pb, confirming the use of lead white for the imprimatura and suggesting the addition of this pigment to paint the sky. Indeed, the Pb distribution is not homogeneous, showing a higher Pb quantity in the lower part of the area.

In addition, from the image 4.17, it is possible to notice that the Pb remains "horizontally" homogeneous passing from the cleaned to not cleaned zone, and thus it acts as homogeneous absorber for any contributions from underlying layers. Therefore, the "vertically" homogeneous and intense Ca region distributed in the non-treated area indicates that the X-rays of this element originate from a shallow layer, suggesting the presence of calcium oxalates as degradation compound in the varnishes. This result was also confirmed by further analyses carried out by the scientific laboratories of the *Opificio delle Pietre Dure*.

For the AREA2, the Cu and Fe maps are reported in order to characterise the composition of the black underdrawing. The co-presence of these two elements suggests a mixture of a copper-based pigment, probably azurite considering the hue of the colour, and a natural earth.

The conservation treatment of the AREA2 has given me the chance to show, in an important case-study, that XRF imaging is really a helpful tool and a useful guide for the restorers during cleaning treatments. As we can see in AREA2 of Fig. 4.17, the Pb distribution is almost homogeneous, so no Ca contribution can come from the underlying gypsum preparation layer, as explained in the previous example. Therefore, any structure present in the Ca maps must be due to a shallow contribution, in this case the above-mentioned decay products, not removed by the cleaning process. Thus the Ca intensity distribution variations in the maps must be connected with the cleaning treatment intensity, which was different for the diverse parts of the painting. Ca is more abundant in the darker than in the lighter areas, thus suggesting a milder treatment to remove varnishes over the underdrawing, probably to avoid also the removal of the original black pigment. There are really very few cases in which it is as crucial as for the *"Adorazione dei Magi"* to maintain as much as possible of the original materials, being one of the few available paintings where it is possible to carry on a deepened study on the materials and techniques used by Leonardo to prepare the underdrawing.

4.3.2. Restorations

In this paragraph, some examples are presented in order to highlight the usefulness of the XRF imaging technique to easily and quickly evidence the presence of restorations.

Detecting materials incompatible with the time period of the artefact or obtaining the evidence of anomalous distribution of particular elements can be a strong hint of repaints and/or integrations. In addition, considering that different pigments have been introduced at diverse times (as already explained in par. 4.1.3), it is possible to reconstruct the period of the artwork manufacturing and sometimes to get precious information about the restoration history [76]. Typical examples of pigments providing precise time-stamps are the zinc white, used up to the 19th century, and titanium white, introduced only after the1920s [77]. Both were commonly used in pictorial integration as white pigments or as priming for other pigment.

The first example of discrimination of pictorial integrations from original pigments concerns the "*Madonna del coniglio*" painted by Edouard Manet during the 19th century (Fig. 4.18). In this work, commissioned by a private costumer, it was necessary to characterise the painting palette, the execution technique and identify possible additions made during previous restorations in order to plan a correct restoration plan.

Figure 4. 18. “Madonna del coniglio” painted by Manet

The analysed areas (in total 215 cm^2) were acquired in 5 hours and 35 minutes. For all measurements the conditions were: 25 kV anode voltage, 100 µA anode current, 1 x 1 mm^2 pixel size, and 1mm/s scanning speed.

As examples, two different areas related to pictorial integrations are shown in Fig. 4.19.

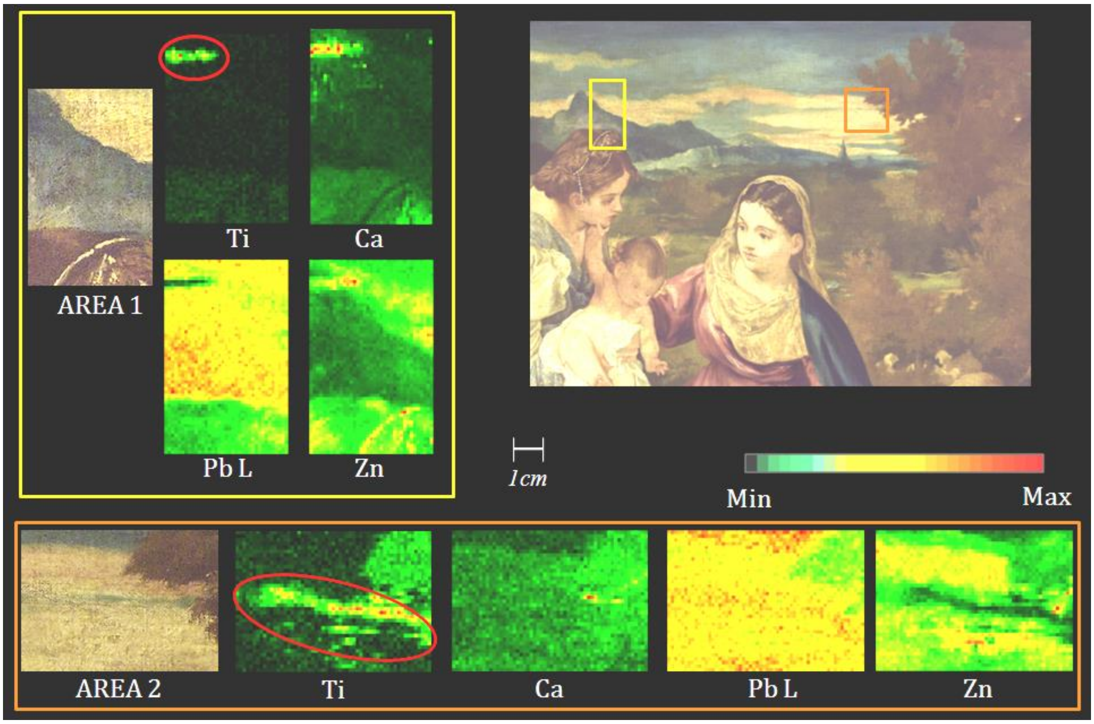

Figure 4. 19. A section of the painting detailing the sky near the mountain and near the tree. The Ti, Ca, Pb L and Zn maps are reported, in order to highlight how anomalous elemental distributions can help in finding restorations

From the image, it is clearly evident that both the restorations (red circles) are characterised by Ti, suggesting the use of titanium white.

From the Pb L, Ca and Zn elemental maps, some differences in the integration procedures can be pointed out. Indeed, for the upper part of AREA1, the contemporary strong decrease of Pb and the increase of Ca suggest the presence of a lacuna in the lead white imprimatura, subsequently restored with a Ca-based material integration (i.e. gypsum).
In AREA2, as only the Zn elemental map shows a decrease in correspondence of the Ti restored part, it is reasonable to hypothesise a simple pictorial integration of a damage occurred to the pictorial layer.

In addition, comparing the Zn distribution maps of the two areas, a further piece of information can be extracted. Indeed, in correspondence of the restoration of the AREA1, Zn and Ti show a similar spatial distribution, while in AREA2 this does not happen. As said, this can suggest a double use of the titanium white: in AREA1, it was applied as priming for- or in mixture with- a Zn based pigment, such as the zinc yellow[22], visible e.g. in the coronet of *Santa Caterina*, while in AREA2 the titanium white was used in pictorial integration simply as white pigment.

Different pictorial integrations were also found in the "*Crocifissione*" by Simone Martini, already presented in paragraph 4.2.2 for the study of the gilding techniques. In this case, we turn the attention to the *velatura* of the Christ's loincloth (Fig. 4.20).

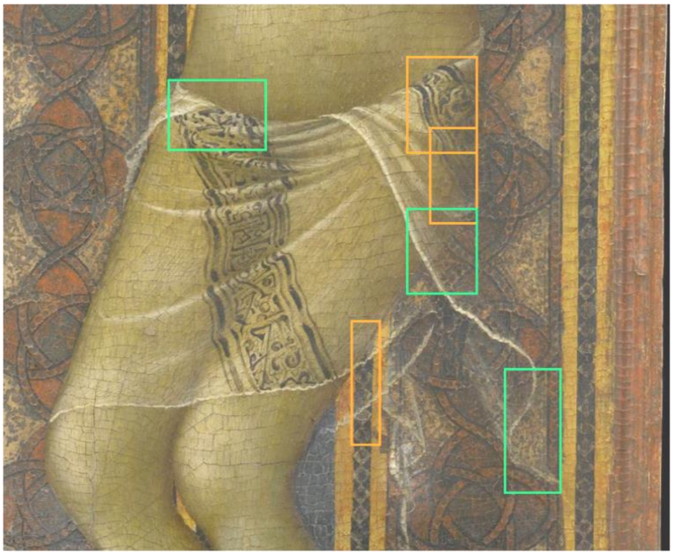

Figure 4. 20. The Christ's loincloth. Coloured shapes highlight the investigated areas. In the following we will briefly discuss the results of the analyses carried out inside the green ones

The most interesting results concerning the chemical composition of the original and restoration materials were found in correspondence of the three areas highlighted with the green squares (among the six studied on the loincloth,Fig.4.20),which are reported hereafter.

---

[22] From the study of the other areas, a Zinc yellow was identified inthe halo of the baby and the clouds. It was also possible to point out that the Zn yellow was also added to other pigment for obtaining brighter areas

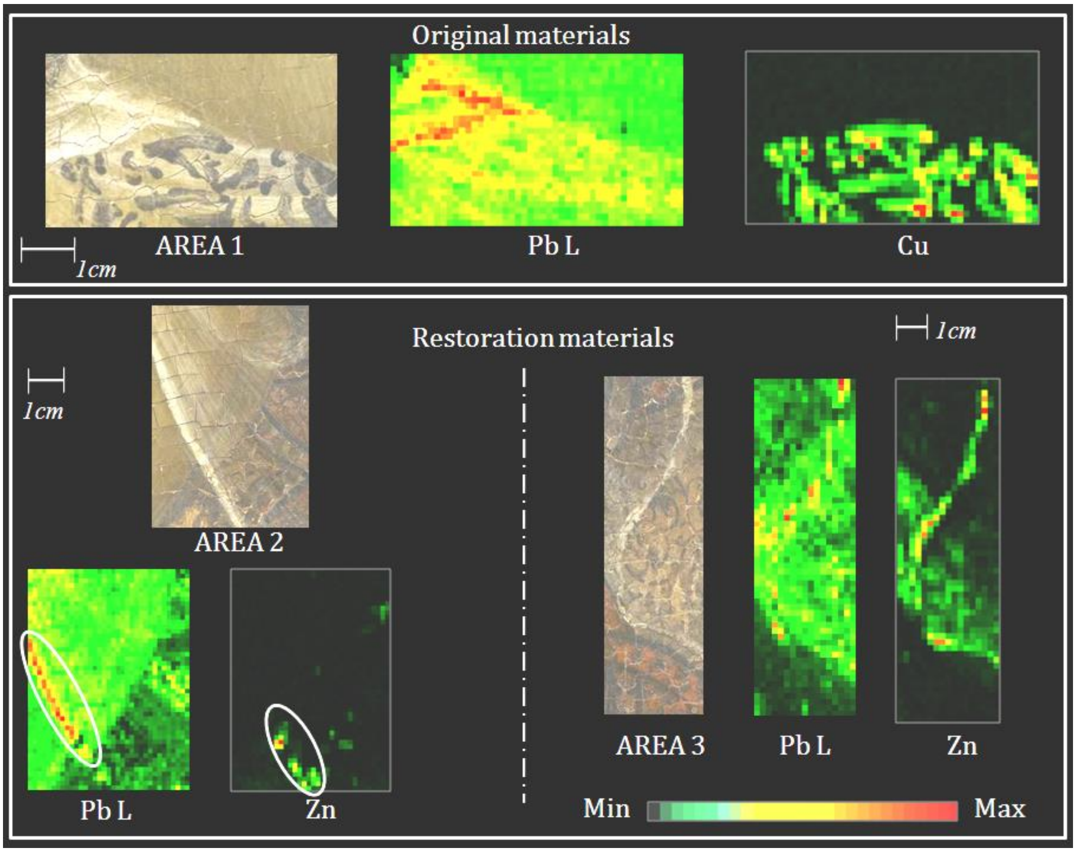

Figure 4. 21. The Cu (only for the original part), Pb L and Zn (only for the restoration) maps of the three studied areas are reported, as they allow highlighting the chemical composition of the original and restored parts

The elemental maps of the non-restored loincloth (AREA1) clearly indicate that Simone Martini used a lead white for painting the *velatura*, upon which is laid the black decoration, mainly composed by a Cu-based pigment (considering the hue of the colour, it is reasonable to hypothesise the use of Azurite).

In AREA2 and AREA3, the co-presence of Pb (related to residuals of the original lead white) and Zn suggests the use of zinc white for pictorial integrations of the loincloth, as clearly visible in AREA2, where the white edge of the loincloth resulted to be painted partly with lead white (circle in Pb L map) and partly with zinc white (circle in Zn map).

Also for the gildings, the pictorial integration is a common practice, above all when the loss of the metal foil compromises the properly “reading” (integrity) of the artworks, decreasing their value. Sometimes, the taste of the époque or the antiquity market imposed spurious intervention. In many cases the original gilded layers could be replaced by cheaper materials [78]

In the following, an example concerning pictorial integrations in gildings is shown. The discussed restoration concerns the illumination of the manuscript described in par. 4.2.1.

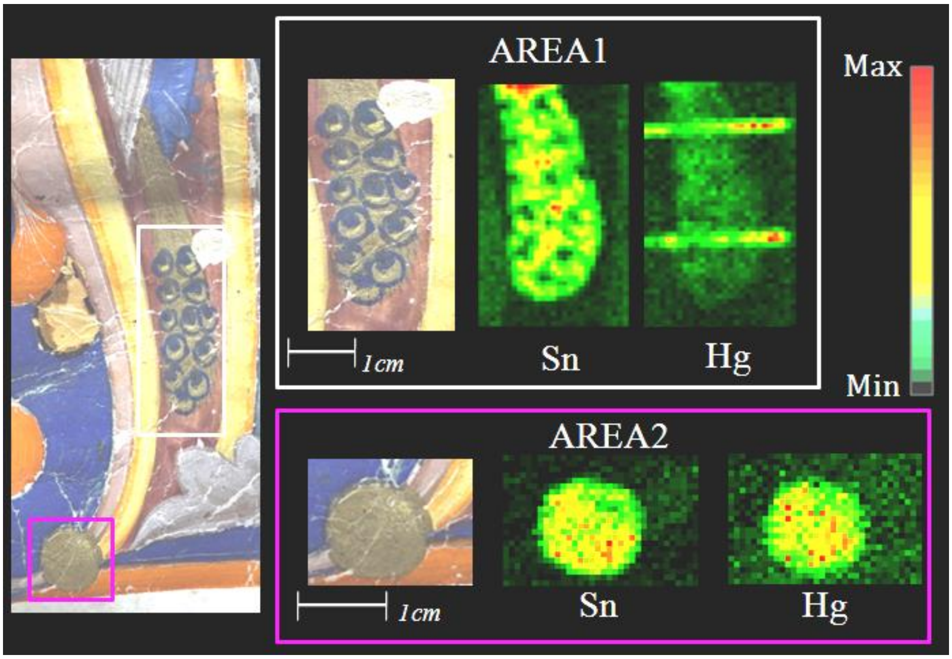

Figure 4. 22. Two scanned areas are shown. Their Sn and Hg distribution maps are reported, in order to characterise the chemical composition of the gilding restoration material

As seen in the previous paragraph, the original gilded decorations of the parchment are made with a pure gold metal foil, applied *a guazzo* on an iron-rich bole imprimatura. In Fig. 4.22, the peacock’s tail and a circular decoration are shown. In both gilded areas, Sn is clearly visible and its presence suggests the use of a tin-rich pigment, most likely a stannic sulfide, known also as Purpurin or Mosaic gold[23], one of the most important gold surrogates, highlighting the presence of restoration material [79].

---

[23] Mosaic gold is an artificial pigment, which looks like bronzing powder. It was developed in China around. 300 AD. In Europe this pigment was developed much later and has been identified in various manuscripts and paintings from the fourteenth and fifteenth centuries, occasionally on medieval manuscripts

This hypothesis is strengthen also by the Hg distribution, largely overlapping the Sn one, as the starting material for the Purpurin preparation is basically a solution formed by Sn, S, Hg and ammonium [62;80].

Finally, it can be noted that, in the peacock's tail, the Hg map shows two horizontal lines, not present in the visible image of the front side of the sheet. Thanks to the trans-illumination image (Fig. 4.23), it is possible to easily explain this "anomalous" feature. Indeed, these Hg contributions are due to the musical staves in the back side of the sheet, painted with cinnabar (HgS), as can be seen in the figure below.

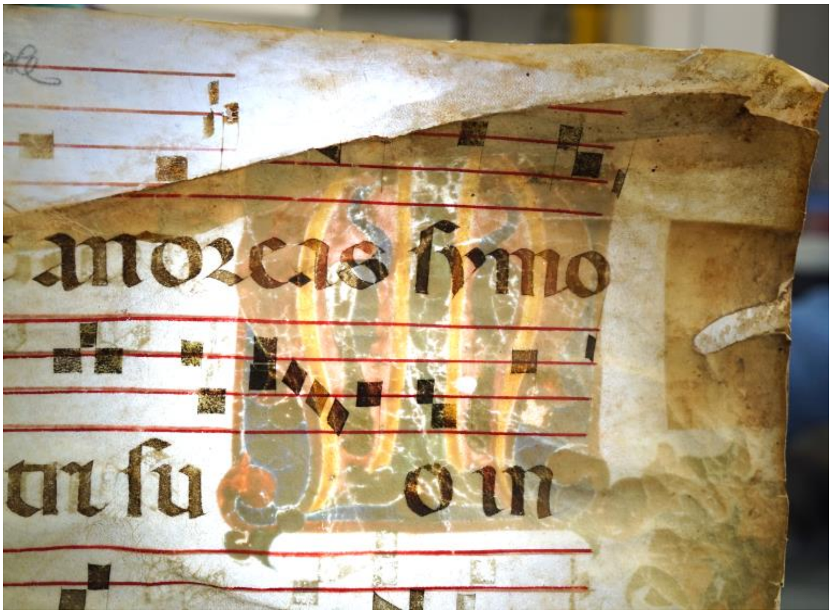

Figure 4. 23. Transillumination image of the illuminate calligraphic initial

FINAL REMARKS AND FUTURE PERSPECTIVE AT THE LABEC LABORATORY

Thanks to the results obtained working with the XRF1 scanner, developed at Labec laboratory before my PhD training, it was possible for me to point out pros and cons of this first-generation instrument, basing on the measurements that I personally performed on many CH samples and taking into account all the observations, comments and notes from conservation scientists, physicists, chemists, restorers and art historians I have been working with during the measurement campaigns.

On the basis of theXRF1 study, a second generation XRF2 scanner was implemented. This instrument is by far more compact, lightweight and easy-to-handle with respect to the XRF1 and it has extended capabilities. All these improvements and upgrades allow for overcoming the limitations pointed out for the XRF1. The many tests, carried out on laboratory samples and on real Cultural Heritage case studies, allowed me to confirm the correct functioning of each development and to evaluate the extended capabilities of the XRF2.

Let’s now briefly review the details of the main differences between XRF2 and XRF1.

First of all, the new Graphical Users Interface (GUI) is highly simplified with respect to the previous one and is now really user-friendly and fail-safe, as the many persons that have used and are still using the scanner can attest.

One of the main success of my PhD work has been the development of the dynamic positioning system, which automatically allows for maintaining constant the scanner-to-sample distance, and thus the irradiation and detection geometries, during the measurements. This feature is particular relevant in the CH field, where it is particularly hard to find artworks with flat/planar surface.

Diagnostic tests were carried out, with and without tracking system active, on lab sample (*tilted lead block*) and true CH objects (the “*Madonna con Bambino*”, a wood panel enriched with a tri-dimensional application, and a crumpled and undulated illuminated parchment).The obtained results point out how drastically the elemental maps are affected by sample-system distance variations.The differences between the measurements with and without the tracking system are highlighted by the comparison of the elemental maps obtained in the two configurations.These differences are higher for the low energy X-rays and get smaller at higher energies, but they never become negligible in the performed tests. The dynamic positioning system proved to really extend the XRF2 scanner capabilities. A widened range of non-planar sample geometries is now accessible, as the tracking system allows avoiding loss of information and prevents possible damages to the sample.

The XRF2 is now also able to reveal an extended range of low Z-elements, thanks to the helium flow, which allows minimising the absorption in air of the secondary radiation emitted by the sample with energies down to ~1 keV. The helium flow is directly controlled by the new GUI interface, where it is possible to switch on/off the gas flow and to set the desired flow rate. Thanks to this feature, it was possible to carry on a diagnostic campaign on a Roman Mosaic glass *tesserae*, mainly composed by low atomic number elements (Si, Al, Mg and K).

The capability of adjusting the parameters for detector signal manipulation were added in order to create a flexible software, which is able to work with different types of detectors and that allows optimising detector performances, such as, for example, the energy resolution (ER). ER has a great relevance in CH applications, as objects under study are intrinsically heterogeneous and thus composed by many elements, whose characteristic lines may overlap. This makes the material compositional identification challenging. Following my suggestions, the imaging software of the XRF2 system now allows for choosing any desired energy interval and it is not anymore mandatory to choose a pre-determined energy interval for creating the maps. Thanks to these improvements, in favourable cases, it is possible to distinguish the contributions of elements with partially overlapping lines. In the case study of the modern paint of Bice Lazzari, this capability allowed distinguishing the largely overlapping X-rays due to barium white (original pigment) and titanium white (restoration pigment).

Several software upgrades for acquisition and data analyses have been introduced and have shown their importance “on field”. A rate meter is now available in the GUI, which allows for a real-time indication of the detection count rate. In this way, it is possible to have preliminary information about the statistics acquired during the measurement, thus allowing for a correct planning of the measurements.

With this version of the acquisition program it is also possible to group the original 16384 channel spectra into 8192 or 4096 channel spectra, directly exploiting the spectrum GUI interface.

As my PhD thesis has been largely dealing with imaging data analyses, a program to convert our files into a format compatible with the PyMCA toolkit was implemented. In this way, it is now possible to exploit the PyMCA imaging toolkit. One of the most interesting and fruitful options for our applications is the possibility of combining several elemental maps to form RGB (red "R", green "G" and blue "B") composite images. Now, at a glance, the presence of intermediate colours clearly indicates the use of a material where two or more elements are simultaneously present.

The great potential of the XRF2 for imaging analyses in the CH field has been definitively demonstrated by the many diagnostic campaigns, summarized in chapter 4. Indeed, the XRF2 imaging analyses allowed me to answer to many questions raised by the restorers, such as, just to cite the most interesting:

- the identification of the painting palette, the discovery of "pentimenti" and the extraction of information about the stratigraphy, as in the case study of "*La muta"* by *Raffaello,* or the characterisation of modern pigments and the discrimination between the original pigment and the restoration one, as in the case of "*Misure e Curvature*" by Bice Lazzari;
- getting information about the manufacturing techniques. This has been the case, for example, of the study of the gilding decorations in the "*Crocifissione*" by Simone Martini, where the XRF analyses allowed to point out the co-presence of thetwo different gilding techniques, the "*a guazzo"* and the "tin foil";
- obtaining information on the conservation state to guide the cleaning procedures. The most striking example of this kind of study is the identification of the alteration products in the panel "*Adorazione dei Magi*" by Leonardo da Vinci;
- put into evidence the presence and characterise different pictorial integrations, such as for the paintings "*Madonna del coniglio*" by Manet, the "*Crocifissione*" by Simone Martini and for the gildings restoration in parchment.

Thanks to the extensive use of the XRF2 scanner, during the three years of my PhD, also some weaknesses were pointed out.

The acquisition in scan mode is too slow. To overcome this limitation, we have started the development of a new prototype based on a *XRF multi-sensor detection system* (Fig.C.1), in order to increment detector active area and thus to allow speeding up the acquisition in scanning mode.

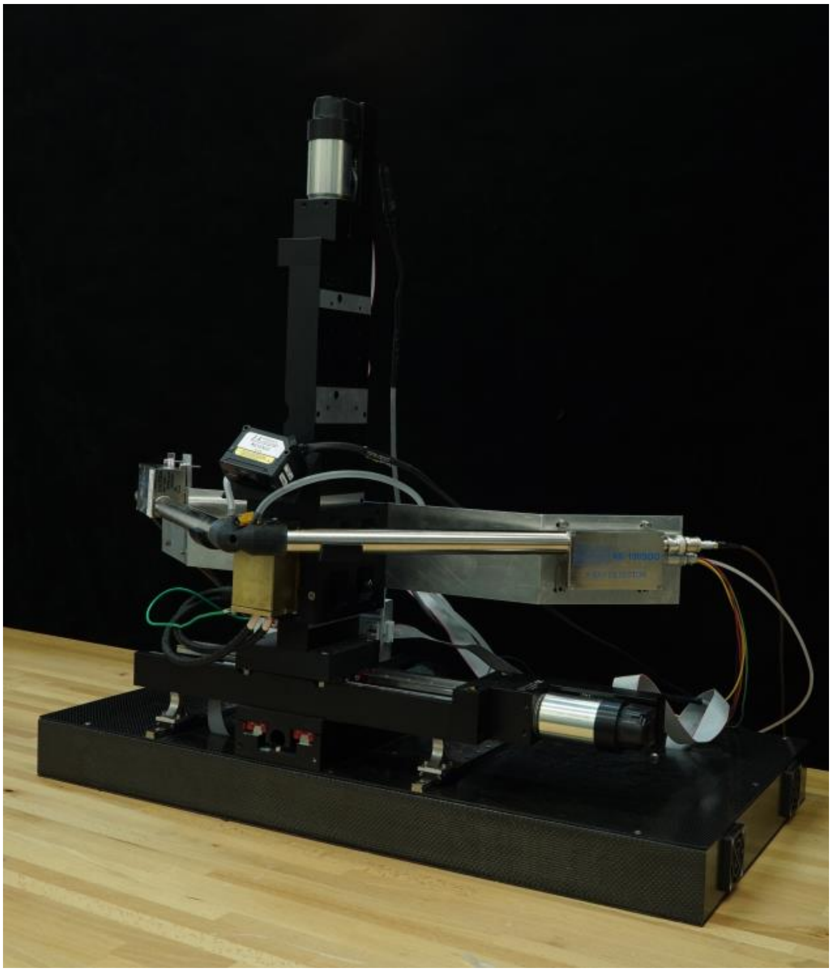

Figure C.1. The *XRF multi-sensor detection system* prototype

The new instrument will have an increased active area, thanks to the adoption of multiple detectors possibly also of wider active area. The first prototype will have a double detector configuration, as shown in figure C.1, but I already started a study for the development of a configuration exploiting 3-4 detectors.

The second main limitation of the XRF2 is its spatial resolution, which is now adequate for many CH applications but can be insufficient in some case. This has been pointed out using the XRF1, as explained in paragraph 2.4. So, some tests to evaluate the SR have been carried out, exploiting home-made and commercial standard samples (Edmund Optics), formed by parallel bars, alternating “full and “empty” bars, which in each group have the same thickness and spacing. The largest bar the scanner cannot discern is assumed to be its resolving power (from now on, spatial resolution). The results have shown that the SR is around 500 µm, when using the 800 µm collimator. Even if it is possible to distinguish objects with dimensions smaller than those of the beam size, typically down to about one half of its diameter, the dimensions of the objects in the elemental maps result different from the real dimensions, as seen for the detail of the peacock tail (Fig.2. 11). To meliorate the SR of the XRF2, a new collimator (Ø 400 µm) was manufactured and the SR was measured. Results show the expected SR increase and now the SR is less than 300 µm. The increase of the SR is clearly visible from the intercomparison of the measurements carried out on the same detail with the two different beam sizes, as shown in Fig. C2.

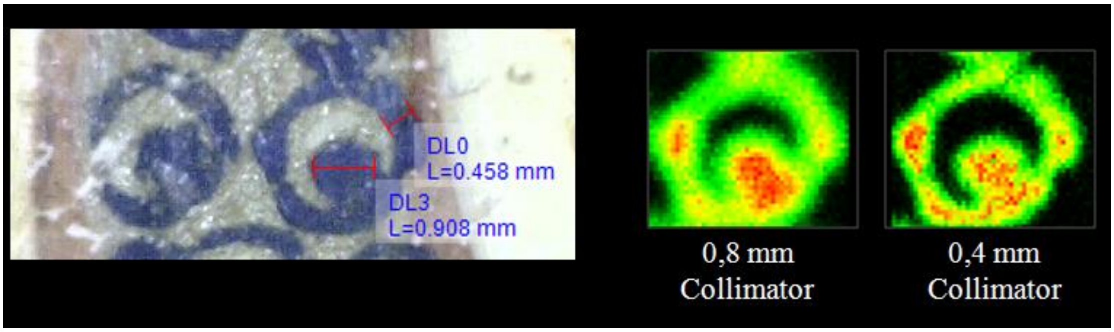

Figure C.2. Cu elemental maps of the same detail obtained with the 800 and 400 µm collimators, using in both cases a 100 µm step and the same experimental conditions. The comparison allows pointing out the unfaithful representation obtained with the worse SR

It can be noticed that the 800 µm collimator Cu-map does not provide a faithful reproduction of the detail under study, what instead holds true for the 400 µm collimator.

Unfortunately, as said above, high resolution maps have heavy costs in terms of working time; for example, in the above example, the SR improvement has been obtained by increasing the measurement time roughly of a factor 4, to compensate the beam intensity decrease.

Thus, to further improve the SR of the scanner, a polycapillary lens will be installed. It consists of many hollow glass channels (each working as a waveguide) focusing the beam into a small spot, maintaining high intensities (a polycapillary lens can normally have a transmission factor thousand times greater than a collimator providing the same nominal beam width, in the 1-10 keV energy range).

My collaboration with the CNA (Centro Nacional des Acelaradores, Seville, Spain) allowed me to gain a good operative knowledge on the use of XRF spectrometers equipped with polycapillary lenses. Actually, in the framework of this collaboration, I have exploited their µ-XRF spectrometer for the measurements of Etruscan gold jewels, in order to identify the soldering technique. Since the analyzed jewels are characterized by details of typical dimensions down to few tens of microns, a high SR is required. The µ-XRF spectrometer allowed studying the joining areas of the jewels and obtaining reliable information about the soldering technique used by Etruscan goldsmith.

Considering the experience gained with the μ-XRF exploiting a polycapillary lens, a third generation XRF scanner is under development, combining the use of this optics with a multi-sensor system, thus simultaneously improving both SR and detection efficiency.

REFERENCES

[1] A. Gilardoni, C. Gilardoni, AP. Gilardoni, *Defectologia o Controlli Non Distruttivi CND*, ed. Gilardoni S.p.A., 1971

[2] R. Van Grieken, A. Markowicz. *Handbook of X-Ray Spectrometry*, CRC Press Inc., 2nd Edition, Boca Raton FL (USA), November 2001.

[3] G. F Knoll., *Radiation detection and measurement*, John Wiley&Sons Inc., New Jersey (USA), 4th Edition, 2010.

[4] C. Ruberto, *Application of portable XRF on cultural heritage: Studies on Beato Angelico's fresco, the "Madonna delle Ombre", in San Marco*, Master's thesis, University of Florence, Academic year 2012-2013.

[5] Bruker, XRF Data Differences: Quantitative, Semi-Quantitative, and Qualitative Data

[6] R. Jenkins, R.W. Gould, D. Gedke, *Quantitative X-ray Spectrometry*, ed. Marcel Dekker Inc., 1995.

[7] A. Markovitz, Pramana- J.Phys., 76, 2 (2011), 321-329.

[8] D.K.G. De Boer, X-*Ray Spectrometry*, 19, 3 (1990), 145.

[9] K. Nygård, K. Hamalainen, S. Manninen, P. Jalas, J.P. Ruottinen, *Quantitative thickness determination using x-ray fluorescence: application to multiple layers*, X Ray Spectrometry, 33 (2004), 354-359.

[10] A. Re, D. Angelici, A. Lo Giudice, E. Maupas, L. Giuntini, S. Calusi, N. Gelli, M. Massi, A. Borghi, L.M. Gallo, G. Pratesi, P.A. Mandò, *New markers to identify the provenance of lapis lazuli: Trace elements in pyrite by means of micro-PIXE*, Appl. Phys. A, 111, 1 (2013) 69-74.

[11] P.A. Mandò, M.E. Fedi, N. Grassi, *The present role of small particle accelerators for the study of Cultural Heritage*, European Physical Journal Plus, 126, 4 (2011) 1-9.

[12] N. Grassi, P. Bonanni, C. Mazzotta, A. Migliori, P.A. Mandò, *PIXE analysis of a painting by Giorgio Vasari*, X-Ray Spectrom., 38, 4 (2009) 301-307.

[13] M.E. Fedi, L. Liccioli, L. Castelli, C. Czelusniak, L. Giuntini, P.A. Mandò, L. Palla, F. Taccetti, *Memory effects using an elemental analyser to combust radiocarbon samples: Failure and recovery*, Nuclear Instruments and Methods in Physics Research Section B: Beam Interactions with Materials and Atoms, 361 (2015) 376-380.

[14] L. Caforio, M.E. Fedi, P.A. Mandó, F. Minarelli, E. Peccenini, V. Pellicori, F. Petrucci, P. Schwartzbaum, F. Taccetti, *Discovering forgeries of modern art by the 14C Bomb Peak*, European Physical Journal Plus, 129 ,1 (2014) 1-5.

[15] M.E. Fedi, L. Carraresi, N. Grassi, A. Migliori, F. Taccetti, F. Terrasi, P.A. Mandò, *The artemidorus papyrus: Solving an ancient puzzle with radiocarbon and ion beam analysis measurements*, Radiocarbon, 52, 2 (2010) 356-363.

[16] A. Migliori, P. Bonanni, L. Carraresi, N. Grassi, P.A. Mandò, *A novel portable XRF spectrometer with range of detection extended to low-Z elements*, X-Ray Spectrom., 40 (2011) 107-112.

[17] L. Castelli, L. Giuntini, F. Taccetti, E. Barzagli, F. Civita, C. Czelusniak, M.E. Fedi, N. Gelli, F. Grazzi, A. Mazzinghi, L. Palla, F.P. Romano, P.A. Mandò, *New criterion for in situ, quick discrimination between traditionally maintained and artificially restored Japanese swords (katanas) by XRF spectroscopy*, X-Ray Spectrom., 42 (2013) 537-540.

[18] A. Mazzinghi, *XRF analyses for the study of painting technique and degradation on frescoes by Beato Angelico: First results*, N. Cim. C, Volume 37-4 (2014) 253-262.

[19] A. Mazzinghi, L. Giuntini, N. Gelli, C. Ruberto, *XRF study on the gilding technique of the fresco "Crocifissione con Santi" by Beato Angelico in the San Marco monastery in Florence*, X-Ray Spectrom., ,. 45, 1 (2016) 28–33.

[20] N. Grassi, L. Giuntini, P.A. Mandò, M. Massi, Advantages of scanning-mode ion beam analysis for the study of Cultural Heritage, Nuclear Instruments and Methods in Physics Research Section B: Beam Interactions with Materials and Atoms 256, 2 (2007), 712-718.

[21] 40kV Cable with MAGNUM X-ray Sources, Technical Datasheet. Moxtek, Orem UT (USA), D. Rev., 2014

[22] L. Giuntini, L. Castelli, L. Carraresi, C. Czelusniak, M. E. Fedi, N. Gelli, L. Liccioli, P. A. Mandò, M. Massi, A. Mazzinghi, L. Palla, C. Ruberto, M. Giannoni, G. Calzolai, M. Chiari, F. Lucarelli, S. Nava, F. Taccetti. *Portable XRF scanner for material composition analysis*. Report_3RCM_G42004, Improvement of portable instrumens and analytical techniques for in-situ applications, Final report of coordinated research project G42004, International Atomic Energy Agency, Vienna (A), 2015

[23] Amptek XR-100SDD detector, User's Manual. Amptek, Bedford MA (USA), 2014

[24] AXIS 241Q/241S Video Server, User's Manual. Axis Communications AB, Lund (S), 2009.

[25] PI M-414, Technical Datasheet. Physik Instrumente (PI) GmbH&Co. KG, Karlsruhe (D), 2014.

[26] http://doc.qt.io/qt-5/licensing.html

[27] B. Achilladelis, A. Robertson, P. Jervis, *A Report on Project SAPPHO: A Study of Success and Failure in Industrial Innovation*, Two Volumes, Centre for the Study of Industrial Innovation, London (1971).

[28] R. Rothwell, *Innovation and Re-innovation: A Role for the User*, Journal of Marketing Management, 2, 2 (1986), 109-123.

[29] S. Conway, *The Role of Users in the Innovation Process*, Doctoral Working Paper Series, 10 (1993) (NS), Aston Business School.

[30] E. von Hippel, *The dominant role of users in the scientific instrument innovation process*, Research Policy, 5 (1976), 212-239.

[31] Keyence handbook, Tough, Reliable, Repeatable Laser Measurement Simplified.

[32] https://www.arduino.cc/en/Main/ArduinoBoardUno

[33] CAEN handbook, Digitizer DT 5780.

[34] G. Gauglitz, T. Vo-Dinh, *Handbook of spectroscopy*, Wiley-CCH Verlag-GMBH & Co. HGaA (2005).

[35] L. Giuntini, M. Massi, S. Calusi, N. Gelli, L. Castelli, L. Carraresi, C. Czelusniak, M.E. Fedi, A.M. Gueli, L. Liccioli, P.A. Mandò, A. Mazzinghi, L. Palla, C. Ruberto, F. Taccetti, *The set-up for forward scattered particle detection at the external microbeam facility of the INFN-LABEC laboratory in Florence*, Nuclear Instruments and Methods in Physics Research Section B: Beam Interactions with Materials and Atoms, 348 (2015), 8-13.

[36] I.C. Freestone, *The provenance of ancient glass through compositional analysis*, Mater. Res. Soc. Symp. Proc. 852 (2005), O8.1.1–OO8.1.14

[37] C. Chiavari, M. Martini, E. Sibilia, M. Vandini, *Thermoluminescence (TL) characterisation and dating feasibility of ancient glass mosaic*, Quaternary Science Reviews 20 (2001) 967-972.

[38] E.V. Sayre, R.W. Smith, *Compositional categories of ancient glass*, Science, 133 (1961), 1824–1826.

[39] I. van der Werf, A. Mangone, L.C. Giannossa, A. Traini, R. Laviano, A. Coralini, L. Sabbatini, *Archaeometric investigation of Roman tesserae from Herculaneum (Italy)by the combined use of complementary micro-destructive analytical techniques*, Journal of Archaeological Science 36 (2009) 2625–2634.

[40] V. Gedzevičiūtė, N. Welter, U. Schüssler, C. Weiss, *Chemical composition and colouring agents of Roman mosaic and millefiori glass, studied by electron microprobe analysis and Raman microspectroscopy*, Archaeol Anthropol Sci., 1 (2009), 15–29.

[41] J. Henderson, *Chemical characterization of Roman glass vessels, enamels and tesserae*, In: P.B. Vandiver, J. Druzik, G. Segan Wheeler (Eds.), Materials Issues in Art and Archaeology II. Materials Research Society, Symposium Proceedings, Pittsburgh 185 (1991), 601–607.

[42] J. Henderson, *The raw materials of early glass production*, Oxf. J. Archaeol., 4(1985), 267–291.

[43] V.A. Sole, Talk *The PyMca X-ray Fluorescence Toolkit, Advancing Quantitative Chemical Imaging*, J@mp’11 Meeting: Joint Users’ Meeting at PSI 2011, Paul Scherrer Institut, Villigen (CH), September 2011.

[44] http://www.esrf.fr/computing/bliss/downloads

[45] G. Artioli, *Scientific Methods and Cultural Heritage: An Introduction to the Application of Materials Science to Archaeometry and Conservation Science*, Oxford University Press (2010), New York (USA).

[46] R. van Grieken, K. Janssens, *Cultural Heritage Conservation and Environmental Impact Assessment by Non-Destructive Testing and Micro-Analysis*, Taylor & Frencis group plc (2005), London (UK).

[47] K. Janssens, R. Van Grieken, *Comprehensive analytical chemistry: Non-destructive Micro Analysis of Cultural Heritage Materials*, Elsevier (2004), vol.XLII.

[48] K. Možina, K. Možina, S. Bračko, *Non invasive methods for characterization of printed cultural heritage*, J. of Cult. Her., 14 (2013), 8–15.

[49] A. Amat, C. Miliani, B.G. Brunetti, *Non invasive multi technique investigation of artworks: anew tool for on the spot data documentation and analysis*, J. of Cult. Her., 14 (2013) 23–30.

[50] R.L. Feller, R. Ashok, B. Berrie, Artist's pigments: a handbook of their history and characteristics, Cambridge University Press and National Gallery of Art (1993), vol.1- 3.

[51] C. Genestar, *Characterization of grounds used in canvas and sculpture*, Materials Letters 54, 5–6 (2002), 382-388.

[52] F. Rosi, A. Daveri, B. Doherty, S. Nazzareni, B.G. Brunetti, A. Sgamellotti, C. Miliani, *On the Use of Overtone and Combination Bands for the Analysis of the CaSO4–H2O System by Mid-Infrared Reflection Spectroscopy*, Appl. Spectrosc. 64 (2010), 956-963.

[53] J. Gettens Rutherford, H. Kühn, W.T. Chase, *Lead White*, Studies in conservation 12, 4 (1967), 125-139.

[54] M.I. Cooper, P.S. Fowles, C.C. Tang, *Analysis of the laser-induced discoloration of lead white pigment*, Applied Surface Science, 201, 1–4 (2002), 75-84.

[55] P.A. Mandò, M.E. Fedi, N. Grassi, A. Migliori, *Differential PIXE for investigating the layer structure of paintings*, Nuclear Instruments and Methods in Physics Research Section B, 239, 1–2 (2005), 71-76.

[56] L. Bonizzoni, A. Galli, G. Poldi, M. Milazzo, *In situ non-invasive EDXRF analysis to reconstruct stratigraphy and thickness of Renaissance pictorial multilayers*, X-Ray Spectrometry 36, 2 (2007), 55-61.

[57] R.J.H. Clark, L. Cridland, B.M. Kariuki, K.D.M. Harris, R. Withnall, *Synthesis, structural characterisation and Raman spectroscopy of the inorganic pigments lead tin yellow types I and II and lead antimonate yellow: their identification on Medieval paintings and manuscripts*, J. Chem. Soc. Dalton Trans 16, 1995, pp. 2577–2582.

[58] D. Hradil, T. Grygar, J. Hradilová, P. Bezdička, V. Grűnwaldová, I. Fogaš, C. Miliani, *Microanalytical identification of Pb-Sb-Sn yellow pigment in historical European paintings and its differentiation from lead tin and Naples yellows*, Journal of Cultural Heritage 8, 4 (2007), 377–386.

[69] H. Kühn, *Verdigris and copper resinate*, Studies in Conservation 15, 1 (1970), 12-36.

[60] T.D. Chaplin, R.J.H. Clark, D.A. Scott, *Study by Raman microscopy of nine variants of the green–blue pigment verdigris*, Journal of Raman Spectroscopy 37, 1-3 (2006), 223-229.

[61] K. Castro, A. Sarmiento, I. Martínez-Arkarazo, J.M. Madariaga, L.A. Fernández, *Green Copper Pigments Biodegradation in Cultural Heritage: From Malachite to Moolooite, Thermodynamic Modeling, X-ray Fluorescence, and Raman Evidence*, Analytical Chemistry 80, 11 (2008), 4103-4110.

[62] CenniniCennino, The craftsman's handbook (Il libro dell'arte), Yale University Press, 1936 (1437).

[63] J. Kirby, M. Spring, C. Higgitt, *The Technology of Red Lake Pigment Manufacture: Study of the Dyestuff Substrate*, National Gallery Technical Bulletin, 26 (2005), 71-87.

[64] A. Claro, J. Melo, S. Schäfer, J.S. Seixas de Melo, F. Pina, K.J. van den Berg, A. Burnstock, *The use of microspectrofluorimetry for the characterization of lake pigments*, Talanta, 74, 4 (2008), 922 – 929.

[65] D. Hradil, T. Grygar, J. Hradilová J, P. Bezdička, *Clay and iron oxide pigments in the history of painting,* Appl Clay Sci., 22, 5 (2003) 223-236.

[66] U. Casellato, P.A. Vigato, U. Russo, M. Matteini, *A Mössbauer approach to the physico-chemical characterization of iron-containing pigments for historical wall paintings*, J Cult. Heritage, 1 (2000), 217-232.

[67] R.J. Gettens, G.L. Stout, In: Painting materials, a short encyclopaedia Dover Publications, Inc. (1966), New York (USA), p 134.

[68] R.M. Cornell, U. Schwertmann, *The iron oxides: structure, properties, reactions, occurrences and uses,* VCH, New York (1996).

[69] B. Hochleitner , V. Desnica , M. Mantler , M. Schreiner, *Historical pigments: a collection analyzed with X-ray diffraction analysis and X-ray fluorescence analysis in order to create a database*, Spectrochimica Acta Part B, 58 (2003), 641–649.

[70] M. Matteini, A. Moles, *Tecniche della pittura antica: le preparazionidel supporto*, in Kermes, Arte e Tecnica del Restauro, 4, Nardini Editore, Firenze (1989).

[71] H. Kessler, *Seeing medieval art*, Broadview press, Ontario (USA), 2004.

[72] C. Higgitt, R. White, *Analyses of Paint Media: new studies of Italian paintings of the Fifteenth and sixteenth centuries*, National Gallery technical bulletin, Yale university press, 26 (2005), 87-97.

[73] M. Del Monte, C. Sabbioni, G. Zappia, *The origin of calcium oxalates on historical buildings, monuments and natural outcrops*, The Science of the Total Environment, 67 (1987), 17-39.

[74] F. Cariati, L. Rampazzi, L. Toniolo, A. Pozzi, *Calcium oxalate films on stone surfaces: experimental assessment of the chemical formation*, Studies in Conservation, 45 (2000), 180-188.

[75] C. Gratziu, A. Melucco Vaccaro, *Patine ad ossalato di calcio: un problema dimetodologia scientifica* in Proceedings of the1st International Symposium 'The Oxalate Films. Origin and Significance in the Conservation of Works of Art', Centro 'Gino Bozza', Milan (1989) 183-193.

[76] B. Stuart, *Analytical Techniques in Materials Conservation*, John Wiley & Sons, Chichester, England (2007).

[77] L. Campanella, A. Casoli, M.P. Colombini, R. Marini Bettolo, M. Matteini, L.M. Migneco, A. Montenero, L. Nodari, C. Piccioli, M. Plossi Zappalà, G. Portalone, U. Russo, M.P. Sammartino, *Chimica per l'arte*, 1st edn., Zanichelli, Bologna (2007)

[78] D. Bigleow, *Gilded wood: conservation and history*, Archetype publications, London (2000).

[79] P. Merrifield, *Original Treatises dating from the XIIth to XVIIIth centuries onthe Arts of Paintings*, Dover, London (1849), 458-461.

[80] R.L. Feller, R. Ashok, B. Berrie, Artist's pigments: a handbook of their history and characteristics, Cambridge University Press and National Gallery of Art (1993), vol. 2, 4.

ACKNOWLEDGEMENTS

Firstly I wish to thank my tutors, Lorenzo Giuntini and Pier Andrea Mandò, for accepting to supervise me,encouraging me during these three years and giving me access to the LABEC laboratory and research facilities;

I am deeply grateful to the *Opificio delle Pietre Dure* for the opportunity of working on many precious artworks, in particular to Marco Ciatti, Cecilia Frosinini and Roberto Bellucci. I also warmly thank for the support all the restorers, especiallyFabrizio Bandini,Francesca CianiPasserini, Luisa Gusmeroli, Alessandra Ramat,PatriziaRiitano, and Oriana Sartiani. Also all the members of the scientific laboratory, in particular Giancarlo Lanterna, Alfredo Aldrovandi and OttavioCiappi, are acknowledged with gratitude. I would like to acknowledge, with gratitude, Giuseppe Zeccarellifor having provided me with many beautiful images, which have significantlyimproved the quality of my work;

very special thanks to Francesco Taccetti, who has given me the possibility to collaborate with several scientific group thanks to the CHNet - INFN network. In particular I want to thank the New York University in Abu Dhabi, especially Francesco Arneodo, Allen Magnusson, Valerio Conicella and Adriano Di Giovanni for the collaboration in the development of some parts of the XRF2 scanner, developed during my thesis. In addition, I want to thank Alessandro Lo Giudice and Alessandro Re, of INFN- sezione di Torino, and Debora Angelici, of TecnArts.r.l., for the collaboration and fruitful discussions on the many CH applications;

special words of thanks are due to the Cultural Heritage INO-CNR group, in particular to Raffaella Fontana, EzioBuzzegoli, Marco Barucci, Marco Pamapaloni, Marco Raffaelli and Jana Striovafor the very fruitful and pleasant scientific collaboration;

I am also indebted to LuigiaMelillo, Archaeological Museum of Naples, for the opportunity of analyse a Roman Mosaic;

I must here remind the Collaboration with the CNA (Centro Nacional des Acelaradores, Sevilla, Spain) and in particular I wish to thank mycolleague and friendSimonaScrivano for involving me in her scientific project (Catacterización No-desctructiva de JoyasArqueológicas de Oro mediante Micro Fluorescencia de rayos X) and sharing with me her knowledge. For this work, special thanks are also due to Carlotta GiuseppinaCianferoni, director of the Egyptian Collection of the Archaeological Museum of Florence, without whom the interesting and pioneering study on Etruscan gold jewels would not have been possible;

I want to thank the whole LABEC group, specially Giulia Calzolai,Luca Carraresi, Lisa Castelli, Massimo Chiari,MariaelenaFedi, Martina Giannoni,NiclaGelli, MirkoMassi, Franco Lucarelli, Silvia Nava for helping me whenever I needed, giving me ideas onhow to proceed with the work and sharing their skills with me. Marco Manetti and Bernardo Casinifor designing and constructing all the parts of the XRF scanners really in real timebut also for their friendship;

I want to warmly thank my dear colleagues and friends, Anna Mazzinghi, Lara Palla, Caroline Czelusniak, Lucia Liccioli and Anna Impallaria, without whom this workcould not have been done;they were always willing to listen to me, support me and make me laugh;

finally, I want to thank my parents and all my friends, because without them I could have never pursued my passion for this work. Thank you for always believing in me and teaching me that love for what you do is fundamental.